論文 / 著書情報
Article / Book Information

題目(和文)	
Title(English)	Present and future urban climate simulations in a tropical megacity
著者(和文)	DARMANTO NISRINA SETYO
Author(English)	Nisrina Setyo Darmanto
出典(和文)	学位:博士(工学), 学位授与機関:東京工業大学, 報告番号:甲第11171号, 授与年月日:2019年3月26日, 学位の種別:課程博士, 審査員:神田 学,木内 豪,髙木 泰士,中村 恭志,中村 隆志,VARQUEZ ALVIN CHRIST
Citation(English)	Degree:Doctor (Engineering), Conferring organization: Tokyo Institute of Technology, Report number:甲第11171号, Conferred date:2019/3/26, Degree Type:Course doctor, Examiner:,,,,,
学位種別(和文)	博士論文
Type(English)	Doctoral Thesis

Present and future urban climate simulations in a tropical megacity

熱帯メガシティーにおける現在及び将来の都市気候シミュレーション

東京工業大学
Tokyo Institute of Technology

A DISSERTATION PRESENTED
BY
NISRINA SETYO DARMANTO
TO
THE DEPARTMENT OF TRANSDISCIPLINARY SCIENCE AND ENGINEERING
GLOBAL ENGINEERING FOR DEVELOPMENT, ENVIRONMENT, AND SOCIETY

IN PARTIAL FULFILLMENT OF THE REQUIREMENTS
FOR THE DEGREE OF
DOCTOR OF ENGINEERING

TOKYO INSTITUTE OF TECHNOLOGY
TOKYO, JAPAN
MARCH 2019

Advisor
Professor Manabu Kanda（神田　学）

Co-advisor
Dr. Alvin Christopher Galang Varquez

Internal committees
Professor Tsuyoshi Kinouchi（木内　豪）
Dr. Hiroshi Takagi（高木　泰士）
Dr. Takashi Nakamura（中村　恭志）
Dr. Takashi Nakamura（中村　隆志）

A very honour dedication to

my beloved parents Mr. Prihadi Setyo Darmanto and Mrs. Eny Marwanti,
my dearest husband Mr. Muhamad Bintang Hadi Prayoga,
and my supportive sister Mrs. Ariana Darmanto and brother Mr. Dedy Dwi Prasetyo Eryanto.

Acknowledgement

I would like to express my sincere gratitude to my supervisor Prof. Manabu Kanda and my sub-supervisor Dr. Alvin Christopher Galang Varquez for the continuous support of my doctoral research, for their patience, motivation, solution, idea, and immense knowledge. Their guidance and encouragement helped me all the time of this journey, from constructing the theme, method, analysis, and realize them into publications and this thesis.

I would also like to thank my internal thesis committees: Prof. Tsuyoshi Kinouchi, Dr. Hiroshi Takagi, Dr. Takashi Nakamura, and Dr. Takashi Nakamura, for their insightful comments and suggestions during the completion process of this thesis. My greatest appreciation to their questions which broaden my analysis from many directions and perspectives.

This research could not be accomplished without support from the Environment Research and Technology Development Fund of the Ministry of the Environment, Japan, Strategic Research on Global Mitigation and Local Adaptation to Climate Change (S-14) project. I would also like to express my appreciation for S-14 project for giving me opportunity to join their workshop and symposium related to climate change mitigation and adaptation.

My sincere thanks also goes to Dr. Atsushi Inagaki who provided me an opportunity to have hands-on experience on atmospheric observation know-how and widen my knowledge regarding integration of simulation and observation. Also, my best appreciation goes to Mrs. Yuuko Okamoto for her incredible supports and assistance during my time in the laboratory. My deep regard is addressed to Ms. Meral Yucel, Mr. Muhammad Rezza Ferdiansyah, and Ms. Yovita Wangsaputra for the ideas, motivation, supports, and fun. Also my thanks to other fellow labmates: Ms. Natsumi Kawano, Mr. Takafumi Sueishi, Mr. Motoyuki Hijikata, Mr. Shouta Kiyomoto, Mr. Riku Kawamoto, Mr. Kouhei Yamashita, Mr. Yoji Ishibashi, Mr. Xiaoqing He, Ms. Yuuri Narita, and Mr. Tetsuro Tomizawa for their company.

Last but not least, I would like to address my profound gratitude to my husband, family and my circles for their unconditional love, kindness, and huge support. This accomplishment would not have been possible without them.

Abstract

Present and future urban climate simulations in a tropical megacity

The effects of urbanization on the present and future atmospheric environments of cities in tropical areas remain uncertain. We introduce a general method for modeling the urbanization effects on present and future climate that can be applied to any city. We apply the model to Greater Jakarta megacity for current study. We introduce an approach to derive 1-km scale urban parameters from globally available satellite imageries for use in numerical mesoscale weather model. It showed that urban parameters made from global datasets could improve performance of the weather model and can be used as a substitute when no real building data are available. Using the urban parameters, we conduct simulations for 2006-2015 as present and 2046-2055 as future urban climate condition. Global climate change scenarios (RCP2.6 and RCP8.5) were coupled with distributed urbanization scenarios (compact and business-as-usual (BaU), based on projections of future urban parameters and anthropogenic heating) in a mesoscale weather model. Despite the predominant influence of global effects, the urban effects of individual grids were spatially varied. Finally, we project the future heat-related mortality risk based on each future scenario's temperature.

抄録

熱帯メガシティーにおける現在及び将来の都市気候シミュレーション

本論文は「Present and future urban climate simulations in a tropical megacity（熱帯メガシティーにおける現在及び将来の都市気候シミュレーション）」と題して英文で書かれ，8章から構成される．

第1章「Introduction」では，急激な社会・経済的発展が予想される熱帯メガシティーにおいて，気候変動および都市化による気温上昇の将来予測と対策の効果を評価する一般的手法の確立の必要性について論じている．そのための技術的課題を指摘し，本論文のねらいと独創性について述べている．

第2章「Theoretical framework」では，都市化による大気環境への影響に関する物理的メカニズムと既存の知見をレヴィユーし，将来予測に必要な技術とそのための都市データについて述べている．

第3章「Urban roughness parameter data construction from global satellite imageries」では，グローバルに入手可能な衛星データを用いて，都市粗度パラメータを推定する手法を提案し，検証を行っている．異なる推定手法を相互比較し，ニューラルネットワークが最善であることを示している．

第4章「Satellite-derived urban roughness parameters performance in WRF mesoscale model」では，第3章で構築した都市粗度パラメータを用いた気象予測計算と，従来手法での気象予測計算を3地点における実測データと比較し，検討している．その結果，建物抵抗が考慮されることによって，風速の再現性およびその結果として主に夜間の気温再現性が顕著に向上することを示している．

第5章「Present urban climate reconstruction」では，第4章で検証した都市粗度パラメータを考慮した象予測計算手法を用いて，8 月の気象再現計算をそれぞれ 10 年

間分行った上でアンサンブル平均し, 標準的な日気象変化（気候値）を再現している. さらに, 3地点の観測実測データと比較して, その性能評価を行っている.その結果, 第4章と同様の風速・気温再現性の向上を確認している.

第6章「Future urban climate projection」では,グローバルな社会経済シナリオ (温暖化ガス排出:RCP および経済発展:SSP）とローカルな都市発展シナリオ (BAU, コンパクトシティー) を組み合わせて, 将来の気候予測を行っている. また, グローバルな気候変動による気温上昇と都市化による気温上昇の影響もそれぞれ評価している. 都市化影響は, 都市全体の平均気温上昇へ寄与は大きくないが, 都市化の進展する（人口の増加する）街区などでは気候変動を数倍も凌駕する気温上昇をもたらすことを示している. また, 最善シナリオ（RCP2.6, SSP1, コンパクトシティー）は, 最悪シナリオ（RCP8.5, SSP3, BAU）に対して気温上昇を顕著に抑制しており、適応策の有効性を示唆している.

第7章「Future heat-related mortality projection」では,第6章で得られた将来気候予測結果にバイアス補正を施したうえで, 熱関連死亡リスクの将来予測を行っている. その結果, 気温上昇の顕著な地点では気温上昇も大きい傾向にあり, 人間への影響評価においてローカルな都市影響を考慮することの重要性を示している.

第8章「Concluding remarks」では,本論文の成果をとりまとめ,今後の展望について述べている.

以上要するに,本論文では,人工衛星だけから都市粗度パラメータを推定する手法を提案したうえで,いくつかのグローバル・ローカルな社会経済シナリオの基で将来の気候予測を行い, さらには熱関連死亡リスクの予測も行った上で, 従来のグローバルな気候変動研究とローカルな都市気象研究の融合が重要であることを示している. 開発した手法は一般性を有し, 今後, ローカルなデータを入手しにくい他の発展途上国のメガシティーへの応用・展開も期待される. これらの成果は,工学上・工業上高く評価できる.よって,博士（工学）として価値が十分あるものと認められる.

Contents

List of Figures

List of Tables

List of Symbols

Symbol	Name	Unit
A_F	Frontal area of buildings	m^2
A_p	Plan area of buildings	m^2
A_T	Plan area total of surface	m^2
A_x	Surface area of element(s)	m^2
c	Specific heat of a substance	$Jkg^{-1}K^{-1}$
c_p	Specific heat of air at constant pressure	$Jkg^{-1}K^{-1}$
D_{av}	Daily average number of deaths	deaths/day
d	Aerodynamic displacement height	m^2
g	Gravity acceleration	ms^{-2}
H	Height of building(s) adjacent to urban canyon	m
H_{ave}	Average building height in an area	m
H_{max}	Maximum building height in an area	m
I	Thermal inertia	$Jm^{-2}K^{-1}s^{-1/2}$
k	Thermal conductivity	$Wm^{-1}K^{-1}$
L	Obukhov length	m
$LW^{\downarrow}$	downward longwave radiation	Wm^{-2}
$LW^{\uparrow}$	upward longwave radiatio	Wm^{-2}
Q	Heat flux	W
Q_*	Net allwave radiation flux	Wm^{-2}
Q_E	Latent heat flux	Wm^{-2}
Q_F	Anthropogenic heat flux	Wm^{-2}
Q_H	Sensible heat flux	Wm^{-2}
ΔQ_A	Net energy (sensible and latent) advection	Wm^{-2}
ΔQ_S	Net heat storage	Wm^{-2}
r_U	Ratio/fraction of an urban area	(-)
$SW^{\downarrow}$	downward shortwave radiation	Wm^{-2}
$SW^{\uparrow}$	upward shortwave radiation	Wm^{-2}
T_0	absolute surface temperature	K
T_A	air temperature	K
Td_{mean}	Daily mean temperature	°C
Td_{max}	Daily maximum temperature	°C
u	Longitudinal (x-axis) wind component	ms^{-1}
u_*	Friction velocity	ms^{-1}

Symbol	Name	Unit
$\bar{u}_z$	Wind velocity at certain height	ms^{-1}
v	Lateral (y-axis) wind component	ms^{-1}
W	Width of urban canyon	m
w	Vertical (z-axis) wind component	ms^{-1}
w_*	Convective velocity scale	ms^{-1}
z	Vertical distance, height above ground	m
z_0	Aerodynamic roughness length	m
z_e	Height of inflection point at 1D wind profile	m
z_H	Mean height of elements in an area	m
z_i	Depth of mixed layer	m
α	Surface albedo	(-)
ε	Emissivity	(-)
κ	Von karman constant	0.4
λ_c	Complete aspect ratio	(-)
λ_f	Frontal area fraction/index	(-)
λ_p	Plan area fraction/index	(-)
μ	Mean (in statistic)	(-)
ψ_{sky}	Sky view factor	(-)
ρ	Density	kgm^{-3}
σ	Stefan-Boltzmann constant	$5.67 \cdot 10^{-8}\ Wm^{-2}K^{-4}$
σ	Standard deviation (in statistic)	(-)
σ_H	Standard deviation building height in an area	m
τ	Reynolds stress	Pa
τ_0	Momentum flux	Pa
θ	Potential temperature	K
θ_*	Friction temperature	K
ζ	Dynamic stability parameter	(-)

List of Abbreviation

Abbreviation	Definition
ABL	Atmospheric boundary layer
AHE	Anthropogenic heat emission
AU	All urban area
BaU	Business as usual
CDF	Cummulative distribution function
CGK	Cengkareng WMO weather station
GDP	Gross domestic product per capita
GCM	General circulation model
HSU	High sprawl urban
ISL	Inertial sublayer
KMO	Kemayoran WMO weather station
LCZ	Local climate zone
ML	Mixed layer
OT	Optimum temperature
PDF	Probability density function
PGW	Pseudo global warming
RCM	Regional climate model
RCP	Representative concentration pathways
RR	Relative risk (of heat-related mortality)
RSL	Roughness sublayer
SSP	Shared socio-economic pathways
TF	Transfer function
TPR	Tanjung Priok WMO weather station
UCL	Urban canopy layer
UCM	Urban canopy model
UHI	Urban heat island
WMO	World meteorological organization
WRF	Weather research and forecasting
WUDAPT	World urban database and access portal tools

1 Introduction

1.1 Background of study

It is predicted that 68% of world total population in 2050 will live in urban areas (United Nations, 2018) and most of the populations will reside in megacities. The vast portion of megacities with more than 10 million population is currently located in Asia as shown in Figure 1.1. As mentioned before in 2.2, the major environmental impacts of urbanization is inadvertent modification of urban climate due to increase of heat and pollutant emissions, and changes in surface cover of built-up areas. Furthermore, global climate change will affect vast majority of population in the world, including urban population. Previous research in analyzing the relation between global warming as background temperature increase and UHI phenomena stated that a megacity like Tokyo metropolitan area suffers from 1.7°C per century temperature increase (JMA, 2011), surpassing the background

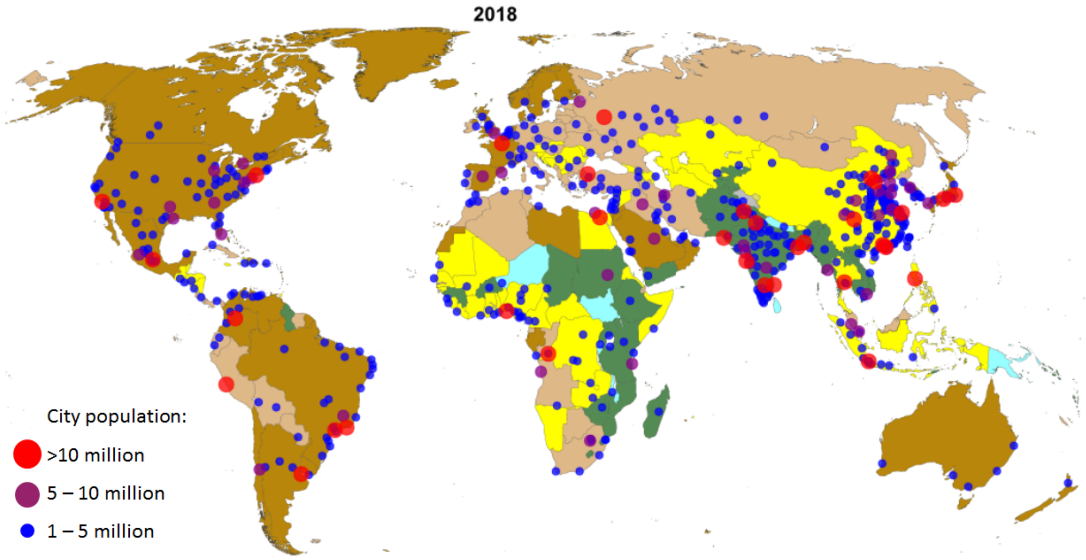

Figure 1.1: Urban population size in 2018 (United Nations, 2018)

global temperature increase of 0.78°C per century. Kusaka et al. (2000) estimated the historical change as well as the spatial distribution of daytime UHI intensity by numerical simulation and showed that the land-use change during the past 85 year in Tokyo megacity generates daytime UHI intensities of 2-3°C on average and 3-4°C on maximum. Based on both global and local urban effects, urban climate analysis for present and future in cities -especially those in Asia where rapid urbanization is happening- is one of the most siginificant discussion to realize climate change mitigation-adaptation efforts in urban area (IPCC, 2014). Subject to further investigation, even though the urban effect to the global climate change effect can be straightforward for ambient temperature, the interaction itself is under non-linear dynamic mechanism (Lee et al., 2017).

Current Asian megacities (e.g., Beijing, Shanghai, Manila, Jakarta, Delhi, Mumbai) are growing in economic and have urban population growth rate of more than 2.5% yearly, thus analyzing urban climate change in these cities are necessary. Most of these cities are located in (sub)tropical latitude and unfortunately,

researches regarding urban effect in these areas are only make up less than 20% of world's total studies (Roth, 2007b). Regardless of high rate of urbanization, there are several factors causing the lack of scientific research and public awareness on urban effect and urban climate changes in (sub)tropical areas following study by Emmanuel (2016) as follows.

1. Background climate

   Convention on global climate studies presumed that there is little influence of local urban effect on global climate change (Parker, 2010; Trusilova et al., 2013). In addition, UHI intensity trend as profound evidence of urban effect in tropical region is comparably smaller than those in temperate and dry climate (Varquez and Kanda, 2018). These statements give strong assumption that the urban area is concerned as minor effect in climate studies. Hence, further tropical urban climate research remains weak and unknown.

2. Technical limitation

   In indoor thermal comfort case, previous study showed that in tropical region's medium air temperature (i.e., 30-35°C), natural ventilation becomes less effective (MacGregor and Nieuwolt, 1998). Active cooling is the main strategy for urban tropics. Properous tropical megacities such as South East Asian (SEA) megacities tend to do active adaptation strategy (i.e., using energy for cooling) which is quite problematic. Study by Yau and Pean (2014) said that in every 1°C increase on outdoor temperature will cause 2% drop in split-type air conditioner coefficient of performance and results in increase of electricity energy to achieve expected indoor thermal comfort. Thus, will generate more sensible heat to the atmosphere.

   Further consent comes for urban data scarcity in developing countries (e.g., urban land cover map, 3D buildings data, future urban planning master plan). Urban climate study is very much sensitive and highly depend on data

availability. Even though these data eventually can be acquired through co-operation with local government or urban planning stakeholders, the process are quite demanding (i.e., in perspective of time, money, labor).

3. Institutional issues

   It always been missing link between scientific communities and local stakeholders in communicating scientific knowledge to real policies implementation that is often directed by city government (Rosenzweig et al., 2015; Ren, 2017). Another issue regarding the commitment of creating urban mitigation-adaptation policies on climate change in Asian megacities are still limited (https://www.c40.org/). Here, government shows large portion in establishing the commitment and policy in creating climate change resilience city. Therefore, supports and funding for building more public knowledge and awareness on urban climate are strongly depend on institutional commitment and policies.

4. Socioeconomic issues

   As mentioned before, urban tropics have warmed to an extent that passive adaptation in tackling thermal comfort is already exhausted. In addition to excess heat emission, the use of active cooling is quite dubious for such developing worlds. High economic gap in the population of these developing cities put aside the lower-income urban dwellers without access to air conditioning facility. Thus, bring this matrix of population into thermal-related risks.

1.2 Objective and importance of the study

More recently, questions have been raised about the background climate dominacy over urban effect, especially in those rapidly growing megacities. Study conducted

in fast-growing subtropical city Hanoi by Lee et al. (2017) and Ho Chi Minh city by Doan and Kusaka (2018) give scientific evidences that UHI in these two cities are approaching a significant increase of 0.5°C in next 30 years. This value is cannot be neglected since it corresponds to 20-30% of global warming effect. Thus, this research is important to ascertain the evidence in a tropical city that prospected to expand hastily in near future.

Regarding the issues stated on technical limitation, this study also aims to develop a realistic urban data useful for urban climate numerical simulation solely from globally available and open source datasets for present and future urban condition. The mitigation strategy in this study is designed to follow Representative Concentration Pathways (RCP) global emission scenarios. So far, studies on combining global climate change with local urbanization scenario are conducted using locally available built-up area master plan Lee et al. (2017); Doan and Kusaka (2018); Yang et al. (2016). However, in this study we attempt to develop local adaptation scenario in form of urban morphological expansion and AHE (i.e., passive adaptation strategy) to support RCP's target is derived from global Shared Socioeconomic Pathways (SSP). We aversely using any data from local governments or stakeholders to optimize global implementation. The framework is designed to provide a generic, repeatable, and realistic approach to futuristic urban climate studies.

Greater Jakarta urban agglomeration, including second largest megacity in the world of Jakarta and its satellite cities, is considered well-suited in represent a rapidly growing megacity in tropical area and is selected as this research case study. Despite still low-number of researches focusing on urban effect in Greater Jakarta, new report of C40 cities (2018) stated that Jakarta's government currently put active concern and has strong mayoral power on buildings and transportation regulations. This open a huge opportunity for this study to be

implemented as one of consideration in creating future Jakarta urban planning assessment. By introducing the prime analysis on future-heat related mortality in 1km high-resolution in Jakarta, this study should make a major contribution on building social concern and public awareness of urban climate study importance in Jakarta. Furthermore, the results of this study are expected to fill the communication-gap on urban climate between scientific communities (e.g., meteorologist, climatologits, enviromental scientists) and design stakeholders (e.g., urban planners, architects, government officials, policy makers).

Recently, many researchers efficiently analyzed the urban climate by using state-of-the-art numerical weather and climate model which capable on medium to fine resolution such as regional climate model (RCM). RCMs are 3D weather models which encompass regional or continental scale –medium resolution- up to city scale –fine resolution-. One of the sophisticated mesoscale model widely used in urban climate research is Weather Research and Forecast (WRF) model. WRF is capable of coupling with various UCMs and will be further explained in 3.1. The coupled model can provide comprehensive urban climate study for present and future condition at city scale up to urban region (Table 2.1) which is suitable for the purpose of this study.

1.3 Scopes of the study

1. Chapter 1 : Introduction

   Chapter 1 includes background of study, objective, and importance of study.

2. Chapter 2 : Literature review

   In chapter 2, the theoretical background regarding urban climate fundamentals for current research is presented.

3. Chapter 3 : Urban roughness parameter data construction from global satel-

lite imageries

Urban morphological data is fundamental requirement for numerical urban climate simulation. This chapter focuses on 1km resolution urban roughness data development in megacities exclusively from global satelite imageries. The concept is to find empirical function between satellite imageries and real urban parameters from cities so that the function can be applicable generically in global extent.

4. Chapter 4 : Satellite-derived urban roughness parameters performance in WRF mesoscale model

   Upon completion of satellite-derived urban roughness parameter conducted in chapter 3, the performance of the parameters in mesoscale model WRF coupled with single-layer UCM is validated and analyzed in this chapter. Validation uses comparison of near-surface temperature and wind speed between simulation and 1-hourly observation data taken from urban meteorological weather station in Jakarta.

5. Chapter 5 : Present urban climate reconstruction

   In chapter 5, the study expanded into projecting future urban climate, where this chapter on reconstruction of current historical climate from 2006-2015 (i.e., 2010s) which will be reference as present climate on the next projection step.

6. Chapter 6 : Future urban climate projection

   This chapter is the main goal of this study. Projection to the future urban climate in 2046-2055 (i.e., 2050s) is conducted in this chapter. Future climate change effect is conducted using pseudo global warming dynamical downscaling method. Local urbanization projection is focused on method in constructing future urban parameters and AHE, based on socio-economic

parameters projection change. The future scenarios are considered as no-mitigation-adaptation strategy and with-mitigation-adaptation strategy.

7. Chapter 7 : Future heat-related mortality projection
   In chapter 7, impact on heat-related mortality due to urban climate change is analyzed. Basic equation of optimum temperatur and heat-related mortality relative-risk is used to project future excess death due to temperature increase in older population group.

8. Chapter 8 : Concluding remarks
   This chapter concluding all previous chapters in this study. Recommendations related to current study and future works also adressed in this chapter.

1.4 Summary

Overall, this chapter comprehends objective, challenges and importance of urban climate study in a tropical megacity. Urban climate modelling analysis through numerical simulation methods for current and future urban climate are briefly explained in this chapter. This chapter also offers concept of connection between scientific and general communities in communicating and building public awareness on urban climate problem.

2

Theoretical framework

2.1 Definition of urban climate

Climate is defined as average weather condition for a particular region and time period, usually in a long time-span around 30-years. It can be in the form of averages of temperature, precipitation, humidity, sunshine, wind velocity, and other meteorological parameters that occur over a long period in a particular place. Based on spatial coverage, climate can be classified as macro/ meso/ regional climate and local climate (i.e., boundary layer climate). Boundary layer climate is defined based on general and specific condition of climate in its atmospheric boundary layer.

Atmospheric boundary layer (ABL) is the boundary layer as that part of the troposphere that is directly influenced by the presence of the earth's surface, and responds to surface forcings with a timescale of about an hour or less (Stull,

2009). These forcings include frictional drag, evaporation and transpiration, heat transfer, pollutant emission, and terrain induced flow modification. Urban boundary layer climate (hereafter, urban climate) is an interaction of physical, chemical, and biological process operating to produce change/ affecting the state of urban atmospheric condition and create a distinct urban weather characteristic for long period. Scale of urban climate study is varied from urban region to city block, with classification of urban morphological units as defined in Table 2.1.

As other layers in ABL, urban layer can be divided into several sublayers following their special characteristic. Most of the interaction between surface and its ABL happened in surface layer. Surface layer occupied 10% of the closest ABL to ground surface. ABL above urban area has special term of urban boundary layer (UBL) due to its structure and it is affected by presence of city/ urban area. This UBL can be defined into 4 layers (Figure 2.1):

1. Urban canopy layer (UCL)

   UCL spans from ground to the mean height of buildings. It consists of exterior (outdoors) and interior (inside buildings) atmosphere and where human thermal comfort study is mostly taken place. The urban structures include facet, element, and urban canyon. Scaling parameter in this layer is z_H and W.

2. Roughness sublayer (RSL)

   RSL spans from ground up to 2-5 times the height of buildings including the UCL. In the RSL flow is affected by individual elements. The urban structures include block and urban climate zone. Scaling parameter in this layer is z, z_H, W.

3. Inertial sublayer (ISL)

   ISL located above the RSL, where shear-dominated turbulence creates a

logarithmic velocity profile and variation of turbulent fluxes with height is small. Urban structures scale in this layer are in regards to combined blocks or city scale. Scaling parameter in this layer is $(z - d)$, z_0, u_*, θ_*. The atmospheric phenomena happening in this layer is shaping the majority of urban climate.

4. Mixed layer (ML)

   Located above the ISL, where atmospheric properties are uniformly mixed by thermal turbulence and usually capped by and inversion (up to upper limit of entrainment zone). Scaling parameter in this layer is z_i, w_*, θ_*^{ML}. This layer is interacting with other mesoscale climate dynamic.

Urban units	Built features	Green and water features	Urban climate phenomena	Typical horizontal length scales	Climate scales
Facet	Roof, Wall, road	Leaf, lawn, pond	Shadows, storage heat flux, dew, and frost patterns	10 x 10 m	Micro
Element	Residential building, high-rise, warehouse	Tree	Wake, stack plume	10 x 10 m	Micro
Canyon	Street, canyon	Line of street trees or gardens, river, canal	Cross-street shading, canyon vortex, pedestrian bioclimate	30 x 200 m	Micro
Block	City block with canyons, factory	Park, wood, storage pond	Climate of park, factory cumulus	0.5 x 0.5 m	Local
Neighborhood or Local Climate Zone	City center, residential (quarter), industrial zone	Greenbelt, forest, lake, swamp	Local neighborhood climates, local breeze, air pollution district	2 x 2 km	Local
City	Built-up area	Complete urban forest	Urban heat island, smog dome, patterns of urban effects on humidity, wind	25 x 25 km	Meso
Urban region	City plus surrounding country side	All green and water surface area in city and surrounding country side	Urban 'plume', cloud, and precipitation anomalies	100 x 100 km	Meso

Table 2.1: Classification of urban morphological units

An urban system is composed of mixed intertwined climatically-active surfaces. Urban built-up area is consists of many different urban fabrics (e.g., concrete, bricks, sand, etc) which have their own climatic properties including:

- Radiative: geometry, absorptivity, reflectivity, transmissivity, emissivity
- Thermal: specific heat, heat capacity, thermal conductivity, thermal admittance
- Moisture: interception and storage capacity, permeability, stomatal characteristic, chemical nature
- Aerodynamic: roughness, zero-plane displacement, porosity

To an extent of coarser scale (i.e., city scale), there are some important parameters to express urban physical properties:

1. Plan area fraction (λ_p)

   To define plan view are occupied by element type A_x within a total ground surface area. The element type can be defined as building, impervious surface, vegetation, or water area. The plan area fraction in this study is mainly focusing on building plan area fraction (λ_p) or hereafter, called as plan area index.

2. Frontal area fraction or frontal aspect ratio (λ_f)

   The frontal area fraction is a necessary parameter regarding urban airflow and aerodynamic. It indicates the fractional wall area of the buildings towards the oncoming flow. It is the ratio of the sum of wall windward area of buildings to the total plan (A_T) area they occupy.

3. Complete aspect ratio (λ_c)

   Complete aspect ratio is defined as total 3D external surface area of all

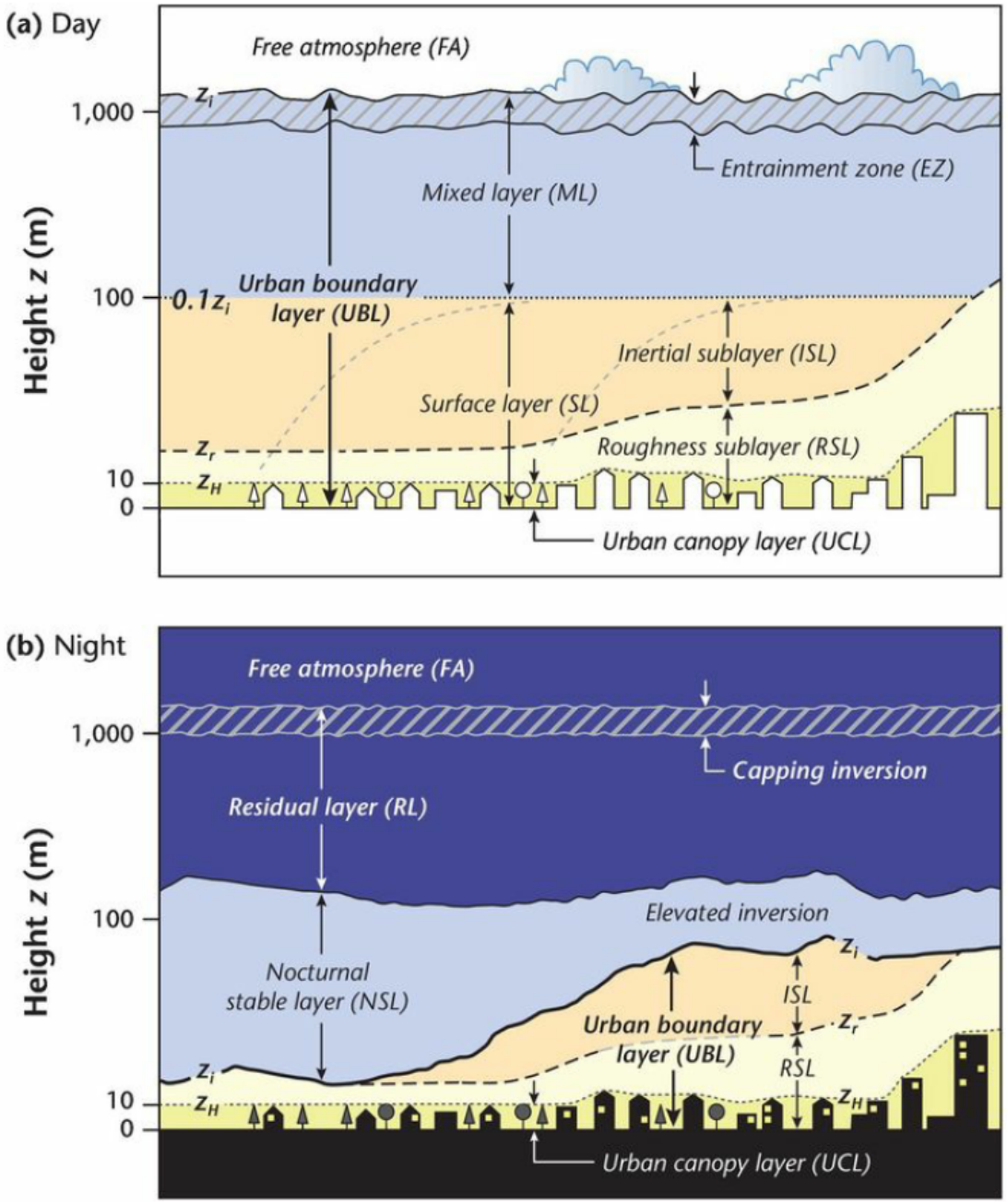

Figure 2.1: Schematic of typical atmospheric layers above urban surface by (a) day and (b) night. Taken from Oke et al. (2017)

.

elements including the ground surrounding them, to the total plan area they occupy (A_T).

4. Sky view factor (ψ_{sky})

   Sky view factor is the fraction of the radiative flux leaving the surface at a single point that reaches the atmosphere above the urban canopy. It value depends on the position and orientation of surface relative to the amount of sky obstruction overhead.

5. Canyon aspect ratio (H/W)

   Building canyons are described by two dimensional cross section, referred to dimensionless ratio of H/W where H is the height of the building walls adjacent to the street and W is the width, usually the street's width. The canyon aspect ratio is important to define radiation access, shade and trapping, urban canopy layer wind effects, thermal effects at pedestrian level, and the dispersion of vehicle pollutants.

6. Average building height (H_{ave})

   The H_{ave} is the average buildings height in a unit of plan area they occupy without mentioning the ground elevation.

7. Displacement height (d)

   Zero plane displacement height or also called zero wind displacement height. In a packed roughness elements (i.e.,, densely built-up area or dense forest), the top of these elements begins to act like a displaced surface instead of ground surface. Thus, in urban area, average building height acts as the displaced surface on the wind flow. The height above surface up to the displaced surface is called displacement height. This displacement height also can be defined as the central height of drag action (Kanda et al., 2013).

8. Length of roughness element (z_0)

   The shifted height level due to surface roughness at which the logarithmic wind profile has zero wind speed is defined as z_0.

9. Anthropogenic heat flux density or anthropogenic heat emission (AHE)

   The anthropogenic heat flux is mainly the result of consumed energy due to accumulated urban activities that converted to heat and released to the atmosphere. The (AHE) is expressed as sensible heat flux (W/m^{-2}).

10. Thermal admittance of urban area

    Thermal admittance is surface thermal property that governs the ease with which a body takes up or releases heat. It is the square root of the product of thermal conductivity and heat capacity ($I = \sqrt{k \cdot \rho \cdot c}$). Also called thermal inertia.

Stewart and Oke (2012) defines land use classification in more systematic description following the effect of local ground surface to the microclimate called local climate zones. The classification is including urban climate zones which defines a general concept of urban surface area characteristic based on built-up area morphology. This study is based on several observation-based studies in each urban climate zone compiled altogether. The study results in a generic range of urban morphology and heat parameters value that can be practically applied in any urban studies.

2.2 Urban effect on atmospheric environment

The most discussed urban effect is urban heat island (UHI) phenomena, a condition where urban area temperature is higher than surrounding rural area (Figure 2.2). UHI is one of the example of inadvertent climate modification (Oke, 1978) as we cannot return the urban condition back to before its urbanized. There

are several mechanisms that cause UHI as mentioned in the study of Varquez and Kanda (2018). The first mechanism is due to increase of sensible heat flux in urban area from anthropogenic activities, reduction in evapotranspiration, and turbulent-induced heat transport. Second one is due to increase of thermal inertia in urban area. Complexity of urban surfaces related to built-up area configurations and added with buildings materials caused urban area as a heat-trap. Thus, urban area will have higher resistance to temperature change or in other words, contributes to higher thermal inertia. Due to its high thermal inertia, temperature in urban area during nighttime is higher than its surrounding and emits higher longwave radiation. This is why more of UHI are observed during the nighttime or nocturnal UHI. The complexity of urban also allows the third reason of UHI. As the urban area is strongly varied in buildings shape and morphology, urban area creates a rougher surface compare to its surrounding. Urban area as surface roughness elements then act as aerodynamic drag and prevent cooler airflow from outskirts entering the city. Other atmospheric environment change due to urban effect is related to urban-induced localized precipitation (Bornstein, 1968; Niyogi et al., 2017), urban breeze circulation (Hidalgo et al., 2010; Eliasson and Holmer, 1990), sea-breeze penetration over urban area (Yoshikado, 1990; Simpson et al., 1977), and air pollution (Vardoulakis et al., 2003; Guttikunda et al., 2014, 2003).

2.2.1 Airflow in urban area

As the wind flow through a surface, the roughness of the surface act as obstacle and form friction between the surface and the atmosphere, thus change the wind velocity profile as illustrated in Figure 2.3. The wind velocity in certain height $\bar{u}_z$ is defined as exponential function of height as vertical distance from the surface reference as written in wind log-law equation 2.1 considering displacement height d and roughness length of momentum z_0. This equation is generically applicable

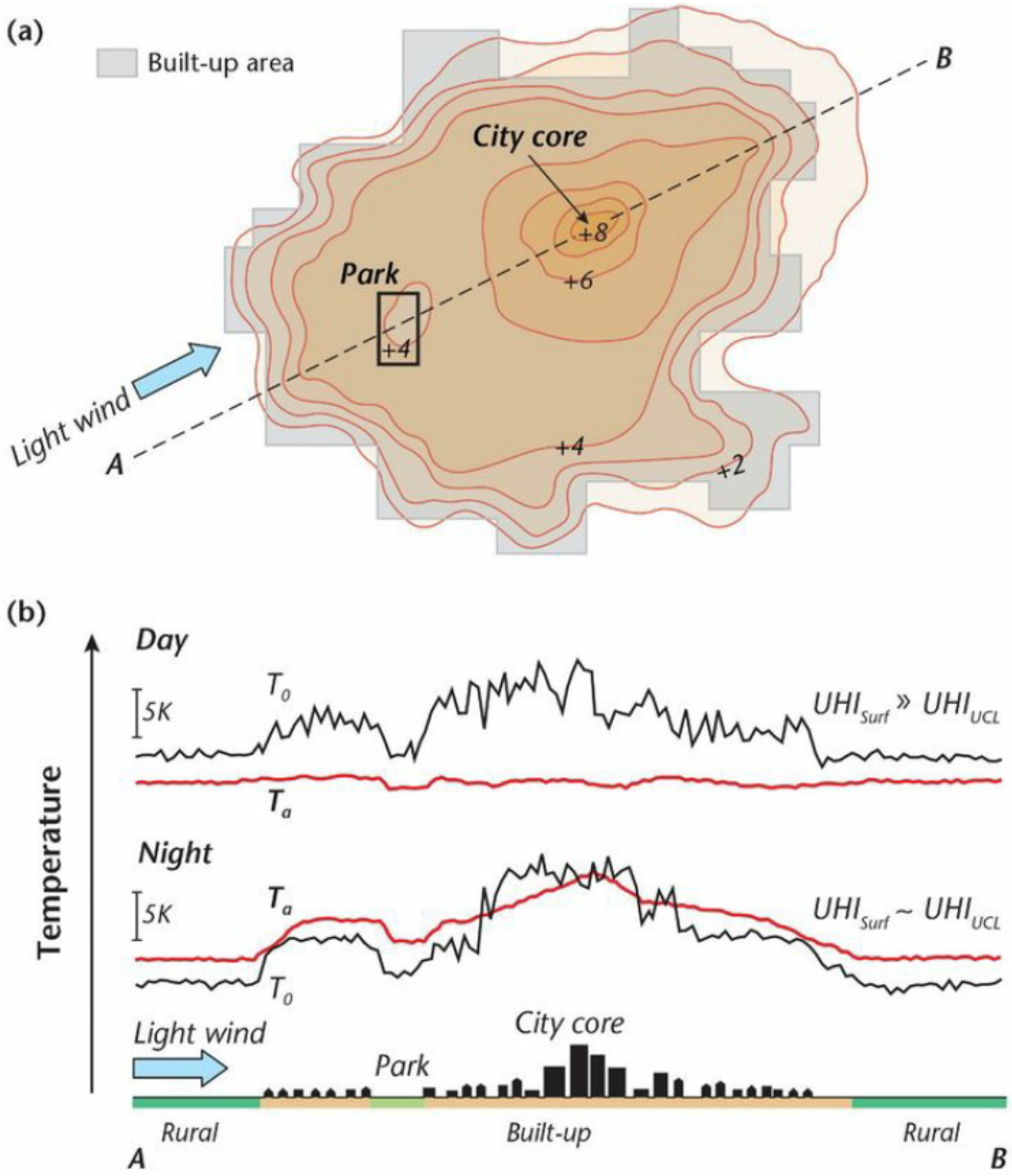

Figure 2.2: Schematic figure of UHI during nighttime calm and clear conditions in relativelity plain topography urban area. (a) Isotherm map illustrating typical features of UHI and its correspondence to urban elements. (b) 2D cross section A-B of both surface and near surface air temperature. Taken from Oke et al. (2017)

.

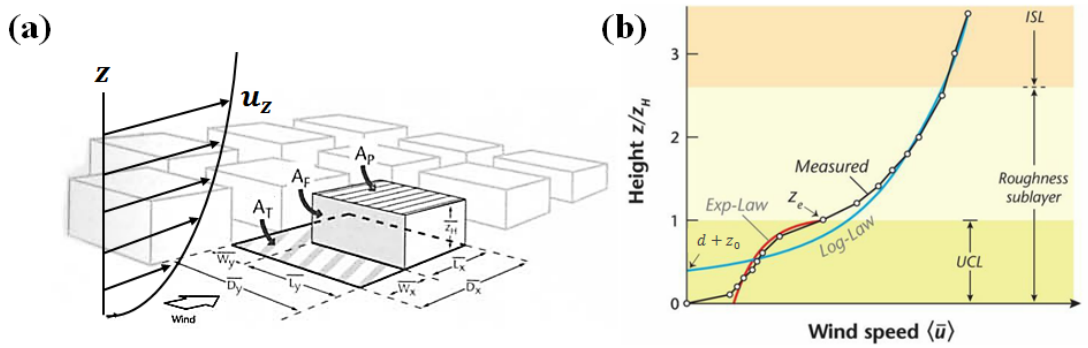

Figure 2.3: Schematic of windflow through buildinglike array. (a) Log-law profile before passing through buildinglike array and definition of surface dimensions used in urban morphology parameters, $\lambda_p = A_p/A_T$, $\lambda_f = A_F/A_T$. (b) Change of 1D wind profile after passing buildinglike array where z_e defines inflection point and log-law profile is interpolated to $d + z_0$ point. Modified from Grimmond and Oke (1999); Oke et al. (2017)

.

in ISL.

$$\frac{\bar{u}_z}{u_*} = \frac{1}{\kappa} \ln\left(\frac{z - d}{z_0}\right) \tag{2.1}$$

where u_* is friction velocity and κ is von karman constant (0.4).

Urban area aerodynamical properties in term of displament height d and roughness length of momentum z_0 varied much depending of the urban morphological characteristic. One study by Stewart and Oke (2012) defined local climate zones (LCZs) which classified land use depends each local climatic condition, including urban climate zones which is defined in 10 classes of LCZs. The mentioned study is based on several individual studies compiled altogether to find average range of important urban morphological parameters. Urban parameters for each LCZ is defined in corresponding study. From the study, it is known that a city is contained with many variations of urban LCZs with each LZC has distinct roughness value characteristic. The roughest value happened in LCZ 1 and 2 (i.e., high rise and dense buildings) which usually happened in the city center where the business areas are located.

Urban as roughness element and heat source affecting the atmospheric above by inducing turbulence and turbulent exchanges that determines the whole urban boundary layer nature. The most widely accepted framework of turbulent exchanges relationships in the ISL is the Monin-Obukhov Similarity Theory (MOST). Studies by Moriwaki and Kanda (2006); Roth (2007a) proofed that MOST can be applied in the urban ISL. MOST provides a mean of relating turbulent fluxes to the mean gradient of associated property, and furthermore making predictions about turbulence intensities and other characteristic of the turbulent flow. Turbulent flow in ISL can be expressed in MOST by following parameters: (1) momentum flux of the urban interface on the overlying flow τ_0; (2) sensible heat flux density Q_H; (3) effective height above ground $(z - d)$; and (4) buoyancy ratio g/θ. Length scales related to mentioned parameters are described as follows.

$$u_* = \sqrt{\tau_0/\rho} \tag{2.2}$$

$$\theta_* = -\frac{Q_H}{\rho c_p u_*} \tag{2.3}$$

$$L = \frac{\theta u_*^2}{\kappa g \theta_*} \tag{2.4}$$

$$\zeta = \frac{z - d}{L} \tag{2.5}$$

where θ_* is friction temperature (K), c_p is specific heat of air at constant temperature ($Jkg^{-1}K$), L is Obukhov length (m), g is gravitational acceleration (ms^{-2}), and ζ is measure of dynamic stability in the ISL (unitless) (i.e., $\zeta = 0$ for neutral, $\zeta > 0$ for stable, $\zeta < 0$ for unstable).

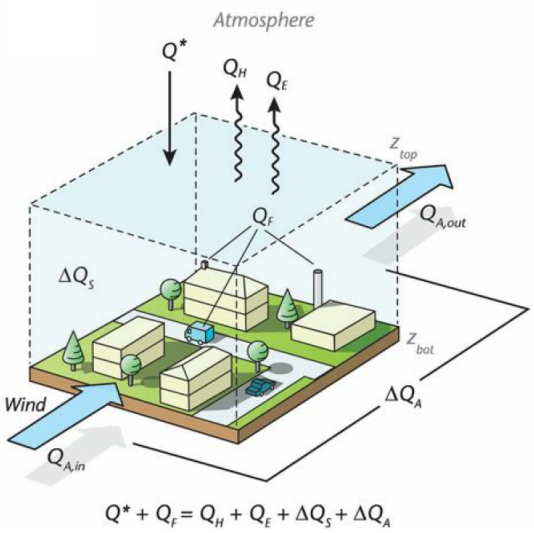

Figure 2.4: Conceptual diagram of urban energy balance. Taken from Oke et al. (2017)

2.2.2 Urban energy balance

Urban energy balance is a fundamental element to analyze and predict urban climate since the heat exchange and temperature variance strongly depend on it. The main component of urban energy balance is shortwave radiation budget, longwave radiation budget, sensible heat flux, latent heat flux, advective heat flux, and anthropogenic heat flux. Equation 2.6 shows the basic energy balance equation which also applicable in urban area as illustrated in Figure 2.4.

$$Q_* + Q_F = Q_H + Q_E + \Delta Q_S + \Delta Q_A \tag{2.6}$$

where Q_* refers to total radiation energy flux, Q_F refers to anthropogenic heat emission flux, Q_H refers to sensible heat flux, Q_E refers to latent heat flux, ΔQ_S refers to the net heat storage by all built-up elements, and ΔQ_A refers to the net energy due to advective heat energy transport (i.e., ΔQ_A can be neglected by assuming extensive and homogenous urban surface).

Radiation from the sun is the most important driver of climates near the

ground. In urban area, the complexity of morphology gives a distinctive feature of solar beam blocked by buildings and cast shadows in buildings canyon. Urban radiation balance is fundamental aspect to determine the urban energy balance. The basic principles of surface radiation budget on a surface is explained in equation 2.7.

$$\begin{aligned} Q_* &= SW_* + LW_* = SW^{\downarrow} - SW^{\uparrow} + LW^{\downarrow} - LW^{\uparrow} \\ Q_* &= (1-\alpha)SW^{\downarrow} + \varepsilon LW^{\downarrow} - \varepsilon\sigma T_0^4 \end{aligned} \tag{2.7}$$

where

$SW^{\downarrow}$ = downward shortwave radiation
$SW^{\uparrow}$ = upward shortwave radiation
$LW^{\downarrow}$ = downward longwave radiation
$LW^{\uparrow}$ = upward longwave radiation
α = surface albedo
ε = surface emissivity
σ = Stefan-Boltzmann constant ($5.67 \cdot 10^{-8}$ $Wm^{-2}K^{-4}$)
T_0 = absolute temperature of a surface

The distinct radiation properties in urban area are albedo and emissivity that can be separated based on urban scale as follows.

a. Urban canopy

   The radiation attributed in urban canopy is closely related to urban fabric albedo and emissivity. In addition, urban structure, including roof facets and inter-element spaces incorporate the effects of shadowing and multiple exchanges between facets. Sky view factor is necessary parameter to determine radiation properties of urban structures under canopy layer.

b. Urban canyon

Multiple reflections phenomena of radiation between two adjacent building walls is concerned as important part of urban radiation balance (Harman et al., 2004). This affects the albedo of the urban canopy layer due to radiation trapping which also increase the urban thermal inertia.

c. Larger urban system (e.g., city blocks scale)

Combined urban structures define an urban system. A block of dense high rise building will have different radiation properties value with less dense high rise complex.

d. Urban boundary layer (i.e., mesoscale)

Radiation in the scale of urban boundary layer is closely related with the atmospheric condition due to local urban effect and influenced by larger synoptic system. As urban area emits larger concentration of aerosol, it reduces the albedo and changing the shortwave. Furthermore, greenhouse gases will affect the longwave radiation.

In a highly complex urban area, the urban energy budget to be solved is challenging. In numerical model for large urban area, predicting urban energy balance can be realized through implementation of energy balance model under urban canopy model scheme (Grimmond et al., 2011). The main equations in the urban energy balance model includes estimation of radiation heat budget, and sensible and latent heat flux. Based on defined urban layers, urban energy balance models can be separated into single layer model (Masson, 2000; Kusaka et al., 2001; Grimmond and Oke, 2002; Oleson et al., 2008b,a) and multi-layer model (Martilli et al., 2002; Kondo et al., 2005; Hamdi and Masson, 2008). Most of the models are using bottom-up approach on estimating canopy level urban energy balance. However, in simple urban energy balance for mesoscale simulations (SUMM) developed by Kanda et al. (2005b,a), the urban energy balance is predicted based on top-down

approach to calculate bulk parameter components of radiation budget and turbulent heat fluxes. This top-down approach is very much suitable for mesoscale urban climate analysis due to its practical and computational efficiency.

The terms Q_F is defined as the additional sensible heat influx from urban area or also defined as anthropogenic heat emission (AHE) flux. AHE is mainly the result of chemical energy or electrical energy that are converted to heat and released to the atmosphere as a result of urban activities. The energy released during combustion or energy released due to consumption of electricity for daily activities such as building space cooling or heating, lighting, water heating, cooking, electrical appliances, and bigger scale consumption such as industrial or manufacturing. These energy consumptions converted into heat energy which is usually injected into atmosphere as sensible heat. Energy consumption is greatly varies depending on the climate of the region, economy condition, and socio-culture differences. The AHE is expressed as sensible heat flux (Wm^{-2}) and is included in the top of urban canopy layer in urban numerical modelling.

2.3 Urban climate study

In analyzing weather and atmospheric condition in urban area, one must combine three basic combination analysis approach: theoretical, observation, and numerical/physical modeling. An urban climate study is determined by theoretical scientific foundation in order to earn clear objective on:

- properties and processes of interest parameters (e.g., air temperature, turbulent fluxes),
- physical extent or domain on the system which is studied about, and
- strategy for capturing the horizontal, vertical and temporal variation within the system.

Theoretical concept become important to understand what supposed to be happened on an active surface on a state of atmospheric condition and vice versa while plannig and conducting observation and modeling. Among many theoretical background fundamentals to urban climate analysis, this study will focus more on urban area as surface roughness element and heat emission source.

The urban effect phenomena itself is primarily analyzed and known from intensive observation experiments, from near-ground to towering instruments measurement systems, also from moving observation mounted on mobile devices. The important and fundamental decisions are the positioning of the instrument platform horizontally and vertically within the urban landscapes for point(s) observation. A well-positioned observation point could record representative attributed data of the underlying urban surface. Instruments mounted on observation tower overlying an extent of urban area and having sufficient vertical scale up to ISL (Figure 2.5) could give a solid reference on realistic turbulent transfer and energy balance (Moriwaki and Kanda, 2006). However, analysis of urban effect through observation itself is limited by the ability of technology to record the effect and the impossibility of observing the effects of all combinations of urban elements which are strongly varied temporally and in 3D spatial extent. Remote sensing measurements from higher atmospheric layers from around canopy layer height up to space could give more observational data with larger extent vertically and horizontally. However, data quality acquired from remote sensing broadly inadequate in resolution and representativeness of complex urban surface. In addition, a high spatio-temporal remote sensing technology often requires excessive amount of cost which considered as one hefty limitation. Practical restrictions on accesing parts of urban area and urban atmosphere also contributes to the limitation of observation methods.

Another way to analyze urban effect and urban climate phenomena is

Figure 2.5: Urban observation tower for urban climate analysis located in Tokyo suburban area in Kugahara. Picture taken from http://www.ide.titech.ac.jp/~kandalab/

through modelling, physically and numerically. A physical model is a simplified and/or scaled real-world system. The urban elements (e.g., buildings, tree, street canyons) are scaled under controlled environment (e.g., laboratory, wind tunnel, solar radiation chamber) or real atmospheric environment (Figure 2.6). Numerical modelling approaches are aimed at simulating real-world urban phenomena using set of equations that link urban parameters and properties to physical processes (e.g., urban energy balance, urban aerodynamical flow). Similar to physical model, numerical models can be operated under controlled atmospheric environment or realistic atmospheric spatio-temporal boundaries derived from observed meteorological datasets. Through numerical models, ones could analyze state of the atmosphere in macro/meso scale and its interaction with urban canopy layers through coupling with urban canopy models (UCMs). Using the coupled models, the urban atmosphere and surface evolve together in response to dynamic ex-

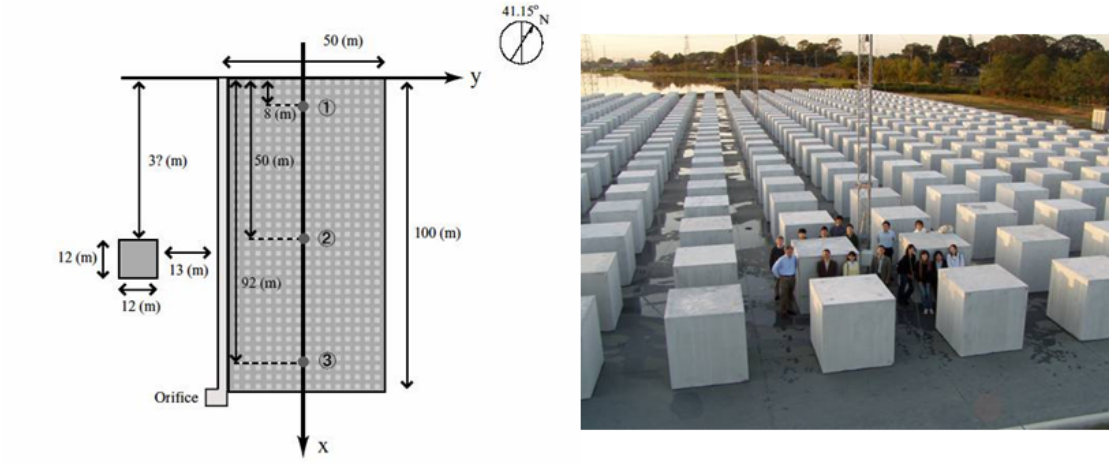

Figure 2.6: COSMO 1/5 scaled urban models. Picture taken from http://www.ide.titech.ac.jp/~kandalab/

change to/from the surface-atmosphere domain. This study is focusing on using the numerical model of mesoscale urban model coupled with urban canopy model in conducting the urban effect in city scale. The coupled system is configured so that a larger scale model (i.e., mesoscale model) provides the upper boundary conditions necessary for smaller scale model (i.e., urban canopy model), which in turn provides the lower boundary conditions for the larger model (Oke et al., 2017). The coupling systems result capable to represent the climate and weather elements necessary for urban climate investigation (Figure 2.7).

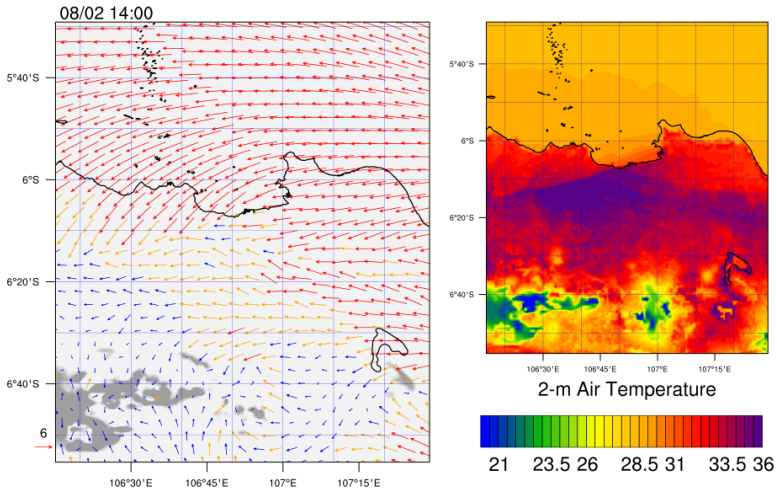

Figure 2.7: Example of numerical modelling result of coupled mesoscale and urban canopy model for horizontal wind field (left) and near-surface temperature (right)

3

Urban roughness parameter data construction from global satellite imageries

3.1 Introduction

Currently, half of the world's population resides in urban areas, and this figure is predicted to increase to 68% (around 6.4 billion people) of the world's total population in 2050, moreover this happening in cities in Asian developing countries in (sub)tropical latitudes (United Nations, 2018). Despite offering improved living standards and signifying rapid economic growth, urbanization also introduces social, economic, and environmental threats. This fact places these cities as the most vulnerable ones on the impact of atmospheric phenomena due to

urban modifications. One of the major environmental impacts of urbanization is modification of the urban climate due to the increase in heat and pollutant emissions, and changes in surface cover. The most widely discussed phenomenon associated with the urban climate is the urban heat island (UHI) (Arnfield, 2003; Bornstein, 1968; Kardinal Jusuf et al., 2007; Miao et al., 2009; Oke, 1973; Roth, 2007b; Taha, 1997), a condition wherein an urban area is significantly warmer than its surrounding rural area. However, most of these studies are carried out on cities in developed countries and none of them conducted in developing tropical cities.

Many recent studies have efficiently analyzed urban climate using state-of-the-art weather and climate models (e.g., mesoscale models), which are capable of medium to fine resolution. Mesoscale models are 3D weather models that encompass regional- or continental-scale medium resolution up to city-scale fine resolution. One of the sophisticated mesoscale models widely used in urban climate research is the Weather Research and Forecast (WRF) model (Chen et al., 2011). The WRF model can be coupled with various urban canopy models (UCMs), either as single (TEB by Masson (2000), 2000; SLUCM by Kusaka et al. (2001)) or multilayer (BEP by Martilli et al. (2002); NJUC-UM-M by Kondo et al. (2005); BEP-BEM by Salamanca et al. (2010)). Further inter-comparison performance analysis among these UCMs is addressed by Grimmond et al. (2011).

Even though some studies recommend on using multilayer UCM for more accurate modelling, this practice requires high computational demand and various input variables on building which extremely challenging to be applied in developing countries. Previous comparative evaluation of several urban land surface models in tropical city reveals that in aggregated neighborhood scale, simple set of parameters has sufficient performance on representing urban heat flux (Demuzere et al., 2017). This indicates that single layer UCM which comparably

more simple than multilayer ones, has great potential to be applied in these developing cities, and furthermore, globally. However, coupling the single layer UCM with the WRF model tends to overestimate near-surface wind speeds (Miao et al., 2009) and insufficiently reproduce surface drag (Nelson et al., 2016). This may be due to inadequate roughness parametrization and a lack of realistic urban parameter distribution. A recent aerodynamic roughness parametrization was developed (Kanda et al., 2013), and spatially distributes these bulk parameters in SLUCM/WRF was shown to improve near-surface wind speeds in Tokyo (Varquez et al., 2015). The necessary distributed urban morphological parameters are: plane area index, λ_p, defined as ratio of total building plane area occupied by buildings to the total floor area; frontal area index, λ_f, defined as ratio of total building frontal area occupied by buildings to the total floor area; average building height, H_{ave}; maximum building height, H_{max}; and the standard deviation of building heights, σ_H. These parameters are necessary for estimating the bulk parameters of zero-plane displacement height, d, and surface roughness length, z_0, of building canopies which determine aerodynamic properties in urban boundary layer.

New land use classification Local Climate Zones (LCZs) (Stewart and Oke, 2012) introduced highly detailed 10 urban cover classes along with each class' ranged value of morphological, thermal, radiative, and metabolic properties. This leads to improvement on recent urban climate researches (Bechtel and Daneke, 2012; Ching, 2013; Stewart et al., 2014). Moreover, recent initiative of World Urban Database and Access Portal Tools (WUDAPT) (http://www.wudapt.org) project develops a framework on collecting and gathering spatial distribution of LCZs (Mills et al., 2015; See et al., 2015). The datasets collected in WUDAPT are at various levels, designated by numbers 0 to 2. A tool for classifying LCZs in level 0 was developed (Bechtel et al., 2015) and gives better representation on

LCZs in many cities across the globe (Bechtel et al., 2016; Danylo et al., 2016; Kaloustian and Bechtel, 2016; Zhongli and Hanqiu, 2016; Cai et al., 2016). Each LCZ is assigned a generic range of urban parameters at the lowest level (level 0). In Level 1, the spatial characteristics of LCZs are refined further based on random sampling for a desired study area. The final level (level 2) provides a highly accurate distribution of LCZs, along with realistic urban parameters. Currently, only datasets at level 0 have methodologies that can be applied globally. Levels 1 and 2 are still limited to specific cities, and their use requires substantial guidance from local experts. Recent approaches on coupling of LCZs from WUDAPT project with urban model improve representation of heat fluxes and temperature distribution (Alexander et al., 2015, 2016; Wouters et al., 2016). Coupling of WUDAPT LCZs in BEP-BEM/WRF gives better representation on intra-urban local climate variability and how wind field is modified due to different urban zones Brousse et al. (2016). The latter study defined urban parameters values by following designated range provided in Stewart and Oke (2012) LCZ's parameters added with local expert knowledge. Thus, each urban zone has one specific value for each urban parameter required in an UCM.

Present study is focusing on how spatial change of urban morphology affect surface drag and wind speed for SLUCM/WRF. This is achieved by modifying urban roughness according to actual distributed 1km bulk urban morphological parameters. Therefore, this study targets a precise estimation of urban morphological parameters from globally available datasets. Furthermore, these parameters can support urban climate modeler to select more precise value during application of LCZs in the model. Distributed urban parameters are required for conducting modified SLUCM/WRF following Varquez et al. (2015). Even though urban cover in latter work is represented in one urban land use type, the urban morphological parameters are distributed differently for each grid. Change on urban thermal

properties and heat budget is not considered at this stage. Thus, effect of urban roughness modification on surface drag and wind speed can be analyzed definitively. Urban morphological parameters are currently estimated from actual 3D building data. However, this database is limited to a few developed cities and remains great challenge to apply the model in megacities in Asian developing countries that has high complexity of urban morphology. Moreover, we aim to provide a way to get detailed urban morphological parameters in any (mega)city by minimizing local expert knowledge, hence it can be applied globally. To achieve these goals, we investigated the potential of using the several latest available global satellite images as inputs and later, derived urban morphological parameters from them.

Landsat 8 satellite mission have been providing latest two-dimensional imagery of earth surface in 30-m horizontal resolution since it was launched (Roy et al., 2014) and also used in LCZs classification (Bechtel et al., 2015). For this study, using Landsat 8 images as urban cover detection data source, we developed a method to determine urban cover fraction parameter λ_p. Later, λ_f is obtained following LES-derived empirical equation on $\lambda_p - \lambda_f$ relationship (Kanda et al., 2013). Because Landsat 8 does not provide vertical information, other global satellite dataset is needed to estimate the building height parameters (H_{ave}, H_{max}, and σ_H) which are core parameters in urban aerodynamic parametrization. Images from two satellites capable of elevation measurements, the 30-m-resolution Advanced Spaceborne Thermal Emission and Reflection Radiometer (ASTER) Global Digital Elevation Model (GDEM) version 2 and the 7.5-arc-second-resolution Global Multi-resolution Terrain Elevation Data 2010 (GMTED2010), were investigated for their potential to estimate H_{ave}. ASTER GDEM has a +7.4-m elevation offset bias in forest areas due to its sensitive measurement of treetops; hence, it is expected that a positive elevation offset in urban areas also exists for the top of

buildings (Tachikawa et al., 2011). On the other hand, GMTED2010 has a coarser resolution than ASTER GDEM has, but it provides new, systematically derived global topographic data for regional applications, and their errors are well within the requirements of the product (Carabajal et al., 2011). It showed that by subtracting ASTER GDEM positive offset by GMTED2010 minimum product, we can estimate the distribution of H_{ave} in Tokyo. From H_{ave} data, H_{max} and σ_H can later be estimated (Kanda et al., 2013).

Another satellite imaging system that is widely used for detecting urban areas is the radiance calibrated 1km nighttime light (NL) images from the Defense Meteorological Satellite Program Operational Linescan System (DMSP-OLS) prepared by Hsu et al. (2015). An analysis of the Anthropogenic Heat Flux (AHF) distribution in China's large cities showed that the DMSP-OLS nightlight image brightness was significantly correlated with higher population density compared to its surrounding (Chen et al., 2012). Higher NL radiance reflects where energy-intensive commercial urban area located as shown in recent study by Dong et al. (2017). In most Asian megacities, this energy-intensive densely populated urban area is characterized by high-rise buildings. Thus, we assume that NL images have high possibility as another predictor in detection of H_{ave}, along with ASTER GDEM and GMTED mentioned before.

By combining all these satellite images, we aim to develop a method of estimating the actual spatial distribution of important urban parameters required for applying new urban aerodynamic parameterization for WRF/SLUCM in developing Asian megacities, where 3D building database is lacking. This study also attempts to highlight tropical urban area where there is still few study regarded. For performance evaluation and validation, we conduct this study on Jakarta, Indonesia, which is considerably fit for our purpose.

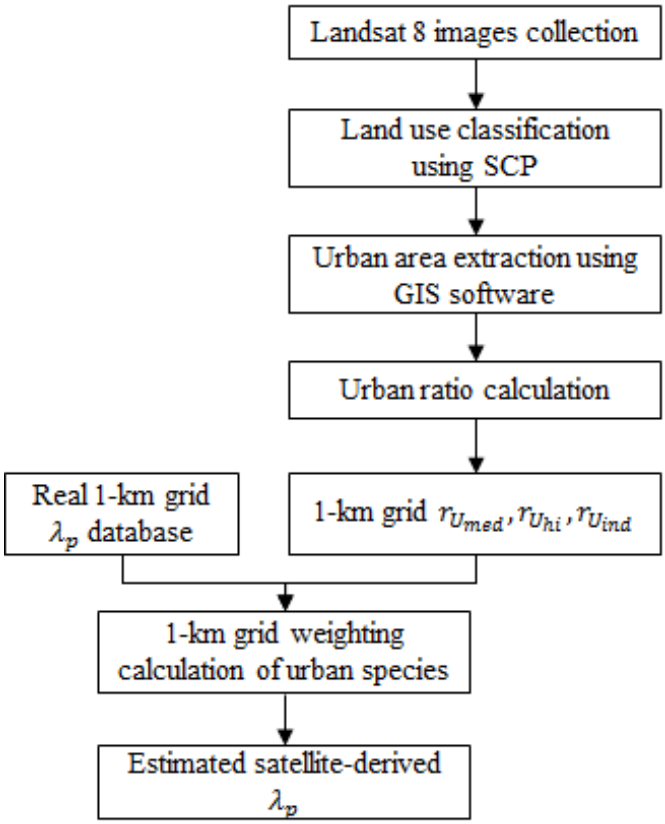

Figure 3.1: Workflow of estimating λ_p from Landsat 8 satellite imageries

3.2 Estimation of λ_p

The process to estimate λ_p occurs in two steps. First, a land-use classification is conducted for the target area at the same spatial resolution as Landsat 8. Later, the parameters are estimated using a derived empirical relationship between the parameters and the fraction occupied by specific urban land use types in a 1km grid. The process is discussed below in detail and the workflow is illustrated in Figure3.1.

3.2.1 Land use classification

For land use classification, we used supervised classification which are commonly incorporated in any GIS processing software. In this study, we use a built-in semi-automatic classification (SCP) plugin available for QGIS Software developed by Luca Congedo (2016). We used SCP version 4.3.0 for this study. First, satellite image enhancement was conducted by converting satellite digital number (DN) reflectance to top of the atmosphere (TOA) reflectance for atmospheric correction, and then performing dark object subtraction (DOS). Image enhancement was used to correct image quality due to atmospheric source noises for each band. After these initial processes, a spectral angle mapping (SAM) algorithm was applied to training datasets to estimate the land-cover classification. SAM has been selected because it is known to perform well in land-use detection (Yuhas et al., 1992; Fan and Deng, 2014). In conducting the SCP, we maintained the 30-m resolution of Landsat 8 used to estimate λ_p.

The supervised classification requires training datasets specified as region of interests (ROIs), user-defined polygons that cover a specific land-use class. SCP is equipped with a region-growing algorithm during the collection of ROIs, which automatically detects similar pixel values on neighboring grids, speeding up the acquisition of training samples. Selected ROIs are stored as a spectral-specific polygon shapefile, which is used as a reference for estimating spectral signatures. In creating an area-specified ROI for study area, a user needs to define the representative land class by overlaying it with high-resolution visible imagery. This was achieved by using satellite imagery of Google Map or Open Street Map as base maps. The ROIs collected for each different land-use classification are then averaged to create spectral signatures. These spectral signatures provide a basis for the land use classification itself. Because this method uses area-specific ROIs, the spectral signatures are valid only for a specific area of study.

In this study, the collected ROIs was based on 10 classes of land use, which had considerably different spectral wavelengths: one water body class (including sea, lakes, and ponds), three vegetation classes (mixed vegetation, grassland, and mixed forest), two bare-soil classes (common bare soil and quarries), one agriculture class (including rice fields and plantation areas), and three urban classes: medium density urban; high density urban; and commercial/industrial. Our aim is to classify urban cover fraction in 1km grid, these urban classes are classified by building density. Urban classes are: medium density corresponding with LCZ 5, 6, 7, 9 (see Stewart and Oke (2012) for the description of the numbers); high density corresponding with with LCZ 2,3; and commercial and industrial corresponding with the LCZ 1, 4, 8, 10. Landsat 8 images are used to defined λ_p or total building floor area in regard to total area of the grid, hence classifying urban area based on their density is considerably sufficient. Furthermore, considering that our target is to create empirical equation based on ordinary least squares (OLS) by solving unknown parameters in linear relationship, the less unknowns will be preferable. Three independent variables from urban classes value is appropriate for this approach. In SAM algorithm for land use classification, each ROI in the same land use class should have similar spectral range value on each band and distinct so they are not overlapping each other. This can be analyzed on spectral plot. Using selected ROIs as training, we run SAM algorithm to classify our designated land use classes and the result for three megacities is shown in Figure 3.2. In classifying urban classes, urban representation refers to Figure 3.3 were used. The classification produced 30-m resolution land use 2D dataset. Ground point validation of the urban area showed that the land use classification proposed in this work gave an accuracy of 88%, 81%, and 86% for Tokyo, Jakarta, and Istanbul respectively.

The method we used in this work was compared with the LCZ classifica-

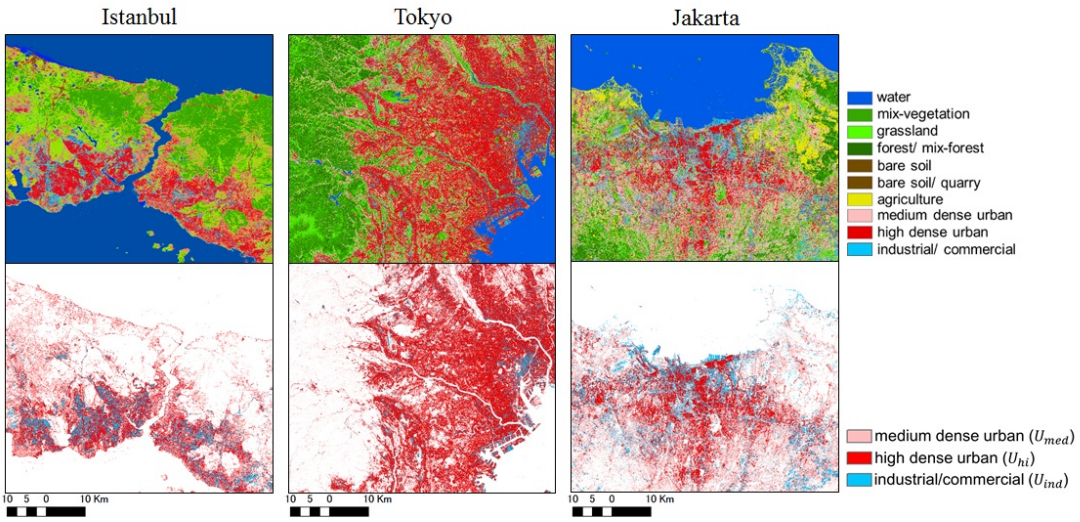

Figure 3.2: Land use classification results in 30-m resolution

tion method of WUDAPT (Figure 3.3), which uses Landsat 8 and produced land use classification based on random forest algorithm (level 0). Even though WUDAPT level 0 can classify 10 different urban covers based on LCZ, the land cover categories we utilized differ in quantity with that of WUDAPT because of our aim. The aim of WUDAPT level 0 is to estimate the distribution of LCZ and using generic range of urban canopy parameters per LCZ, one can estimate toe urban parameter of the area. In this work, we aim to estimate directly the actual distribution of λ_p based on the proposed land use classification method rather than classifying LCZs.

The extracted urban areas were used as the main data for predicting satellite-derived λ_p as well as for updating the existing land use/cover available in the WRF model. The latest available MODIS 20-class land use/cover provided in the WRF model still underestimates the urban area in developing megacities such as Jakarta and Istanbul as they have experienced very rapid urban sprawl over year 2000-2010 in which MODIS data were ensemble. Previous studies mentioned that improved urban representation would have a significant effect on the

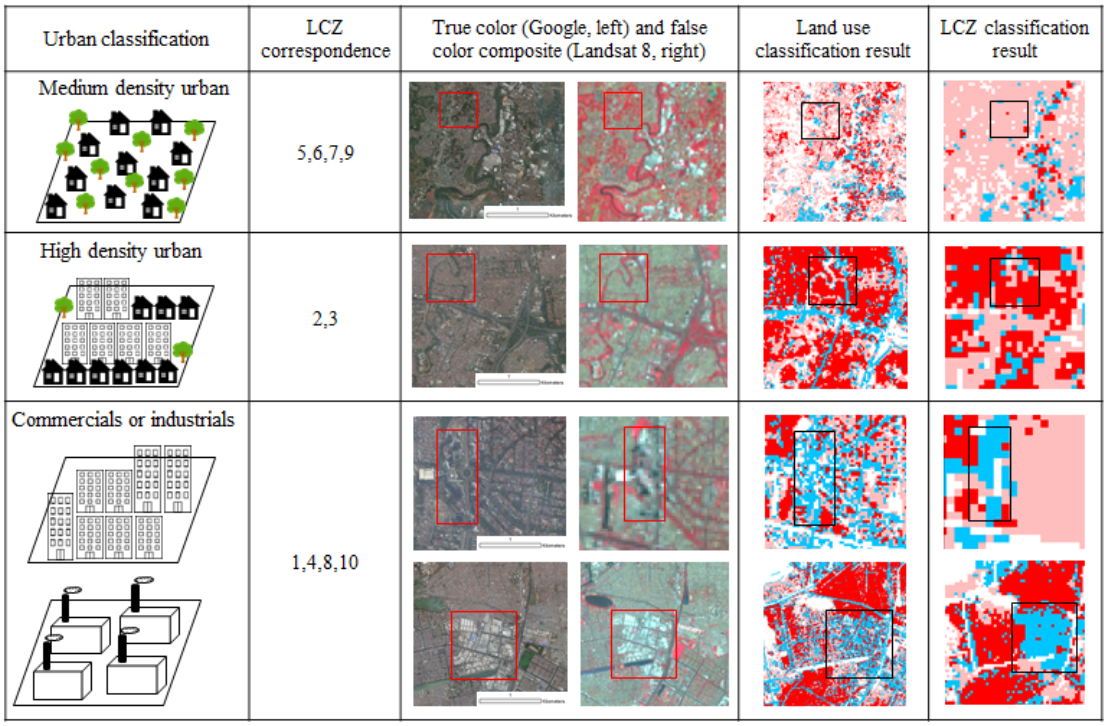

Figure 3.3: Urban classification comparison of current study method and WUDAPT Level 0

mesoscale simulation result (Le Bras and Masson, 2015; Li et al., 2013). Hence, updating urban representation is an essential procedure in urban weather and climate simulation. The urban area extracted from Landsat 8 was used to update the MODIS 20-class land-use/cover geodatabase in any study area of interest.

3.2.2 Empirical equation used for determining λ_p and λ_f

Empirical equation is calculated by OLS using existing real $\lambda_{p_{real}}$ as dependent variable and three urban ratios as independent variables multiplied by three unknown coefficients $\alpha_1, \alpha_2, \alpha_3$ for each urban ratio. Urban ratio defined as the area fraction occupied by specific urban class compared with total area of all urban and non-urban values in a 1km grid. Therefore, there are three urban ratios in

the area inside a 1km resolution grid, derived as:

$$\begin{aligned} r_{U_{med}} &= \frac{\text{total area of } U_{med} \text{ in 1km grid}}{\text{total area of 1km grid}} \\ r_{U_{hi}} &= \frac{\text{total area of } U_{hi} \text{ in 1km grid}}{\text{total area of 1km grid}} \\ r_{U_{ind}} &= \frac{\text{total area of } U_{ind} \text{ in 1km grid}}{\text{total area of 1km grid}} \end{aligned} \tag{3.1}$$

where $r_{U_{med}}$, $r_{U_{hi}}$, $r_{U_{ind}}$ denote the medium-density, high-density, and commercial urban ratio. The designated equation is as follows,

$$\begin{aligned} \lambda_{p_{predict}} &= \alpha_1(r_{U_{med}}) + \alpha_2(r_{U_{hi}}) + \alpha_1(r_{U_{ind}}) \\ \lambda_{p_{predict}} &\approx \lambda_{p_{real}} \end{aligned} \tag{3.2}$$

where $\lambda_{p_{predict}}$ is predicted value of λ_p and $\lambda_{p_{real}}$ is the actual λ_p, both in 1km grid bulk parameters.

The $\lambda_{p_{real}}$ values for Tokyo were taken from MAPCUBE data from CAD Center, Japan. The $\lambda_{p_{real}}$ for Istanbul was calculated from Istanbul real building data provided by the Turkish government, and that for Jakarta was extracted from a map image provided by Here Maps using simple image processing to extract a building footprint from the map. In this method, seven $\lambda_{p_{real}}$ databases were used: Tokyo $\lambda_{p_{real}}$; Istanbul $\lambda_{p_{real}}$; Jakarta $\lambda_{p_{real}}$; Tokyo and Istanbul combined $\lambda_{p_{real}}$; Tokyo and Jakarta combined $\lambda_{p_{real}}$; Jakarta and Istanbul combined $\lambda_{p_{real}}$; and Tokyo, Jakarta, and Istanbul combined $\lambda_{p_{real}}$. The result of $\lambda_{p_{predict}}$ from Equation 3.2 was compared to the $\lambda_{p_{real}}$ in corresponding grid to evaluate Pearson correlation value. From these databases, seven variations of $\lambda_{p_{predict}}$ equations were created (Table 3.1), with each equation having its own combination value of $\alpha_1, \alpha_2, \alpha_3$. From these equations, we selected those deemed suitable for Tokyo, Jakarta, and Istanbul using their Pearson correlation coefficient values and root mean squared error (RMSE) (Table 3.2). Equation $\lambda_{p_{predict}}$ (6) and $\lambda_{p_{predict}}$ (7) both have high

Real λ_p data	df	OLS coefficient			OLS equation
		α_1	α_2	α_3	
Tokyo	575	0	0.37	0	$\lambda_{p_{predict}}$ (1)
Istanbul	2039	0.02	0.47	0.03	$\lambda_{p_{predict}}$ (2)
Jakarta	115	0.17	0.52	0.27	$\lambda_{p_{predict}}$ (3)
Tokyo + Istanbul	2614	0.05	0.4	0.04	$\lambda_{p_{predict}}$ (4)
Tokyo + Jakarta	690	0.06	0.34	0.39	$\lambda_{p_{predict}}$ (5)
Jakarta + Istanbul	2154	0.01	0.48	0.1	$\lambda_{p_{predict}}$ (6)
Tokyo + Jakarta + Istanbul	2729	0.03	0.4	0.13	$\lambda_{p_{predict}}$ (7)

Table 3.1: Coefficients predicted from the seven real λ_p databases for use in Equation 3.2

OLS equation	Tokyo		Istanbul		Jakarta		Average	
	$R_{Pearson}$	RMSE	$R_{Pearson}$	RMSE	$R_{Pearson}$	RMSE	$R_{Pearson}$	RMSE
$\lambda_{p_{predict}}$ (1)	0.730	0.080	0.912	0.060	0.910	0.120	0.851	0.087
$\lambda_{p_{predict}}$ (2)	0.720	0.108	0.914	0.047	0.907	0.175	0.847	0.110
$\lambda_{p_{predict}}$ (3)	0.696	0.160	0.887	0.086	0.930	0.030	0.838	0.092
$\lambda_{p_{predict}}$ (4)	0.722	0.087	0.914	0.050	0.910	0.140	0.849	0.092
$\lambda_{p_{predict}}$ (5)	0.650	0.090	0.846	0.065	0.890	0.086	0.795	0.080
$\lambda_{p_{predict}}$ (6)	0.720	0.120	0.910	0.048	0.920	0.090	0.850	0.086
$\lambda_{p_{predict}}$ (7)	0.710	0.090	0.910	0.050	0.920	0.120	0.847	0.087

Table 3.2: Pearson's correlation coefficient and RMSE of coefficients from equations $\lambda_{p_{predict}}$ (1)–(7)

correlation coefficients and least RMSE for their relation with the three cities' $\lambda_{p_{real}}$. Thus, based on these two equations, we found a range of applicable $\alpha_1, \alpha_2, \alpha_3$ values that could be used for deriving λ_p from Landsat 8 images of other cities: $\alpha_1 = 0.01 \sim 0.03$, $\alpha_2 = 0.4 \sim 0.5$, and $\alpha_3 = 0.1 \sim 0.13$.

To assess the sensitivity of $\alpha_1, \alpha_2, \alpha_3$ ranged values, the minimum and maximum values of each coefficient range were sorted into eight possible combinations, then applied in Equation 3.2 for Istanbul, Tokyo, and Jakarta, and were tested to determine any effect of their intervariability on λ_p real. The λ_p values predicted from these combinations were then compared with the respective λ_p real through a

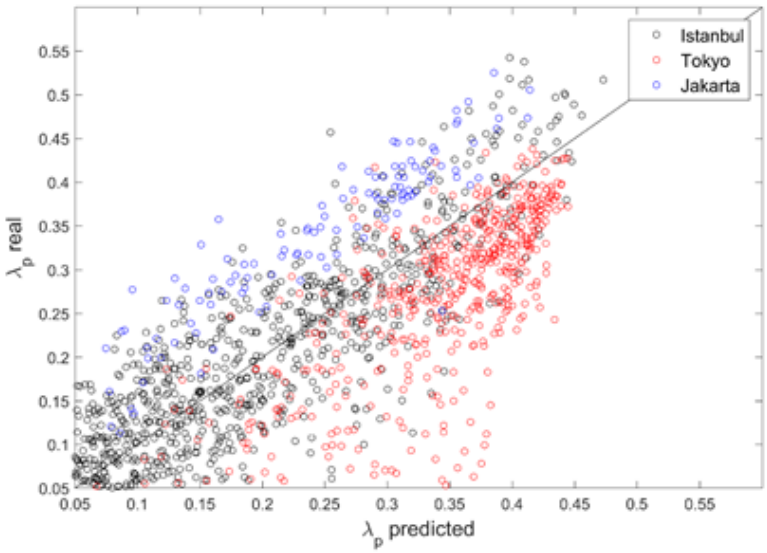

Figure 3.4: Relationship of λ_p real and λ_p predicted

correlation analysis. Results showed that λ_p predicted values had deviations with actual ones. However, the highest standard deviation was less than 0.06, which is not significant in this framework. Thus, the range of $\alpha_1, \alpha_2, \alpha_3$ coefficients was deemed applicable for this method.

Using $\alpha_1, \alpha_2, \alpha_3$ values of 0.01, 0.5, and 0.1, respectively in Equation 3.2 for Istanbul, Tokyo, and Jakarta to compare λ_p real and λ_p predicted, we found that the predicted value agreed well with the actual one with Pearson correlation coefficient value of 0.84, 0.51, and 0.87 for Istanbul, Tokyo and Jakarta respectively (Figure 3.4). The two-dimensional spatial relationship between λ_p real and λ_p predicted also showed good agreement between the two parameters (Figure 3.5).

Even though λ_p and λ_f stand as independent parameter, Kanda et al. (2013) found their relationship in quadratic function as stated in Equation 3.3. The function is derived from real building datasets in Tokyo which also applicable for Toulouse, Berlin, Salt Lake City, Los Angeles, and London. The applicable range

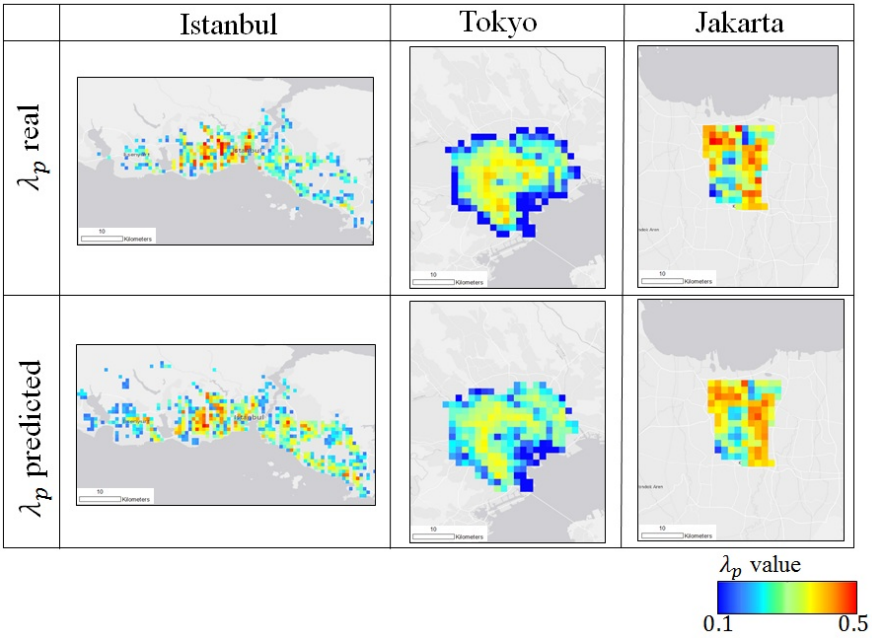

Figure 3.5: Spatial distribution between λ_p real and λ_p predicted in 1km resolution grid

of the equation is $0.45 \geq \lambda_p \geq 0.05$. The $\lambda_{f_{predict}}$ calculated from the $\lambda_{p_{predict}}$ had a Pearson's correlation coefficient of 0.87 with $\lambda_{f_{real}}$ for Tokyo. The other two cities were validated using available dataset and it is shown that their trends are still following Equation 3.3 (Figure 3.6). The available dataset for validation in Istanbul is only available for year 2005. For Jakarta, the validation data is limited to 59 1km grid data which is processed and verified using combination of recent Google Maps, Here Maps, available building data from PASCO Japan, and Digital Surface Model (DSM) data from PASCO Japan.

$$\begin{aligned} \lambda_f &= 1.42\lambda_p^2 + 0.4\lambda_p, \\ \text{for } & 0.45 \geq \lambda_p \geq 0.05 \end{aligned} \tag{3.3}$$

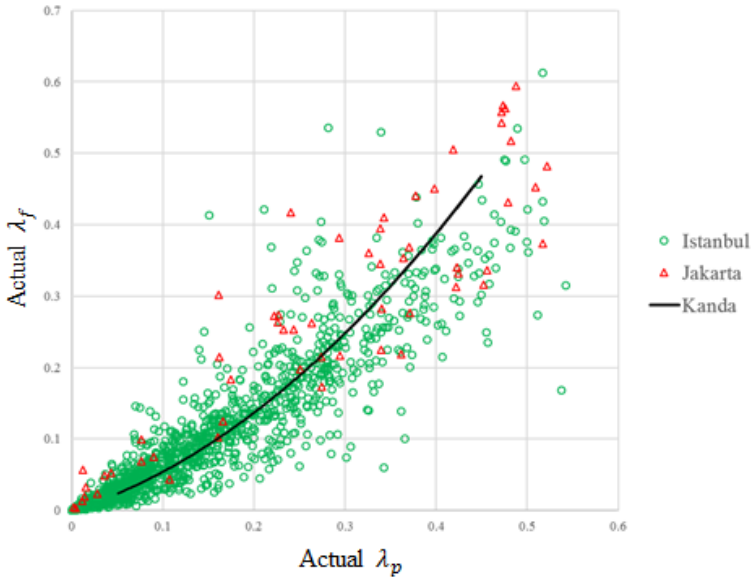

Figure 3.6: Correlation between actual λ_p and λ_f for Istanbul and Jakarta, vs. Kanda et al. (2013)'s empirical function in Equation 3.3 (solid line). It showed that the relationship of actual λ_p and λ_f following Kanda et al. (2013) equation.

3.3 Estimation of H_{ave}

In this study, we used the latest version of 30m ASTER GDEM Version 2 (released 2011) (henceforth, ASTER GDEM) and 7.5-arc-second GMTED 2010 minimum values (henceforth, GMTED), both of which are publicly available. Study by (Tachikawa et al., 2011) resulted that ASTER is considered to have positive offsets on elevation due to buildings or forest canopies. Several experiments were conducted on how to extract ASTER GDEM positive offset which may correlate with building canopy height in urban area. Our study found that the elevation difference between the ASTER GDEM maximum value, and the GMTED (i.e. corresponds to the elevation of the real topography) has a potential in estimating height of surface roughness elements. Simplified illustration regarding the process is shown at Figure 3.7. We refer to the elevation difference between ASTER GDEM and GMTED as the assumed average height surface roughness element.

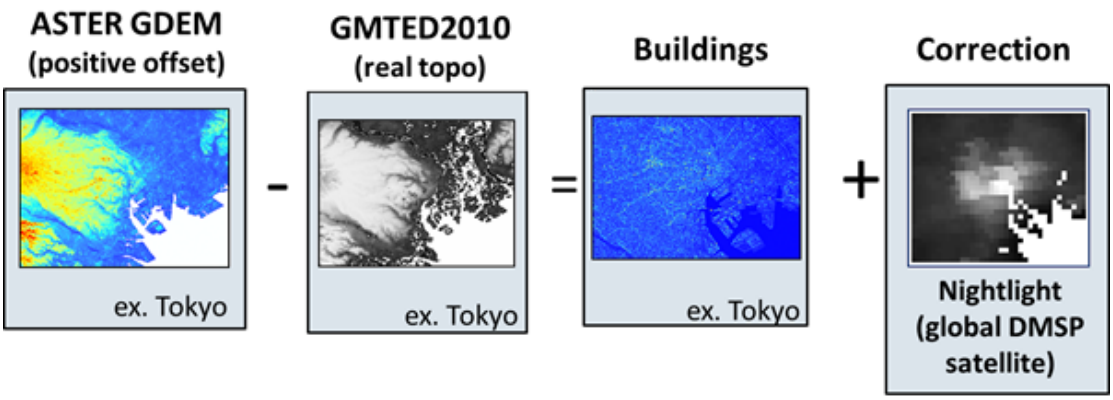

Figure 3.7: Illustration of "artifact"extraction on ASTER GDEM

In urban areas, it is presumed to be the tops of buildings canopy and represents Have. The elevation difference was calculated using GIS software by subtracting the maximum elevation value of ASTER GDEM in a 1km grid from the corresponding 1km average GMTED value (henceforth, ASTER-GMTED).

A reference of actual H_{ave} distribution in 1km resolution was calculated from a high-resolution 3D building map of Tokyo and Nagoya, MAPCUBE -a product of CAD Center, Japan-. A grid-by-grid comparison and correlation analysis were conducted between the reference H_{ave} and the elevation difference. We limited the comparison to urban areas defined by $\lambda_p > 0.2$, following the study of Kanda et al. (2013), since $\lambda_p < 0.2$ were all classified as non-urban land use in Tokyo and have less effect on drag. Furthermore, our study showed that ASTER GDEM tend to "flatten"$\lambda_p < 0.2$ area and detect vegetation canopy rather than building canopy in these areas. This was achieved by masking the study area with the predicted λ_p estimated from the previous section. Following this condition, urban land use with $\lambda_p < 0.2$ was all assigned with H_{ave} value of $3.5\mathrm{m}$, equal to one floor average residential building height.

An exponential relationship was found between bulk 1km H_{ave} parameter calculated from MAPCUBE and ASTER-GMTED. However, this relationship was

not strong enough to be directly use as empirical function since nearly half of the ASTER-GMTED values overestimates real value, especially in $10.0\text{m} \leq H_{ave} \leq 30.0\text{m}$. This made our decision to make use of other available datasets to improve the relationship.

The global OLS radiance-calibrated NL dataset, downloaded from the DMSP-OLS satellite, is capable of capturing the urban centers of large cities (Hsu et al., 2015; Huang et al., 2016) because highly populated areas tend toward greater luminosity than their surrounding areas (Sutton, 1997; Sutton et al., 2006). Study by Dong et al. (2017) stated that nighttime lights are closely correlated with economic activities, for example the more commercialized an area is, the higher energy used due to night lighting. In most Asian megacities, highly populated and commercialized area seems well correlated with high-rise building area. Therefore, it is expected that is connection between NL luminosity and building height. This luminosity is represented by the radiance value, in DN units, with higher DNs corresponding to brighter areas.

The current study found that NL radiance value has a linear relationship with the reference actual H_{ave} data. To assess whether NL database could support ASTER-GMTED, NL and ASTER-GMTED were combined and resampled into 1km grids, then used as independent variables in the same way as section 3.2.2, in order to find empirical function to predict H_{ave}. In particular, the best-fit equation using polynomial approximation relationship is found problematic ($H_{ave_{predict}} = 0.1(ASTER - GMTED)^{1.25} + 0.01(NL)$).

It underestimated the resulting values by up to 20m H_{ave} for extremely high building area in Tokyo and Nagoya. To solve this problem, a feedforward artificial neural network (ANN) was used to obtain H_{ave} prediction using data obtained from Tokyo (554 input data, 380 training samples) and Nagoya (142 input data, 99 training samples). ASTER-GMTED was used as the first input neuron, and

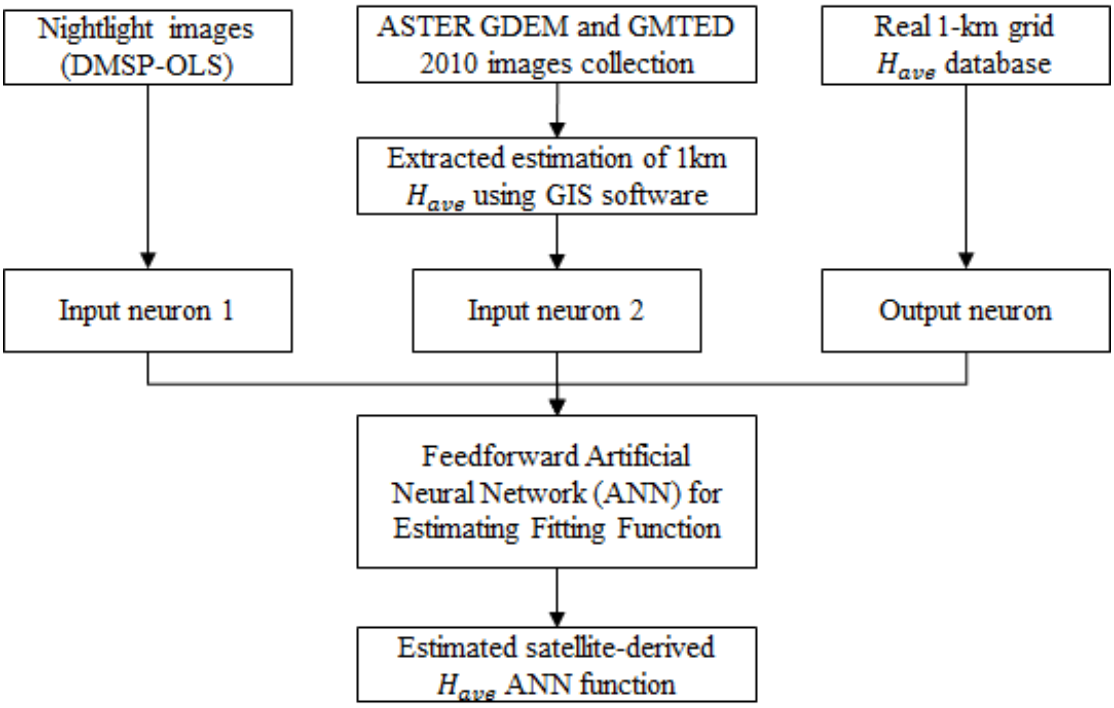

Figure 3.8: Workflow of estimating H_{ave} from satellite imageries

the DMSP-OLS nightlight image was used as the second input neuron. The work flow of estimating H_{ave} from satellite imageries is show in Figure 3.8.

The output neuron was each city's reference H_{ave}, calculated from MAPCUBE. Ten hidden layers and four hidden layers were used to create the Tokyo and Nagoya ANN functions, respectively, and generalization was provided by following rule three of feedforward ANN (FrontlineSolvers, 2018). An inter-comparison using the Tokyo ANN function for Nagoya and vice versa was conducted to define a general empirical ANN function. It showed that the Nagoya ANN function worked better for both Tokyo and Nagoya than did the Tokyo ANN function (Figure 3.9). This may be due to the more complex and heterogeneous building morphology in Tokyo compared to Nagoya. The Nagoya ANN function was applied to define H_{ave} for all cities in the study. A validation with available actual H_{ave} dataset for Jakarta and Istanbul was conducted and the results supported that both cities followed well with Nagoya fitting function (Figure 3.10). The spatial distribution of the real and predicted H_{ave} values is shown in Figure 3.11. These results further support the idea that ASTER-GMTED combined with the DMSP-OLS nightlight image was used to determine H_{ave}, which is a crucial morphological parameter for calculating urban roughness. However, a few overestimated values were also detected, especially for areas packed with very tall buildings ($H_{ave} \geq 30m$) such as Shinjuku in Tokyo.

3.4 Estimation of other urban parameters

The σ_H and H_{max} values were calculated following Kanda et al. (2013) as written in Equation 3.4. Finally, the distribution of two bulk aerodynamic parameters, d and z_0, was attained from the estimated building morphological parameters (Kanda et al., 2013) (Equation 3.5 and 3.6). We referred to these parameters as

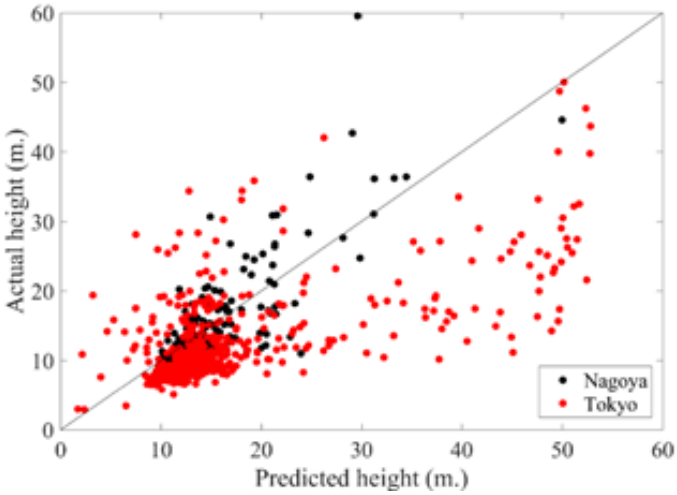

Figure 3.9: Artificial neural network result on H_{ave} approximation for Tokyo and Nagoya

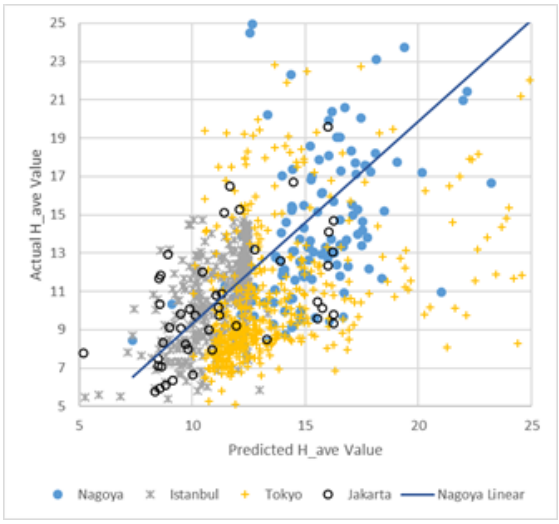

Figure 3.10: Correlation between predicted H_{ave} value with actual H_{ave} in 1km resolution for three cities. It showed that predicted H_{ave} in Istanbul and Jakarta (calculated using ANN function for Nagoya) follow the same trend with Nagoya and reflects their actual H_{ave} value.

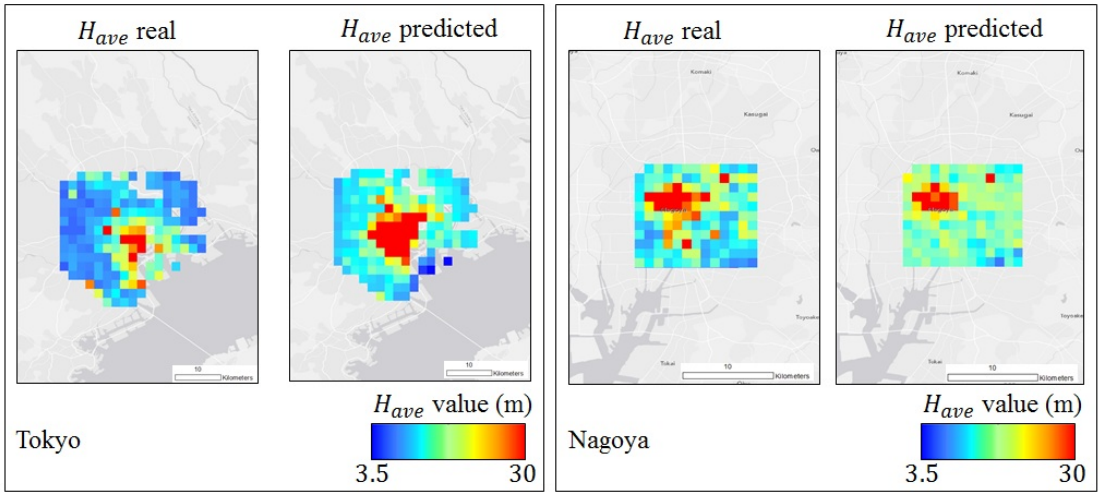

Figure 3.11: Spatial distribution between H_{ave} real and H_{ave} predicted in 1km resolution grid

urban parameters derived from global datasets.

$$\begin{aligned} H_{max} &= 12.51\sigma_H^{0.77} \\ \sigma_H &= 1.05H_{ave} - 3.7 \end{aligned} \tag{3.4}$$

$$\begin{aligned} \frac{d}{H_{max}} &= c_0X^2 + X(a_0\lambda_p^{b_0} - c_0) \\ X &= \frac{\sigma_H + H_{ave}}{H_{max}} \quad , \quad 0 \leq X \leq 1.0 \\ a_0 &= 1.29; b_0 = 0.36; c_0 = -0.17 \end{aligned} \tag{3.5}$$

$$\begin{aligned} \frac{z_0}{z_0(mac)} &= b_1Y^2 + c_1Y + a_1 \\ Y &= \frac{\lambda_p\sigma_H}{H_{ave}} \quad , \quad 0 \leq Y \\ a_1 &= 0.71; b_1 = 20.21; c_1 = -0.77 \end{aligned} \tag{3.6}$$

Because d and z_0 are critical parameters in the WRF model coupled with urban aerodynamic parametrization, the sensitivity to the 8 possible $\alpha_1, \alpha_2, \alpha_3$ coefficients combination in Equation 3.2 was also tested (i.e., combination without

replacement of minimum and maximum values from each α coefficient, hence $2^3 = 8$ combinations). The intervariability of d and z_0 based on the various coefficients was assessed through a cross correlation. A correlation matrix analysis of eight possible d and z_0 values created from the combination of $\alpha_1, \alpha_2, \alpha_3$ coefficients found that for Jakarta, all the combinations resulted in a similar sensitivity, with no large intervariability shown by a Pearson correlation coefficient ≈ 1. Therefore, there was no significant different among these eight combinations of $\alpha_1, \alpha_2, \alpha_3$ relative to d and z_0. Thus, any random numbers assigned to $\alpha_1, \alpha_2, \alpha_3$ within the allowable range would yield negligible variability in d and z_0. Hence, d and z_0 were confidently constructed for Jakarta using $\alpha_1, \alpha_2, \alpha_3$ values of 0.01, 0.5, and 0.1, respectively.

3.5 Discussion

Currently, the constructed urban parameters dataset is sufficient enough for the mesoscale modelling purpose. The complete set of urban paremeters is shown in Figure 4.1. Subsequently, the distributed satellite-derived urban parameters, which can also be frequently updated, can serve as a good substitute for actual urban parameters calculated by actual 3D building database in the estimation of urban parameters. It provides simple and zero-cost solution to developing cities that mostly lack of actual building database such as Asian megacities. One distinct limitation of using satellite imageries in building parameters is due to coarser resolution of the imageries, hence the "smoothing" or "blooming" effect appear and underestimate the value from real urban parameters. More advanced satellite imageries may resolve this limitation, assuming there is no constraint on funding.

Overall, the present study contributes an alternative way for urban climate community in creating actual urban morphological parameters database when

local experts knowledge is limited and require less workforces. Moreover, the findings of this study could be integrated with the new WRF model version that supports LCZs-based detailed urban land use, thus the integration is expected to give better model results of urban atmospheric phenomena. Further work needs to improve the calculation of H_{ave}, which is limited to the area of $\lambda_p > 0.2$, and could potentially affect the estimated H_{ave} in less urbanized urban areas. Combining open-source actual building data into the H_{ave} could offer a solution. Future research should therefore give more attention to urban morphological data validation especially in megacities in other countries to enrich the urban datasets. Larger datasets also could act as a foundation to conduct an investigation on how region or economic factor of a country affects urban morphological characteristic to give more precise estimation of megacities urban structure.

For some desert cities, the land-use classification might be challenging, and further investigation is needed, especially in defining urban areas. Application of other land use classification algorithm such as random forest is one of the solution for this matter. In addition, cloud-based land use classification such as Google Earth Engine could provide brand-new perspective by maintaining speed and global extent. Based on this study, we encouraged more approach to big data and data science for urban climate research. Therefore, a solid global teamwork consisting scientist, engineers, urban planner, governmental, and other related stakeholders is very much worthwhile.

3.6 Summary

Following the advances made in urban parametrization in weather models and with the need for accurate weather simulations in urban areas, there is a growing demand for distributed urban parameters for cities around the world. Most cities, especially in developing countries, have limited or no building distribution datasets

for use in calculating the required urban parameters in the SLUCM/WRF. Therefore, in present study we proposed simple and zero-cost methods to estimate the actual distributed urban morphological parameters from variety of satellite images combination.

Landsat 8 satellite images were investigated for their capability to estimate the plane and frontal area indices, λ_p and λ_f, respectively. Empirical equations were derived to estimate λ_p and λ_f from Landsat 8 images. Good agreement was achieved when they were compared with the actual λ_p and λ_f values.

Using a neural network, subtracted ASTER-GMTED data were combined with the DMSP-OLS nightlight image to define a function for deriving H_{ave} from satellite images focused on Tokyo and Nagoya. Using the H_{ave} function for Nagoya resulted in a good agreement between the real and satellite-derived H_{ave} in Tokyo and Nagoya. This function was later used to estimate the H_{ave} distribution of Jakarta and later, other preferred cities.

The urban aerodynamic parameters of d and z_0 were then estimated following a method proposed by Kanda et al. (2013), using the earlier urban morphology parameters derived from global datasets. All of the urban parameters were produced in a 1km resolution grid for application in a WRF model simulation for Jakarta (Chapter 4).

4

Satellite-derived urban roughness parametes performance in WRF mesoscale model

4.1 Introduction

This chapter is aimed to assess the performance of urban parameters constructed in Chapter 3 in WRF/SLUCM environment. We compared two simulation cases, the modified WRF/SLUCM using distributed urban parameters from global satellite datasets (SAT) and default SLUCM/WRF with fixed urban parameters value (DEF), to determine how the model performed in reproducing the urban climate in one of the world's largest developing megacities, Jakarta, Indonesia. The detailed different between SAT and DEF case is shown on Table 4.1. The completed

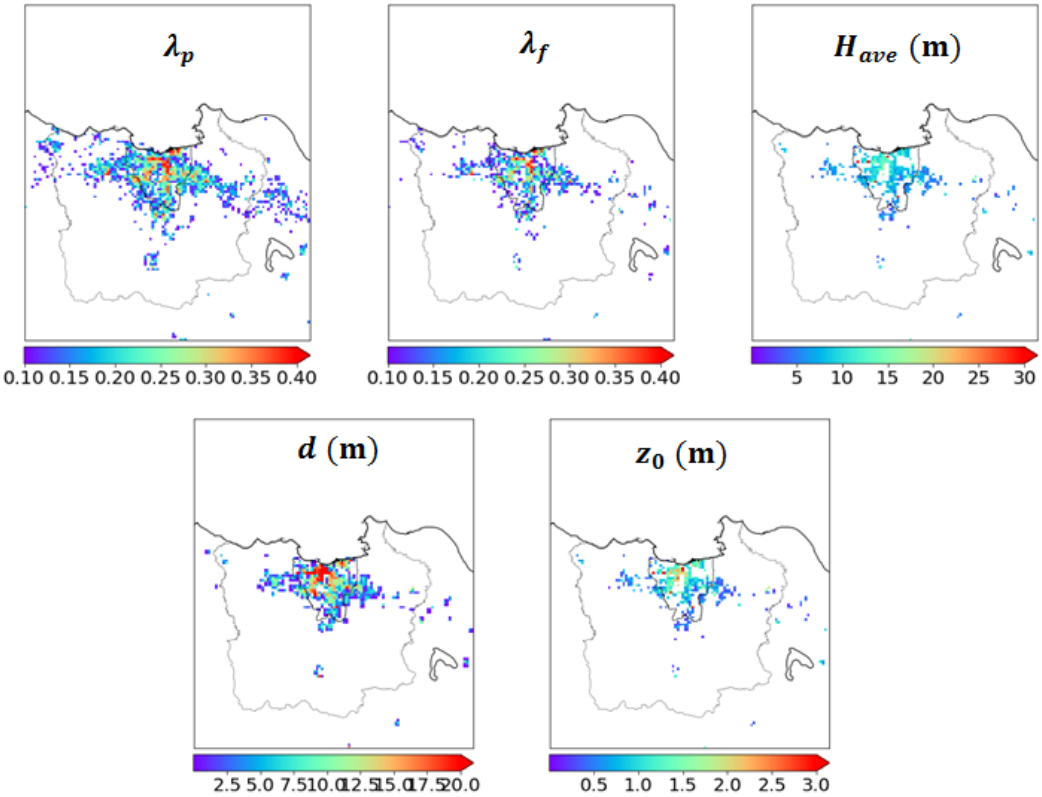

Figure 4.1: Urban morphological and aerodynamical parameters for the WRF/SLUCM model geographical boundary in 1.2km resolution

urban parameters set made in Chapter 3 (Figure 4.1) were then processed into WRF model-compatible geographic boundary data for Jakarta and added to the geographical input boundary.

4.2 Simulation settings

As mentioned in 3.1, the numerical model that is used to assess the urban parameters performance is using WRF/SLUCM improved by urban aerodynamic parameterization (Kanda et al., 2013). We used a modified SLUCM (Kusaka et al., 2001; Kusaka and Kimura, 2004) incorporated into the Weather and Research Forecasting (WRF) model ver. 3.3.1. The modifications are as follows:

- The estimations of the bulk transfer coefficients for each building facet have been revised based on the Simple Urban Energy Model for Mesoscale Simulation (SUMM) (Kanda et al., 2005b,a).
- The actual urban fractions were considered rather than the constant values used in the default WRF model (Kanda et al., 2013; Varquez et al., 2015).
- Gridded sky-view factors derived from the urban parameters were considered (Varquez et al., 2015).
- The effect of vegetation on the local bulk heat transfer coefficient was considered (Kawai et al., 2009).

Further descriptions of the modified WRF can be found at `http://www.ide.titech.ac.jp/~kandalab/download/WRF_URBAN/add_improvements.html`.

Two simulation cases were conducted to analyze the effect of urban parametrization on the urban climate in Jakarta using WRF 3.3.1 coupled with SLUCM. The first case (SAT) used the satellite-derived distributed urban parameters (i.e., WRF/SLUCM with modified urban aerodynamic parametrization), whereas the second case (DEF) used the default SLUCM fixed urban parameters (i.e., WRF/SLUCM without modified urban aerodynamic parametrization). The simulation was conducted for the full month of August 2014, which is within the dry season, with an additional 16 days for model spin up. Both cases use same domain spatial boundaries with one parent and two nested domains: reference longitude 106.84° and latitude -4.7°; domain resolution 30-km, 6-km, 1.2-km (Figure 4.2); parent grid ratio 1, 5, 5; i parent start 1, 33, 65; j parent start 1, 34, 42; distance in x-direction 95, 111, 116; distance in y direction 100, 101, 136; dx 30000; dy 30000; all domains use 40 vertical levels. One-way nesting was used (i.e., no feedback of simulated values from finer to coarser domains).

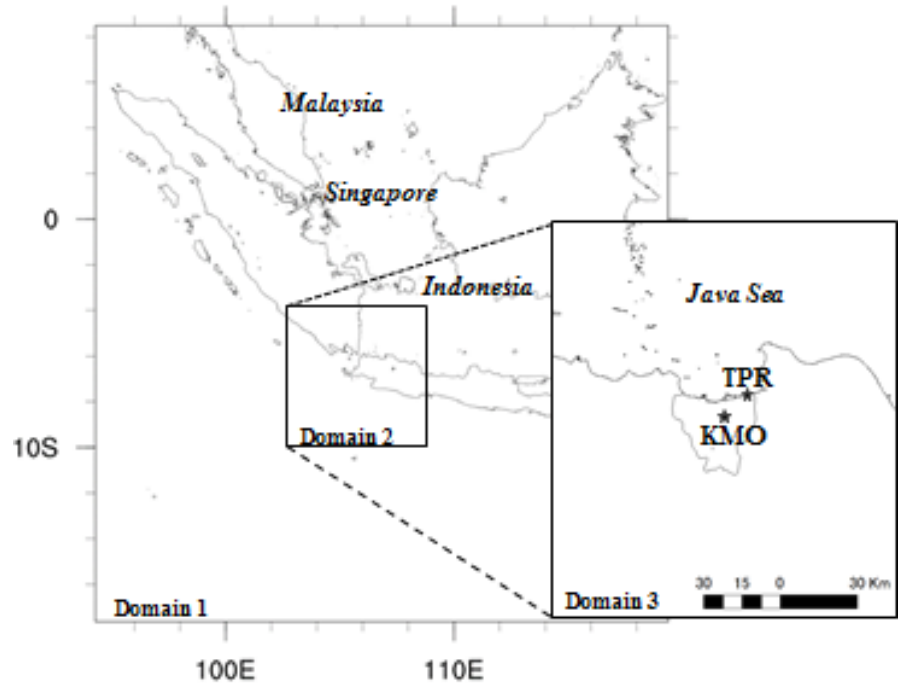

Figure 4.2: Domain setting for Jakarta August 2014 simulation

Due to scarcity of on-site point data observation, two synoptic observation stations for near-surface temperature and wind speeds in 1-hour temporal resolution were used for validation: Kemayoran station (KMO) 106.8418E, 6.1556S and Tanjung Priok station (TPR) 106.8778E, 6.111S. Both of these stations are classified as urban station and follows WMO flat-grassland station standard with WMO code 96745 and 96741 respectively. KMO station is located in commercial/industrial class in our classification and TPR in high-dense urban area. For LCZ class, KMO is located in class 1 (compact high-rise) and TPR is located in class 2 (compact mid-rise). KMO is surrounded by high-rise building especially on the north-west side of the station which largely influences observation records quality.

The National Centers for Environmental Prediction Final (NCEP-FNL) global weather data archive with 6-hour temporal and $1° \times 1°$ spatial resolutions

were used for the lateral and initial meteorological boundary condition. The 4-km MODIS monthly day and night sea surface temperature (SST) data were used in both cases as the initial boundary. An update of the MODIS 20-class land use referred to in section 3.2.1 was used. A summary of both cases is shown in 4.1. Both cases used the physical settings of: shortwave radiation scheme by Dudia; longwave radiation scheme RRTM; Microphysics New Thompson; Kain-Fritsch cumulus parametrization; and planetary boundary layer Mellor-Yamada 2.5.

Adding anthropogenic heat emission (AHE) and urban parameters in WRF/SLUCM simulations resulted in a better wind and temperature interpretation (Varquez et al., 2015). However, in this chapter, our focus is on comparison of with and without using urban parameterization which built from satellite-derived urban parameters calculated previously in Chapter 3. Therefore, we would like to eliminate the effect of AHE in the simulation to see urban parameters individual effect. Our target here is to answer whether satellite-derived parameters can improve the default setting or not, and less targeting on how close the result will be with observation data. Exclusion of AHE also considering the insensitivity of AHE component in the simulation as we did experiment by comparing control_case (i.e. without AHE and distributed urban parameters), AHE_case (i.e. inclusion of AHE, without distributed urban parameters), and param_case (i.e. inclusion of distributed satellite derived urban parameters, without AHE). The results are shown in Figure 4.3. It can be seen that both TPR and KMO AHE_case value insignificantly changed compared with control case in our target location. However, the urban parameter case shows significant different with AHE_case as it deviates much from the control case especially on wind speed. The possible reason for AHE insensitivity is due to magnitude of AHE compared with radiation heat flux (i.e. shortwave and longwave) and turbulent heat flux (e.g. sensible and latent). The maximum AHE is less than $70 W/m^2$ with typical

Parameters	Cases	
Case name	DEF	SAT
WRF version	Default WRF/SLUCM Version 3.3.1	Modified WRF/SLUCM Version 3.3.1
Roughness length $z_0(m)$	SLUCM default 0.53^{*1} , 0.33^{*2} , 0.17^{*3}	Distributed z_0 from global dataset
Displacement height $d(m)$	SLUCM default 7.62^{*1} , 5.72^{*2} , 3.81^{*3}	Distributed d from global dataset
Urban fraction	SLUCM default 0.95^{*1} , 0.9^{*2} , 0.5^{*3}	Modified distributed urban fraction with second dominant
Plan area index λ_p	SLUCM default 0.5^{*1} , 0.5^{*2} , 0.5^{*3}	Distributed λ_p from global dataset
Frontal area index λ_f	SLUCM default 0.5^{*1} , 0.4^{*2} , 0.3^{*3}	Distributed λ_f from global dataset
Average building height $H_{ave}(m)$	SLUCM default 10.0^{*1} , 7.5^{*2} , 5.0^{*3}	Distributed H_{ave} from global dataset

Table 4.1: Urban boudaries description for the DEF and SAT simulation cases. The (^{*1}) marked values refer to commercial urban area, (^{*2}) marked values refer to high density residential area, and (^{*3}) marked values refer to low density residential area.

range of $10 - 50 W/m^2$. This value is lower than the order of magnitude of heat energy due to radiation and turbulent flux as shown in Figure 4.4.

4.3 Results and Discussion

The modification on roughness parameters in this study has higher impact on near-surface wind field rather to temperature due to aerodynamic change effect. The simulated result for Jakarta wind speed and temperature was compared with the hourly synoptic reports from the two stations (Figure 4.5 and 4.6). For the whole month, the simulated 10-m wind speed was mostly overestimated in both cases. Large discrepancy of KMO station observed and simulated values is considered correspond to the station location where it is surrounded by high-rise

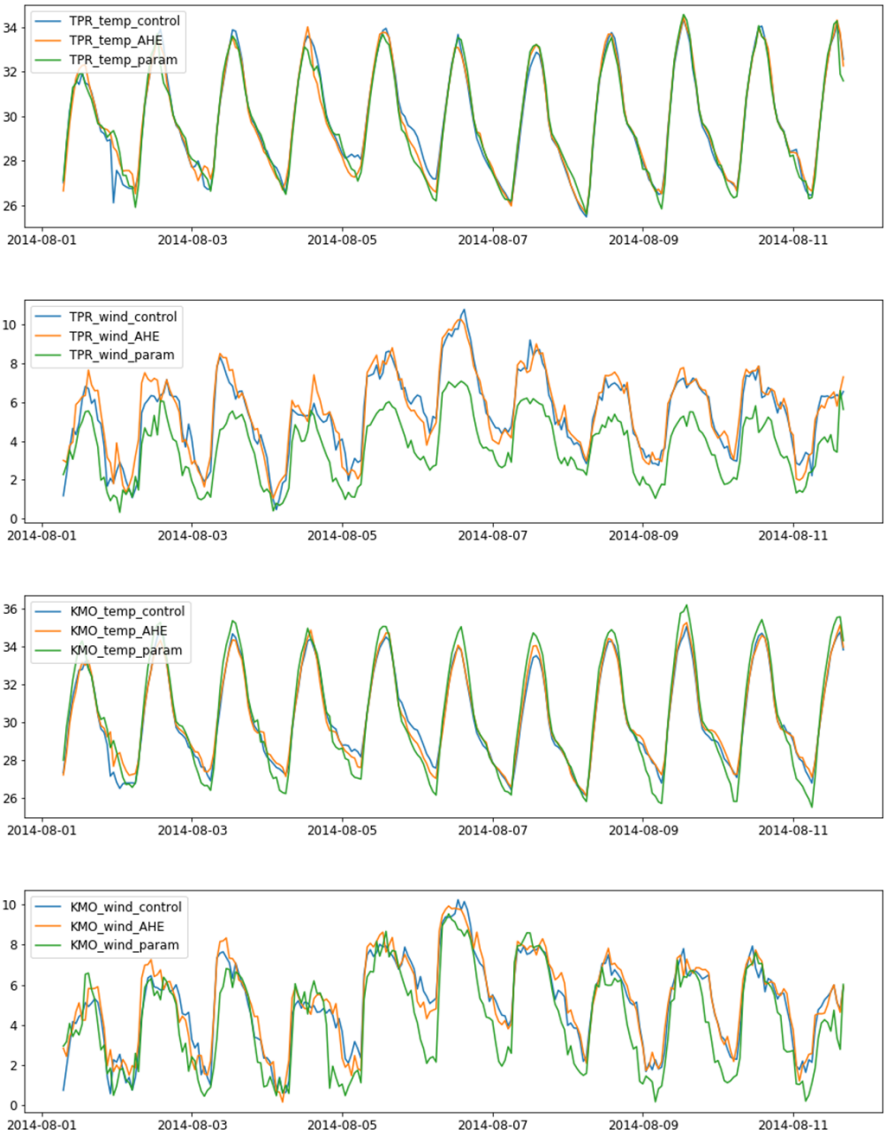

Figure 4.3: Graph on comparison on control_case, AHE_case, and param_case

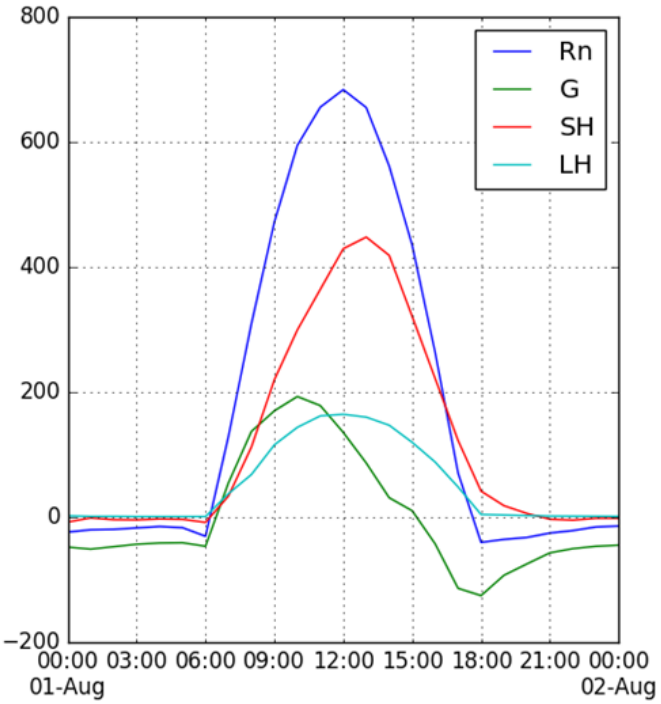

Figure 4.4: Example of simulation result on energy budget. Rn denotes radiation budget (i.e. shortwave and longwave radiation), SH denotes sensible heat flux, and LH denotes latent heat flux. Here, AHE is included in sensible heat flux (SH) component. Unit in $\mathrm{W/m^2}$

building, especially right on the north-west direction of the station thus results in false records. TPR is considered have reliable observation records compared with KMO. Regardless of the locations, it is commonly known that coupling the default settings of UCM with WRF has a tendency to overestimate near-surface wind speeds and insufficiently reproduce the surface drag (Nelson et al., 2016). Therefore, improvement of roughness parameter is necessary to improve surface drag calculation as we did in this research. Unfortunately, as mentioned in 3, the satellite-derived urban parameters are tend to underestimate the average building height, hence affect lower roughness than reality. The underestimation value increasingly happened in compact high-dense area such as KMO, hence also causing why large bias happening there.

With regard to near-surface wind speed, SAT had lower RMSE and bias values at both stations than did DEF. This points out that using current developed urban roughness improves the performance of WRF/SLUCM. A daytime and nighttime statistical comparison, shown in Table 4.3, revealed that large wind speed biases mostly occur during daytime for both cases. Simulated near-surface wind speeds during nighttime show better agreement with observed values, especially in SAT. Shown in Table 4.3, the daytime RMSE values for SAT were 2.04 (TPR) and 4.06 m/s (KMO), whereas for DEF, they were 3.55 (TPR) and 4.17 m/s (KMO). The daytime bias values for SAT were 1.36 (TPR) and 3.69 m/s (KMO), whereas for DEF, they were 3.06 (TPR) and 3.87 m/s (KMO). During nighttime average wind speed, the SAT had RMSE values of 1.40 and 1.62 m/s for TPR and KMO, respectively, whereas in DEF, the RMSE values were 2.61 and 2.87 m/s for TPR and KMO, respectively. Nighttime average wind speed of SAT also resulted in significantly lower bias compared to DEF, with values of 0.71 m/s and 0.49 m/s for SAT at KMO and TPR, respectively, and 2.52 m/s and 2.10 m/s for DEF at KMO and TPR, respectively. Better wind speed prediction on SAT

may suggest that a better distribution of $\mathtt{d}$ and $\mathtt{z}_0$, especially in city center (solid circle at Figure 4.8), contributes to the improvement of the simulation result. This area, characterized by high surface roughness enhances surface wind drag, thereby weakening winds. This phenomenon may potentially lead to higher temperatures in high-density areas because weaker winds are associated with reductions in both ventilation and heat advection from the surface.

Both cases overestimated the near-surface temperature during daytime with slightly different bias magnitude. However, SAT performed better at predicting nighttime temperature than did DEF for both stations, especially on the last 10 days of August. In Table 4.2, the RMSE and bias from both two cases and observed near-surface temperature for each station for whole month simulation are shown. The similar results were found for daytime temperature RMSE and bias. At nighttime, KMO SAT had a lower bias (0.05°C) than did DEF (0.80°C). The nighttime RMSE values were 0.98°C and 1.26°C for SAT and DEF, respectively. A simulation by Tursilowati et al. (2012) in the same study area without any modification on urban parameters produced Pearson correlation coefficients of 0.71 and 0.78 for the relationship between simulated and observed temperature at KMO and TPR, respectively, for the period February 2–4, 2004. The SAT simulation resulted in Pearson correlation coefficient values of 0.92 and 0.94 for KMO and TPR in August 2014, respectively. This may indicate that the WRF/S-LUCM with new aerodynamic parameterization improve the simulation result on temperature due to better representation of heat retention caused by wind drag.

Likewise, the positive bias on 2m temperature -especially during daytime- on both cases are apparently related with systematical error due to urban surface energy balance model in SLUCM and land surface model of NOAH-LSM implemented in the model. To date, this problem still one of the most challenging issue for urban climate scientists (Demuzere et al., 2017; Trusilova et al., 2013). It is

indicated that the modified urban energy balance model, following the top-down approach of predicting bulk transfer coefficient on momentum and heat, has underestimate the sensible and latent heat flux (Kawai et al., 2009). In tropical area with high humidity, as the radiative interactions with water vapor is very important, the underestimated latent heat flux could affect urban canopy temperature significantly (Roth et al., 2017). Latent heat flux in urban surface is determined by evapotranspiration process by urban elements and could affect surface cooling mechanism. This hypotheses is backed up with the fact that the model cannot solve near-surface temperature drop after rain event (e.g., August 7 and 9). Study by Demuzere et al. (2017) on inter-compariosn of urban land surface models' performance in a tropical city also shows disagreement on simulated and observed urban energy flux with the highest error on latent heat flux estimation. Furthermore, recent work by Salamanca et al. (2018) stated that NOAH-LSM showed overestimate of energy flux which results in overestimation of near-surface temperature. Further analysis on urban surface model improvement and discussion lies beyond the scope of this study.

In addition, discrepancies between spatial representativeness of simulation result and point observation as validation data, along with location of observation which is surrounded by high buildings (Figure 5.3a and 5.3b), also contribute to the bias. Another validation analysis using land surface temperature data as to measure surface urban heat island (Zhao et al., 2014) is considered problematic (Voogt and Oke, 2003). Due to the urban complexity (i.e., complication on determining the appropriate surface radiative-emissivity parameters, geometrical parameters, canopy radiative transfer) the satellite-detected urban surface temperature is not adequately match and nor represent the real surface temperature. KMO location may determine a lot why such bias is happening. KMO land cover is grass and the grid it contained in is urban land cover with more than 0.8 urban

fraction. Thus it will cause discrepancy between model and real condition especially regarding turbulent heat flux parameters. KMO's location is surrounded by tall buildings. Daytime northerly sea breeze flow is blocked by tall buildings on the north-side of weather station. The findings agree with previous findings by Varquez et al. (2015) from which the methodology was patterned from. They explained that there are factors that influence the accuracy such as the parameterization of transfer coefficients down to the 2-m scale and the representativeness of weather stations in dense cities especially during daytime. Nighttime statistical analysis shows the SAT case in KMO performed very well in reducing wind speed bias. Hence, this correlate to improvement of temperature validation bias from 0.80°C in DEF to 0.05°C in SAT in KMO.

Station	Case	Simulated mean (A)	Observed mean (A)	RMSE (A)	Bias (A)	Simulated mean (D)	Observed mean (D)	RMSE (D)	Bias (D)	Simulated mean (N)	Observed mean (N)	RMSE (N)	Bias (N)
KMO	**DEF**	29.86	29.08	1.48	0.78	31.46	30.69	1.66	0.77	28.17	27.37	1.26	0.80
	SAT	29.77	29.08	1.45	0.70	32.01	30.69	1.78	1.32	27.41	27.37	0.98	0.05
TPR	**DEF**	29.52	28.80	1.41	0.72	31.18	30.28	1.63	0.90	28.02	27.47	1.20	0.55
	SAT	29.44	28.80	1.35	0.63	31.18	30.28	1.48	0.90	27.87	27.47	1.22	0.40

Table 4.2: Temperature comparison for SAT and DEF cases. A denotes average daily, D denotes daytime average, and N denotes nighttime average.

Station	Case	Simulated mean (A)	Observed mean (A)	RMSE (A)	Bias (A)	Simulated mean (D)	Observed mean (D)	RMSE (D)	Bias (D)	Simulated mean (N)	Observed mean (N)	RMSE (N)	Bias (N)
KMO	**DEF**	5.86	2.65	3.73	3.31	6.12	2.26	4.17	3.87	4.73	2.21	2.87	2.52
	SAT	5.42	2.65	3.51	2.87	5.94	2.26	4.06	3.69	2.92	2.21	1.62	0.71
TPR	**DEF**	5.66	2.98	3.22	2.69	6.61	3.55	3.55	3.06	4.17	2.08	2.61	2.1
	SAT	4	2.98	1.82	1.02	4.9	3.55	2.04	1.36	2.56	2.08	1.4	0.49

Table 4.3: Wind speed comparison for SAT and DEF cases. A denotes average daily, D denotes daytime average, and N denotes nighttime average.

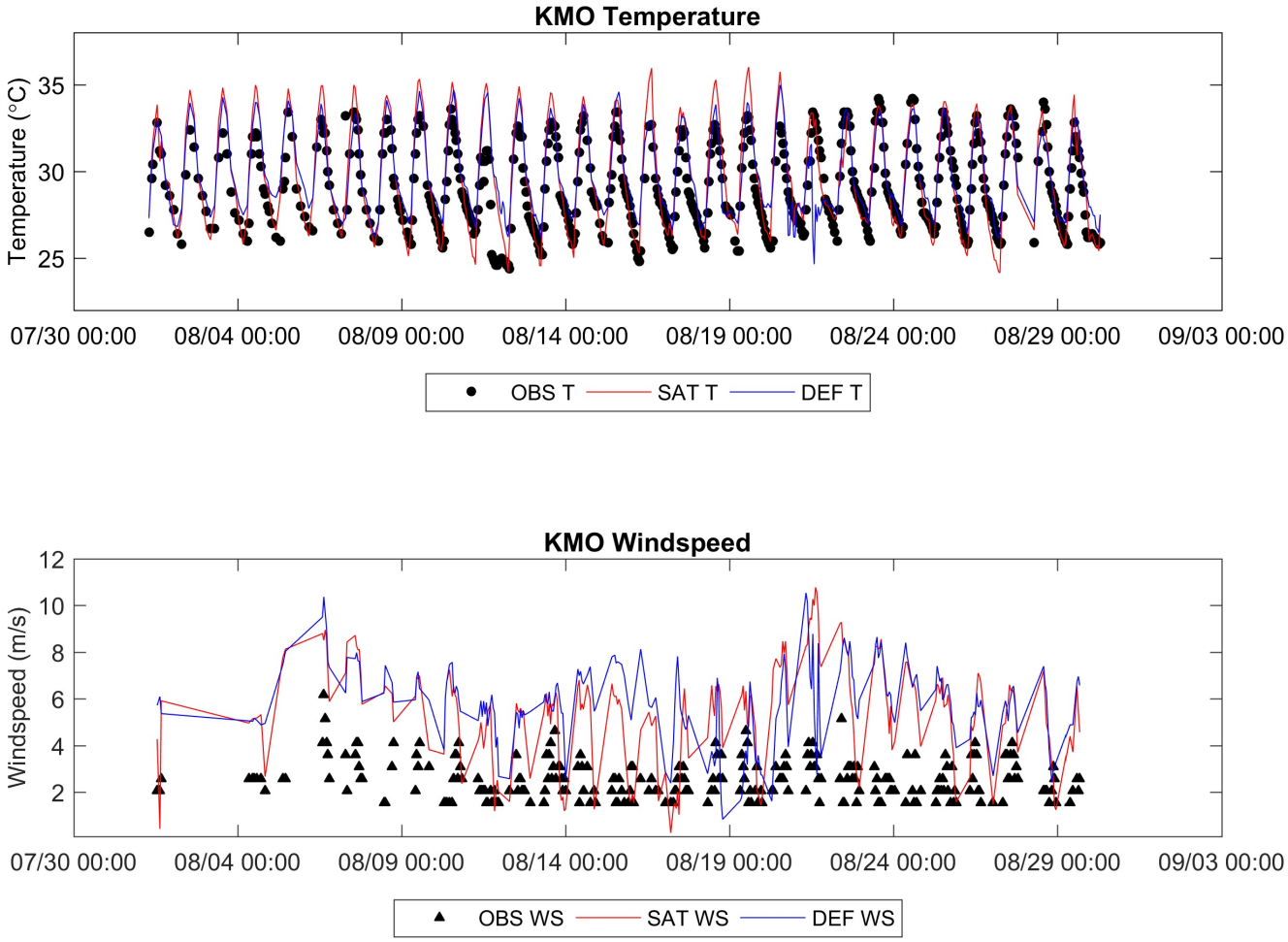

Figure 4.5: Month trend of hourly near-surface temperature and 10-m wind speed at KMO station. Time shown is LST (UTC+7) for August 2014.

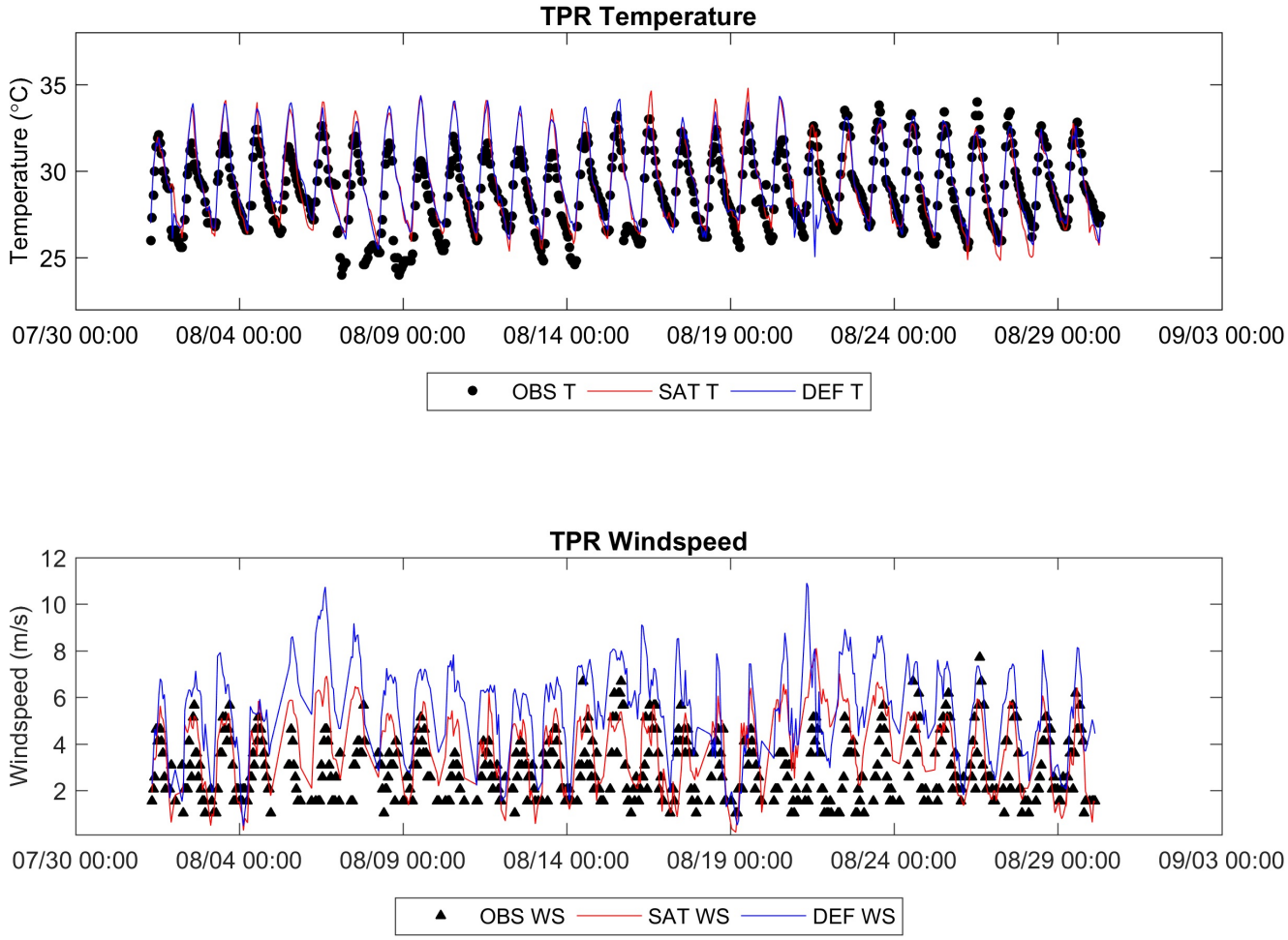

Figure 4.6: Month trend of hourly near-surface temperature and 10-m wind speed at TPR station. Time shown is LST (UTC+7) for August 2014.

Figure 4.8 and 4.7 show the spatial distribution of the average 10-m wind field and 2-m temperature for the full month of August, respectively. The SAT case simulated a higher temperature in the city center (near KMO) during daytime and after sunset than the DEF case. As shown in Figure 4.7 and 4.8, the areas with high temperature and low wind speed in SAT correspond to densely built-up areas, with high $\mathbf{d}$ and $\mathbf{z_0}$ values. The densely built up area generates greater surface wind drag, resulting in weak easterly wind and retention of heat in urban areas.

4.4 Summary

Two simulation cases, SAT and DEF, were conducted for Jakarta to evaluate the performance of satellite-derived urban parameters (Chapter 3) in the SLUCM/WRF modified with urban aerodynamic parametrization scheme. Including urban parameters from global datasets in the simulation provided better agreement, especially with regard to wind speed, than did a simulation that used the default parameters provided in the SLUCM/WRF model. Simultaneously, at the time this work was conducted, a simulation was made for Istanbul (Yucel et al., 2016) to compare the urban parameters derived from global datasets with those from a realistic building morphology. The results can be summarized as follows: (1) SAT improved representation of wind speed and thereby improving temperature, especially improvement in nighttime wind speed over the urban area; (2) Lower wind speed in the high-density built-up area in central Jakarta as a result of the higher surface drag due to the complex urban morphology. Slower wind speeds indicate weakened sea breeze penetration in daytime and land breeze penetration in nighttime. This causes more heat to be trapped in urban areas causing UHI, especially during nighttime.

Furthermore, SLUCM/WRF simulation using urban parameters derived

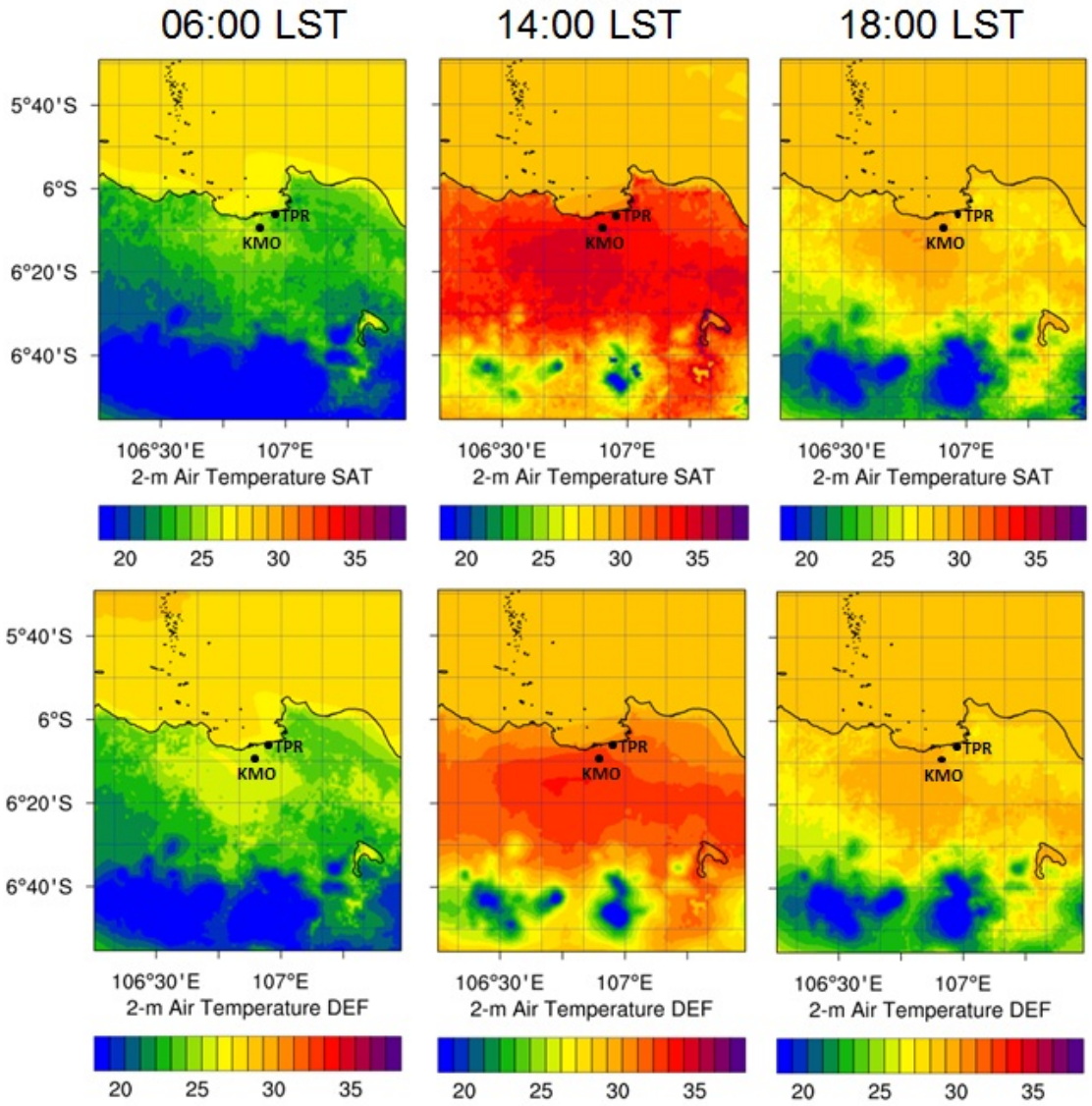

Figure 4.7: August daily average of 2-m temperature in the SAT (above) and DEF (bottom)

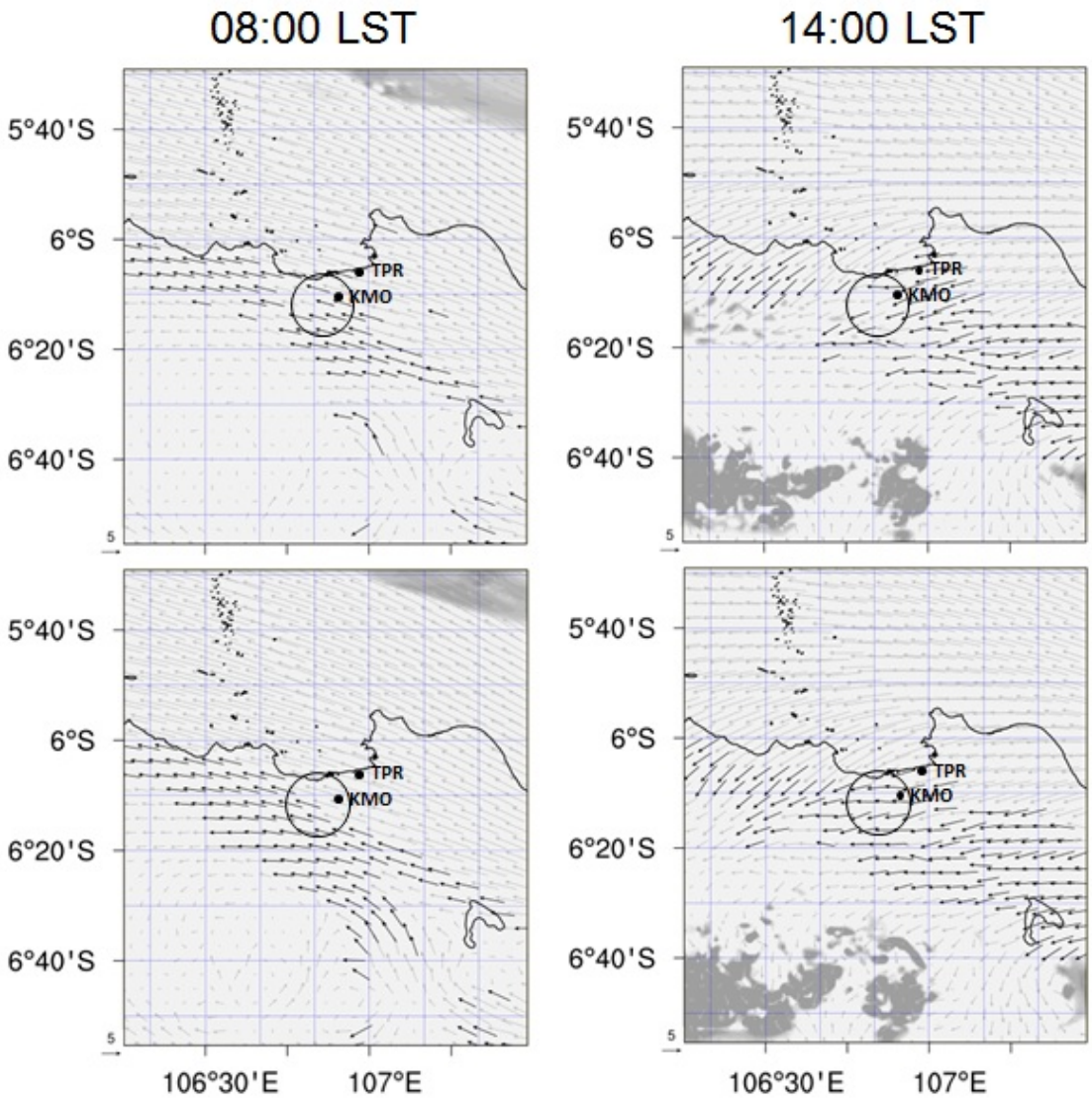

Figure 4.8: The 10-m wind speed in the SAT (above) and DEF (bottom) simulations for August 25, 2014. The darker wind vector shows wind speed > 5 m/s, and the grey shade shows the total water vapor column (g/kg)

from a real 3D building database in Istanbul (Yucel et al., 2016) was not significantly different from a simulation based on urban parameters from global datasets. Therefore, distributed satellite-derived urban parameters, which can also be frequently updated, can serve as a good substitute for actual urban parameters calculated by actual 3D building database in the estimation of urban parameters. As mentioned previously in Chapter 3, this simulation gives evidence of simple and zero-cost solution in conducting mesoscale urban climate analysis in developing cities that mostly lack of actual building database, such as Asian megacities. However, there is some limitation due to the resolution of satellite imageries especially on estimation of average building height, hence affecting on underestimation of aerodynamic roughness parameters. Higher resolution stereo satellite imageries (e.g. up to 2m) can be one of the solution to improve the average building height value estimation to be close to real value. However, this effort have cost trade-off in the application.

Regarding the systematical bias of temperature, we understand that improvement of temperature representation is important in urban climate study and this is an important issue for future research faced not only by our team but throughout the WRF user community. Improvement on urban fabric thermal properties in study area along with detailed urban land use for geographical simulation boundary (Brousse et al., 2016) and utilization of multi-layer urban canopy model (Salamanca et al., 2010) may serve as a promising way in solving the problem, despite higher computational resources. Furthermore, recent study by Demuzere et al. (2017) emphasized that land surface model that are developed until now are not sufficient yet for tropical area which have high humidity.

5

Present urban climate reconstruction

5.1 Introduction

Future climate change is expected to increase the vulnerability of urban populations to associated risks, which are further exacerbated in low- and middle-income countries (Revi et al., 2014). Moreover, urban agglomerations have local effects on the atmosphere (Arnfield, 2003; Masson, 2000; Oke et al., 2017) that could intensify the effects of global climate change. For example, from 1961 to 2010, the mean annual temperatures in 39 major cities increased at rates of 0.12–0.45°C per decade (Rosenzweig et al., 2015). Meanwhile, urban areas have been projected to be warmer than surrounding rural areas (Kalnay and Cai, 2003) and are projected to experience more tropical nights in the future (McCarthy et al., 2010; Oleson, 2012) under climate change. Such urban effects will have a significant impact on energy consumption for cooling (Martilli, 2014), heat waves (Ander-

son et al., 2018; Lemonsu et al., 2015; Wouters et al., 2017; Zhao et al., 2018) , sea breeze penetration (Varquez et al., 2015), and urban extreme rainfall (Niyogi et al., 2017).

The urban agglomeration of Greater Jakarta is currently ranked as the second largest megacity, with a population of more than 30 million (Demographia, 2018). The agglomeration includes Jakarta and other surrounding cities (Figure 5.2). Located in the equatorial region of Southeast Asia, Greater Jakarta experiences an equatorial monsoon (Am) climate under the Köppen–Geiger climate classification (Rubel and Kottek, 2010), characterized by high annual temperatures under the Asian monsoon system that drive the wet season (October–March) and dry season (April–September). Greater Jakarta is a topographically diverse city with coastal areas to the north adjacent to mountainous areas to the south. As such, sea (land) breeze and katabatic (anabatic) wind dominate Greater Jakarta's boundary layer wind system. Greater Jakarta has experienced rapid urbanization since the 1980s, and its urbanization growth trend resemblances that of upper-middle-income countries (United Nations, 2015). Greater Jakarta is expected to grow rapidly for another 30 years before reaching its projected peak population growth. Therefore, we set the 2046-2055 as the target in this study to offer insights for planning optimal mid-term urban mitigation and adaptation strategies.

Before moving to future urban climate simulations, historical simulations for during period 2006-2015 was conducted to represent present climate condition. The present climate condition is fundamental reference of any change in future climate. The framework of present and future urban climate simulations in Greater Jakarta is as described in Figure 5.1. This chapter is aimed to explain the simulations conducted for present climate condition (i.e., the red box in Figure 5.1). Historical simulations for long period (i.e., 10 years) also aims to assess the model performance in the longer run.

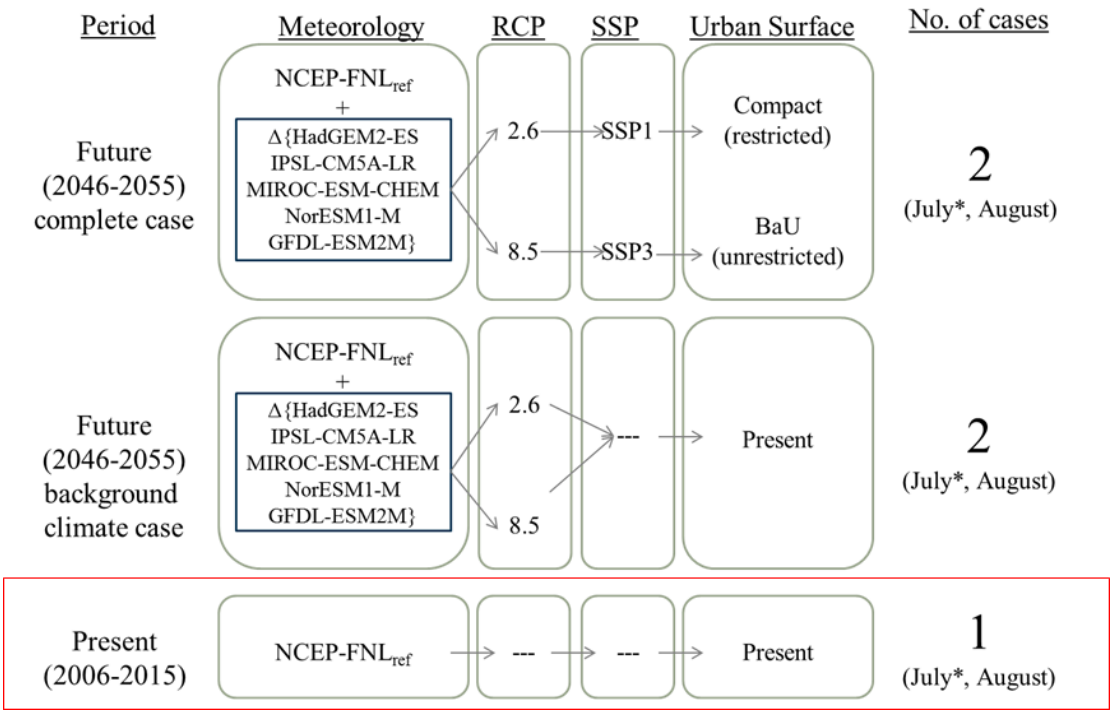

Figure 5.1: Framework and case description of the detailed present and future simulation runs. (*) marks define the spin-up month (25 days on July each year).

5.2 Simulation settings

The designated simulation days for the simulation of Jakarta included the whole month of August 2006–2015 for the present and later in Chapter 6, 2046–2055 for the future, with 25 spin-up days for every year. August represents the peak of the dry season under the weak and low-moisture-content Australian monsoon, which is critical for heat stress and drought. In addition, the lowest synoptic effect on Greater Jakarta is observed in August, which is suitable for studying local urban effects. All cases had the same domain spatial boundaries, with one parent and two nested domains (Figure 5.2). The WRF/SLUCM setting configuration (i.e., environment, microphysics, lateral boundary conditions) used for historical simulations is the same with August validation setting mentioned in Chapter 4 section 4.2 for SAT case.

The National Centers for Environmental Prediction Final (NCEP-FNL) global weather data archive with a 6-h temporal resolution and 1° x 1° spatial resolution was used for the lateral and initial meteorological boundary conditions. In addition, 4-km MODIS monthly daytime and nighttime sea surface temperature data were used to improve default model values. An updated version of the MODIS 20-class land-use was used (see section 3.2.1). All cases used the following physical settings: shortwave radiation scheme by Dudia; RRTM longwave radiation scheme; Microphysics New Thompson; Kain-Fritsch cumulus parametrization; and planetary boundary layer Mellor-Yamada Level 2.5. Differ with Chapter 4, all cases not only used distributed urban parameters (i.e., as explained in Chapter 3), but also distributed hourly anthropogenic heat emissions (AHE) at a 1km resolution (Dong et al., 2017), which were interpolated to the simulation grid.

Three synoptic observation stations for near-surface temperature and wind speed with a 3-h temporal resolution were used to validate the model: Kemayoran

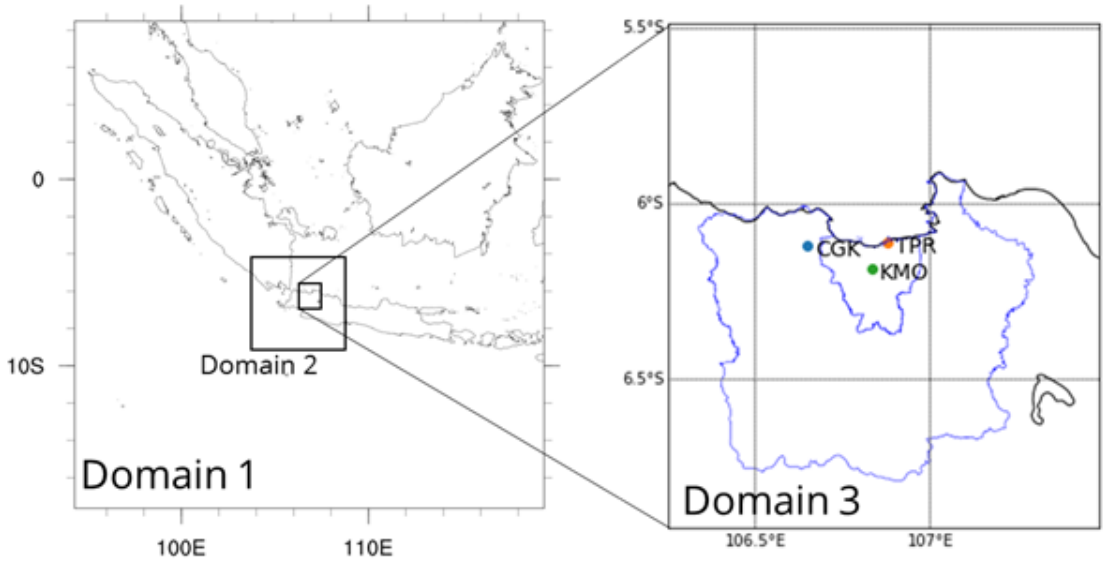

Figure 5.2: Modified WRF/SLUCM domain configuration for Greater Jakarta. The inner solid blue line represents the administrative boundary of Jakarta, while the outer line represents Greater Jakarta, including the three surrounding cities (Bekasi, Tangerang, and Bogor).

station (KMO; 106.8418E, 6.1556S); Tanjung Priok station (TPR; 106.8778E, 6.111S); and Cengkareng (CGK; 106.65E, 6.1167S) (Figure 5.2). All data were downloaded from https://www.ogimet.com. All stations were classified as urban stations and followed the World Meteorological Organization flat grassland station standard. KMO was located in a commercial/industrial area in our classification, while TPR was located in a high-density urban area. For the local climate zone (LCZ) classification, KMO was located in a compact high-rise area (LCZ 1), while TPR was located in a compact mid-rise area (LCZ 2) and CGK was located in grassland on the perimeter of Soekarno–Hatta International Airport. Location of each station is as illustrated in Figure 5.3a to 5.3c.

5.3 Results and Discussions

The model predicted the nighttime temperature well, with root mean square error (RMSE) values of 1.03, 1.14, and 1.45 for TPR, KMO, and CGK, respectively.

Figure 5.3a: Locations and images of the areas surrounding the KMO station

Figure 5.3b: Locations and images of the areas surrounding the TPR station

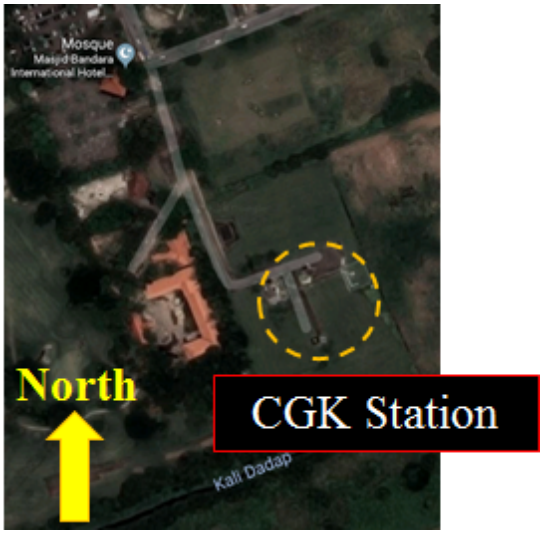

Figure 5.3c: Locations and images of the areas surrounding the CGK station

However, the model generally overestimated the daytime near-surface temperature, with RMSE values of 1.45, 1.98, and 1.79 for TPR, KMO, and CGK, respectively. It also resulted in a smaller bias for nighttime temperature (TPR: 0.37°C, KMO: 0.34°C, CGK: 0.41°C) than daytime temperature (TPR: 0.70°C, KMO: 1.47°C, CGK: 1.22°C). Table 5.1a, 5.1b, 5.2a, and 5.2b present the detailed statistical validation of temperature and wind.

The results showed that the model offered better performance during nighttime than daytime in the study area, as represented in Figure 5.4 for TPR. This results show month-to-month similar pattern with the result of Chapter 4. Hypotheses on technical causes of bias have been discussed in section 4.3. Alike to what already mentioned in section 4.3, the observation points were surrounded by high buildings, causing low ambient temperature measurements due to shading and low wind speed caused by building wakes. Moreover, the points were located on grassland, which is associated with evaporative heat transfer and induces a cooling effect. Finally, since the model had a 1-km resolution, these observation points may not have sufficiently represented spatial trends. Even though there is

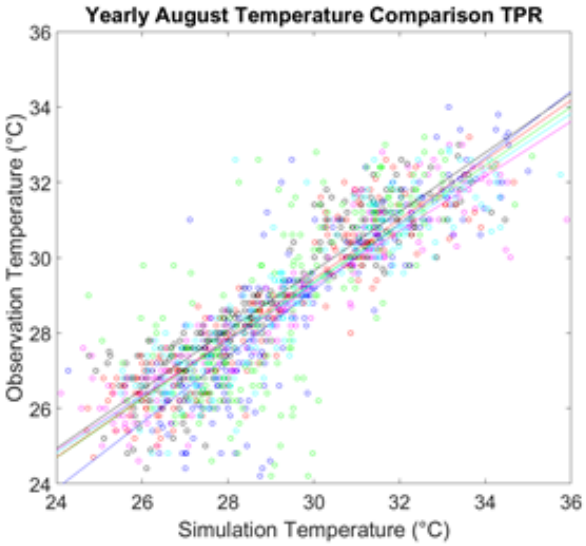

Figure 5.4: Simulation and observation comparison for August 2006-2015 in TPR station

spatial incompatibility between model results and observation values, the average differences in temperature and wind speed are deemed low for such study (Cox et al., 1998) of $< 2°C$ for temperature and $< 2.5m/s$ for 10-m wind. Therefore, simulations for future 2046-2055 period will use the same model settings with the present ones.

5.4 Summary

This chapter talks about the reconstruction of historical climate in 2006-2015. This period is then regarded as the present climate condition that function as reference period of 2010s. The simulation biases have same behavior as discussed in Chapter 4. The hypotheses is due to systematical error mostly regarding to unmatched urban energy balance which largely impact on turbulent fluxes, hence affecting temperature and wind speed. The inclusion of distributed urban roughness parameter through aerodynamic parametrization into the SLUCM increase the accuracy of urban turbulent and mostly affecting wind speed accuracy. Im-

provement on urban surface model is very much worthwhile although currently it is out of scope of this study. For further analysis that needs higher accuracy with observation value and absolute value (i.e. despite difference value) such as Chapter 7, bias adjustment will be conducted offline the simulation.

Station (Average 10-year)	Simulated mean (A)	Observed mean (A)	RMSE (A)	Bias (A)	Simulated mean (D)	Observed mean (D)	RMSE (D)	Bias (D)	Simulated mean (N)	Observed mean (N)	RMSE (N)	Bias (N)
TPR	29.26	28.76	1.27	0.54	30.61	29.9	1.45	0.7	27.88	27.57	1.03	0.37
KMO	29.78	28.87	1.63	0.91	31.55	30.06	1.98	1.47	27.99	27.65	1.14	0.34
CGK	28.39	27.58	1.63	0.82	30.38	29.17	1.79	1.22	26.37	25.95	1.45	0.41

Table 5.1a: Near surface temperature (i.e., diagnostic 2-m temperature on screen layer of urban canopy layer) statistical data validation, averaged for10-year (2006-2015) for each station

Station (Average 10-year)	Simulated mean (A)	Observed mean (A)	RMSE (A)	Bias (A)	Simulated mean (D)	Observed mean (D)	RMSE (D)	Bias (D)	Simulated mean (N)	Observed mean (N)	RMSE (N)	Bias (N)
TPR	3.58	3.02	2.47	1.08	4.54	3.36	2.27	1.48	2.59	2.62	2.72	0.33
KMO	3.86	2.87	3.77	2.03	4.96	2.96	3.66	2.45	2.75	2.59	3.39	0.91
CGK	4.19	3.18	2.45	1.21	5.73	3.96	2.91	1.89	2.62	2.26	1.73	0.42

Table 5.1b: 10m wind speed statistical data validation, averaged for10-year (2006-2015) for each station

Station and Year	Simulated mean (A)	Observed mean (A)	RMSE (A)	Bias (A)	Simulated mean (D)	Observed mean (D)	RMSE (D)	Bias (D)	Simulated mean (N)	Observed mean (N)	RMSE (N)	Bias (N)
TPR 2006	28.96	28.66	1.08	0.6	30.42	29.75	1.29	0.74	27.47	27.43	0.77	0.45
TPR 2007	29.58	28.76	1.66	0.79	31.13	30.12	1.88	0.96	27.99	27.39	1.41	0.61
TPR 2008	29.16	28.45	1.29	0.6	30.53	29.73	1.52	0.66	27.78	27.23	1.03	0.55
TPR 2009	29.32	28.9	1.32	0.41	30.63	29.86	1.66	0.67	27.98	27.87	0.81	0.13
TPR 2010	29.26	28.83	1.56	0.45	30.22	30.09	1.54	0.14	28.27	27.53	1.58	0.77
TPR 2011	28.94	28.68	1.04	0.44	30.3	29.7	1.2	0.72	27.55	27.54	0.82	0.12
TPR 2012	29.37	28.69	1.22	0.7	30.85	29.76	1.48	1.07	27.87	27.58	0.88	0.32
TPR 2013	29.58	28.81	1.5	0.79	30.85	29.97	1.58	0.86	28.29	27.58	1.41	0.73
TPR 2014	29.48	28.99	1.11	0.5	30.87	30.15	1.34	0.72	28.07	27.81	0.81	0.26
TPR 2015	28.91	28.79	0.92	0.14	30.31	29.84	1.05	0.47	27.49	27.69	0.77	-0.2
KMO 2006	29.41	28.51	1.32	0.8	31.26	29.69	1.7	1.45	27.52	27.3	0.73	0.13
KMO 2007	30.05	28.77	1.95	1.26	32	29.94	2.38	2.03	28.06	27.59	1.39	0.5
KMO 2008	29.72	28.89	1.62	0.85	31.49	30.1	2.01	1.46	27.92	27.72	1.11	0.26
KMO 2009	29.87	29.29	1.64	0.65	31.52	30.34	2.07	1.24	28.18	28.17	0.99	0
KMO 2010	29.83	28.84	1.98	0.99	31.22	30	2.2	1.19	28.4	27.64	1.72	0.79
KMO 2011	29.48	29.08	1.18	0.44	31.27	30.21	1.4	1.07	27.66	27.89	0.89	-0.24
KMO 2012	29.9	28.84	1.52	1	31.78	30.18	1.85	1.55	27.98	27.53	1.11	0.47
KMO 2013	30.08	28.76	2.02	1.32	31.81	30.2	2.3	1.61	28.32	27.27	1.69	1.03
KMO 2014	30.02	29.03	1.55	1	31.78	30.31	1.88	1.43	28.24	27.7	1.11	0.56
KMO 2015	29.5	28.64	1.54	0.83	31.36	29.63	2.05	1.72	27.6	27.63	0.71	-0.07
CGK 2006	27.93	26.97	1.59	0.96	30.11	28.59	1.89	1.49	25.71	25.28	1.2	0.4
CGK 2007	28.72	27.64	1.88	1.05	30.89	29.18	2.14	1.64	26.51	26.06	1.58	0.44
CGK 2008	28.28	27.36	1.71	0.96	30.31	29.02	1.94	1.38	26.21	25.69	1.45	0.54
CGK 2009	28.44	27.55	1.65	0.88	30.34	29.15	1.95	1.25	26.5	25.86	1.26	0.48
CGK 2010	28.76	27.68	1.99	1.12	30.3	29.37	1.92	0.92	27.2	25.93	2.07	1.33
CGK 2011	27.97	27.23	1.4	0.75	29.99	28.7	1.56	1.32	25.92	25.74	1.22	0.18
CGK 2012	28.31	27.81	1.54	0.5	30.45	29.41	1.46	1.04	26.12	26.15	1.62	-0.06
CGK 2013	28.87	27.95	1.89	0.93	30.76	29.63	2.12	1.13	26.95	26.22	1.63	0.73
CGK 2014	28.67	27.74	1.59	0.9	30.59	29.25	1.78	1.3	26.71	26.21	1.38	0.51
CGK 2015	28	27.86	1.08	0.15	30.08	29.35	1.11	0.73	25.89	26.33	1.06	-0.45

Table 5.2a: Near surface temperature (i.e., diagnostic 2-m temperature on screen layer of urban canopy layer) statistical data validation, yearly 2006-2015 for each station

Station and Year	Simulated mean (A)	Observed mean (A)	RMSE (A)	Bias (A)	Simulated mean (D)	Observed mean (D)	RMSE (D)	Bias (D)	Simulated mean (N)	Observed mean (N)	RMSE (N)	Bias (N)
TPR 2006	3.4	2.79	5.46	1.84	4.29	2.41	3.15	2.84	2.5	3.64	8.67	-0.44
TPR 2007	4.03	2.89	2.57	1.31	5.04	3.25	2.46	1.81	3	2.45	2.7	0.71
TPR 2008	3.71	3.17	2.64	0.76	4.74	3.86	3.26	0.9	2.65	2.17	1.33	0.56
TPR 2009	3.58	3.06	1.91	1.11	4.51	3.41	2.19	1.42	2.63	2.45	1.28	0.57
TPR 2010	3.56	2.83	1.88	0.95	4.3	3.32	2.12	1.18	2.81	2.21	1.51	0.65
TPR 2011	3.11	2.8	1.26	0.45	4.09	3.4	1.52	0.79	2.12	2.13	0.88	0.07
TPR 2012	3.36	2.88	1.58	0.89	4.24	3.4	1.75	1.12	2.46	2.18	1.3	0.6
TPR 2013	3.64	3.04	1.79	0.96	4.67	3.54	2	1.22	2.58	2.33	1.44	0.58
TPR 2014	3.9	3.51	1.89	1.29	4.96	3.88	2.03	1.49	2.81	2.66	1.52	0.83
TPR 2015	3.47	3.14	1.29	0.66	4.62	3.85	1.5	1.1	2.29	2.33	1	0.14
KMO 2006	3.6	3.09	4.88	1.68	4.51	2.68	2.97	2.46	2.68	4.31	8.26	-0.62
KMO 2007	4.42	2.57	3.65	2.96	5.65	2.69	4.02	3.42	3.17	2.24	2.26	1.65
KMO 2008	4.06	3.11	4.09	2.25	5.38	3.21	4.24	2.29	2.71	2.23	2.24	1.79
KMO 2009	3.81	3.31	5.63	1.57	4.9	3.22	4.21	2.27	2.7	3.54	8.26	-0.25
KMO 2010	3.95	2.65	3.04	1.93	4.73	2.82	3.38	2.18	3.15	2.15	1.72	1.17
KMO 2011	3.23	2.75	2.27	1.63	4.11	2.84	2.44	1.81	2.32	2.44	1.65	1.07
KMO 2012	3.55	2.93	3.57	1.72	4.49	3.16	4.02	1.97	2.58	2.27	1.73	1
KMO 2013	3.96	3.24	5.33	1.8	5.14	2.94	3.39	2.62	2.76	4.15	8.94	-0.68
KMO 2014	4.18	2.87	3.63	2.36	5.45	3.09	4.12	2.75	2.89	2.36	2.11	1.49
KMO 2015	3.61	2.4	2.67	2.09	4.76	2.62	3.08	2.7	2.44	1.97	1.63	0.93
CGK 2006	3.92	3.18	1.8	0.93	5.36	4.09	2.16	1.26	2.46	2.11	1.27	0.55
CGK 2007	4.84	3.12	3.01	1.96	6.44	3.82	3.61	2.8	3.22	2.3	2.08	0.96
CGK 2008	4.26	3.63	3.04	0.94	5.99	4.62	3.12	1.35	2.5	2.18	2.92	0.33
CGK 2009	4.13	2.89	2.72	1.75	5.81	3.39	3.28	2.62	2.42	2.12	1.46	0.41
CGK 2010	4.4	2.49	3.28	2.2	5.52	3.03	3.84	2.91	3.27	1.88	2.49	1.4
CGK 2011	3.63	3.22	1.62	0.5	5.04	4.15	1.96	0.99	2.18	2.23	1.17	-0.02
CGK 2012	3.92	3.58	2.15	0.45	5.29	4.57	2.49	0.81	2.53	2.48	1.69	0.05
CGK 2013	4.28	3.23	2.52	1.25	5.87	3.91	3.14	2.04	2.66	2.43	1.5	0.33
CGK 2014	4.52	3.44	2.29	1.1	6.34	4.23	2.84	2.1	2.67	2.63	1.52	0.06
CGK 2015	3.97	3	2.09	1.06	5.64	3.76	2.68	1.98	2.27	2.21	1.19	0.09

Table 5.2b: 10m wind speed statistical data validation, yearly 2006-2015 for each station

6

Future urban climate projection

6.1 Introduction

Until recently, general circulation models could not capture urban effects due to their coarse spatial and temporal resolutions (Best, 2006). These models either did not include or roughly assumed urbanization in their future projections. However, recent advances in mesoscale climate modeling have enabled the analysis of urban effects under climate change, although most relevant studies have been conducted at city scales (Doan et al., 2016; Hamdi et al., 2014; Lemonsu et al., 2013), with very few focused on a global scale (Fischer et al., 2012; Oleson et al., 2011). The results of these studies have revealed that urban areas are expected to experience greater temperature increases than surrounding rural areas under a given future climate change scenario. However, such studies have been limited to the assumption that future urban land use is static to present conditions. In

reality, urban expansion in developing countries is expected to accelerate in the near future. Therefore, projecting the future urban climate solely based on climate change effects under the assumption of a static urban area is unrealistic.

Application of urban growth controls (Georgescu et al., 2014; Stone et al., 2010) and urban fabric modifications (Georgescu, 2015; de Munck et al., 2018) to weather models has shown that urban adaptation strategies determine the magnitude of urban effects, indicating that sound urban planning is necessary to achieve highly resilient cities. Recent studies have highlighted the behavior of urban effects under climate change and future urban expansion scenarios in cities of American (Li et al., 2016; Tewari et al., 2017), European (Hamdi et al., 2014; Wouters et al., 2017), Asian (Adachi et al., 2012; Yang et al., 2016), and Australian (Argüeso et al., 2015). The results have shown that due to background temperature increases local urban effects cause greater warming than under global future climate scenarios. However, to our knowledge, these studies limited urban expansion to practical urbanization scenarios or two-dimensional urban land-use scenarios with simple parameterizations of urban morphology. By contrast, few advanced studies have coupled future global climate change scenarios and local urbanization based on socio-economic scenarios (Kusaka et al., 2016; Masson et al., 2014). Such studies excel in the projection of future urban morphological parameters and heat emissions based on socio-economic scenarios. Despite these studies representing future urban climates more realistically, they have been restricted to developed countries and their study areas. More recent studies analyzed urban climate by combining global climate change scenario and local urbanization based on issued urban development master plan in developing countries (Doan and Kusaka, 2018; Iizuka, 2018; Lee et al., 2017; Yang et al., 2016). However, it is very challenging to get such urban planning data in global scale.

To address this shortcomings, we developed a future urban climate pro-

jection by integrating global climate change projection based on pseudo global warming method and local urbanization scenario based entirely on globally available datasets. Compared with previous similar studies, our goal is to develop a local urbanization scenario considering building volumes and heat emission derived from global socio-economic scenario. We aversely using any data from local governments or stakeholders to optimize global implementation. The framework was designed to provide a generic, repeatable, and realistic approach to futuristic urban climate studies. We applied the method to project the future urban climate in Greater Jakarta, Indonesia, as a large tropical megacity in Southeast Asia, until the 2046-2055. We integrated Representative Concentration Pathways (RCP; van Vuuren et al., 2011) and urbanization scenario derived from Shared Socioeconomic Pathways (SSP; O'Neill et al., 2014) in mesoscale weather simulations. Accordingly, we were able to analyze the global, urban, and combined global–urban effects. The ultimate goal is that this approach can be applied to other megacities in developing countries.

6.2 Methodology

Two global emission scenarios of RCP, RCP2.6 and RCP8.5 were selected considering the best and worst emission scenario respectively. We paired RCP with SSP to include local urbanization adaptation scenario thus creating an integrated global-urban climate projection analysis. We used SSP1 and SSP3 scenario generated from Integrated Assessment Model of Asia Pacific Integrated Model (AIM) globally available at regional and country scale (Fujimori et al., 2017, 2014, 2012). RCP scenario was used to determine background global climate change effect including physical meteorological parameters and boundaries. SSP scenario was used to project future urban socio-demographic parameters including population density, energy consumption, and gross domestic product (GDP). We used

Case name	Simulation years	Emission forcing	Boundary data	Urban parameters and AHE
Present	2006-2015	-	NCEP-FNL	Present
RCP2.6	2046-2055	RCP2.6	NCEP-FNL-PGW-RCP2.6	Present
RCP8.5	2046-2055	RCP8.5	NCEP-FNL-PGW-RCP8.5	Present
RCP2.6& Compact	2046-2055	RCP2.6	NCEP-FNL-PGW-RCP2.6	Compact city scenario (SSP1)
RCP8.5&BaU	2046-2055	RCP8.5	NCEP-FNL-PGW-RCP8.5	BaU scenario (SSP3)

Table 6.1: Description for numerical simulations for present and future urban climate. Case RCP2.6 and RCP8.5 are background climate cases as illustrated in 5.1.

these parameters as fundamental components in formulating urbanization scenario. Based on scenario matrix concept between RCP and SSP scenario (van Vuuren et al., 2014), we selected RCP2.6 to be coupled with SSP1 and RCP8.5 with SSP3. RCP2.6&SSP1 low emission scenario represents the best adaptation strategy. In contrary, RCP8.5&SSP3 high emission scenario represents worst adaptation strategy.

All simulations (see Figure 5.1) were based on high-resolution 1-km regional climate modeling to simulate the present and future urban climate in Greater Jakarta. Present (2006–2015) and future (2046–2055) climate was simulated using the Weather Research and Forecasting (WRF) model coupled with a modified version of the single-layer urban canopy model (modified SLUCM; Kusaka et al., 2001) to place importance on specific urban morphological parameters (Varquez et al., 2015). These parameters were used to estimate the urban aerodynamic parameters, zero-plane displacement, and roughness length to determine momentum and heat (Hagishima et al., 2009; Zaki et al., 2011; Grimmond and Oke, 2002; Kanda et al., 2013; Kawai et al., 2009; Kanda et al., 2007).

The future global climate scenario was downscaled using a pseudo global warming (PGW) (Kimura and Kitoh, 2007; Rasmussen et al., 2011; Sato et al., 2007) method with ensembles of five CMIP5 global climate models (GCMs) as

inputs for RCP2.6 and RCP8.5. The urban parameters were projected based on the sociodemographic parameters from SSP1 and SSP3. We proposed two urban expansion scenarios, compact and business-as-usual (BaU) adaptation strategies, where the compact scenario was derived from SSP1 and the BaU scenario was derived from SSP3. Then, the global and urbanization scenarios were coupled in the simulation runs.

6.2.1 Future global climate projection

Future climate simulations were conducted using the PGW method under two cases: global climate change alone and combined global–urban climate change (Table 6.1). The PGW method is an indirect future climate dynamical downscaling method derived from GCMs (Kimura and Kitoh, 2007). It represents a delta-change method, taking the difference between present and future perturbations and adding the difference to present historical climate simulations. The PGW method has been used widely in other future project dynamic downscaling studies in a variety of future atmospheric fields to study urban climate (Adachi et al., 2012; Doan and Kusaka, 2018; Iizuka, 2018; Iizuka et al., 2015; Kusaka et al., 2012; Tewari et al., 2017; Yamamoto et al., 2018).

Direct downscaling (DDS) method for future climate projection is conducted as simulations on regional climate model (RCM) nested domains directly within GCM boundaries. DDS method is done annually from present year(s) until future target year(s). However, reproduction of regional climate system is still challenging, since simulated climates in RCM domains are strongly influence by GCM's forcing which is larger than RCM first domain order (Sato et al., 2007). Thus, bias contained in GCM will largely affect RCM and cause domino effect in finer domains. PGW reduce the GCM bias by only use the climate parameters difference resulted by GCM realization (Adachi et al., 2012). Furthermore,

differ to DDS method that require complete set of climatic parameters as input at decided time interval (i.e. 3-hourly or 6-hourly), PGW gives more flexibility to adjust the necessary climatic parameters based on our preferred time interval. Since we used 6-hourly FNL initial and lateral boundary for the simulation, PGW allows us to modify selected parameters in FNL based on delta difference of parameters resulted from PGW and only applied it in preferred time interval. As the result, PGW downscaling could reduce computational time compare with DDS. In addition, it also reduces the sampling error caused by interannual or interdecadal variability because the daily weather in the future climate will have similar characteristic to those corresponding days (present days) in PGW method.

In PGW dynamical downscaling, the difference of climatological paremeters between 10 to 30-year average of future (i.e. we used 10-year averaged for this study) and that of present is calculated using GCM data. Then, the linear coupling of the climatological parameters difference and renalysis data (i.e., present boundary condition from reanalysis data -in our study we used NCEP-FNL - added with the difference) is set to WRF/SLCUM as future initial boundary condition. From here, dynamical downscaling is conducted in WRF/SLUCM system environment. Using this approach, we considered the 10-year average of future climatological parameters of each GCM in August during the period 2046–2055 and for 2006-2015 for present period. Figure 6.1 and Figure 6.2 describe schematic flow of PGW. GCM climatic parameters data are available to download from https://esgf-node.llnl.gov/projects/esgf-llnl/, or http://www.ipcc-data.org/sim/gcm_monthly/AR5/Reference-Archive.html. The resolution of each ensemble member is as presented in Table 6.2.

The climatological parameters necessary for the PGW method include three-dimensional wind components (3-hourly and 6-hourly), temperature components including 2-m temperature and surface temperature (3-hourly, 6-hourly,

GCM Name	Atmospheric grid resolution (in degree)	
	Lat	Lon
HadGEM2-ES	1.25	1.875
IPSL-CM5A-LR	1.8947	3.75
MIROC-ESM-CHEM	2.7906	2.81
NorESM1-M	1.8947	2.5
GFDL-ESM2M	2.0225	2.5

Table 6.2: GCM member used in this study and their resolution (https://portal.enes.org/data/enes-model-data/cmip5/resolution)

daily, and monthly), pressure components (6-hourly), and humidity components (3-hourly, 6-hourly, and monthly) acquired from each GCM member. Ensemble averaging was done for each climate component difference value from 2046-2055. The ensemble averages were subtracted from the ensemble averages of 2006-2015 climate components. The difference of the ensembles was added to the meteorological boundaries of the historical NCEP-FNL to be used as the meteorological boundary for 2046-2055. Target climatic parameters following WRF/SLUCM notations are:

- 4-dimensional temperature (TT) modified by difference of 2-m temperature,
- 4-dimensional U wind component (UU) modified by difference of U wind velocity component,
- 4-dimensional V wind component (VV) modified by difference of V wind velocity component,
- 4-dimensional relative humidity (RH) modified by difference of relative humidity,
- 4-dimensional geopotential height (GHT) modified by difference of pressure,

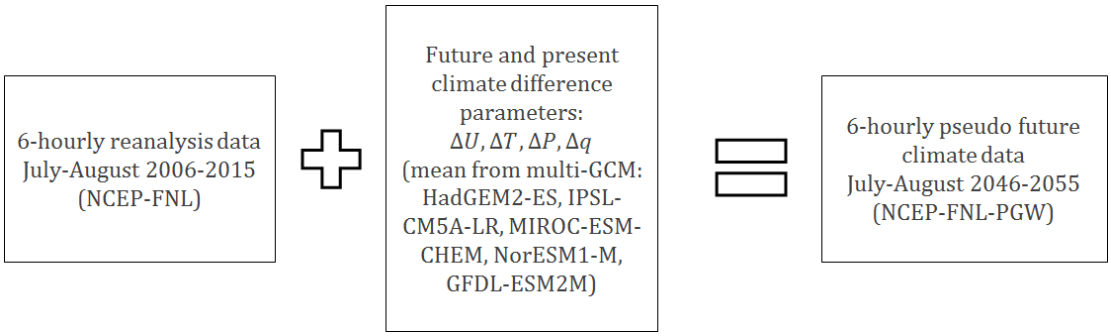

Figure 6.1: Conceptual framework of future meteorological boundary based on PGW method

- 4-dimensional soil layer temperature (ST) modified by difference of surface temperature,
- 3-dimensional skin temperature (SKT) modified by difference of surface temperature,
- 3-dimensional sea surface temperature (SST) modified by difference of surface temperature,
- 3-dimensional soil temperature (SOILT; STxxxxxx, x denotes soil layer code) modified by difference of surface temperature.

Further details of the PGW method can be found in Kimura and Kitoh (2007). In this study, we used NCL programming language to process PGW input as described in Appendix C.

6.2.2 Future local urbanization scenario projection

In a rapidly urbanizing megacity such as Greater Jakarta, it is insufficient to consider only future background climate changes to analyze future urban climate, since urban sprawl is expected to expand widely over the next 30 years. Therefore, we incorporated urbanization scenarios into the future projections based on a socio-economic scenario that supports the RCPs, the Shared Socio-economic Pathways

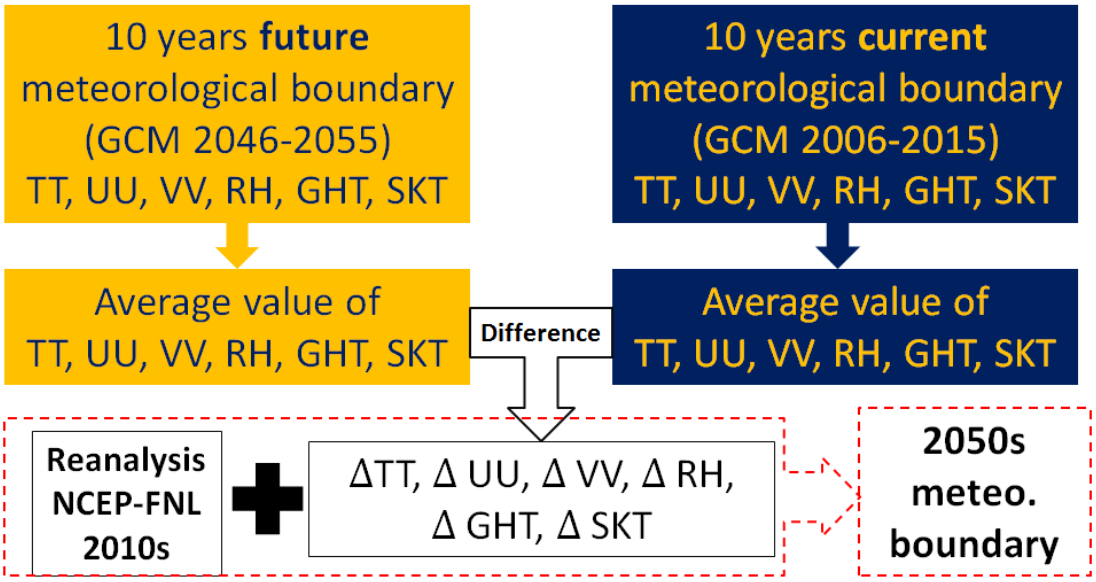

Figure 6.2: PGW method workflow presented in current study

(SSPs). As such, we not only conducted a future projection based on background climate change downscaled using the PGW model but also cases involving both the PGW model and urbanization scenarios.

We considered future urbanization scenarios under the worst and best urban adaptation strategies. The worst adaptation strategy was represented by SSP3, defined by high emissions, inefficient energy consumption, and low-resilience urban planning. We assumed that this condition would force people to reside in suburban areas, creating horizontal expansion further from the city center. The low adaptation and mitigation strategy under SSP3 consequently led to unrestricted future urban expansion. To support this, we created the BaU urbanization scenario from historical urban sprawl trends in Jakarta without any restrictions on horizontal expansion. We considered RCP8.5 as an appropriate emission scenario for the BaU scenario (henceforth, RCP8.5&BaU). Conversely, SSP1 represented the best mitigation strategy, defined by low emissions, high energy efficiency, and high resilience. This condition better supported population growth centralized

in the city center, and urban expansion was expected to be more vertical than horizontal. Thus, horizontal urban expansion was restrained while vertical expansion was allowed, resulting in a compact city scenario. We considered RCP2.6 as an appropriate emission scenario to support the compact scenario (henceforth, RCP2.6&Compact). Both urbanization scenarios were constructed in a 1km grid resolution.

The urbanization scenarios were developed in two steps: (1) determination of urban sprawl probability and population projection and (2) urban parameters and AHE projection. In the first step, we projected the future sprawl probability of the target area using the cellular automaton model SLEUTH (Clarke et al., 1997; Silva and Clarke, 2002). The model predicts the probability on a 0–100 scale for each grid, where higher values on the scale define higher probabilities of expansion. We used historical land-use data constructed from Landsat for the model's learning step and calculated the BaU scenario from the learning results. Meanwhile, we limited the model's expansion parameters for the compact scenario calculations. Then, we projected the gridded population density using the logistic function, which was modified with the probability parameter defined previously. The projected population densities from SSP1 and SSP3 were used as the future function boundaries. The historical population density was taken from the 1km gridded population data of LandScan (Dobson et al., 2000). For further details see 6.2.2.1.

In the second step, we projected the future urban parameters and AHE changes. We used an empirical model that correlates sociodemographic indicators with urban parameters and AHE (Kawano, 2018; Kawano et al., 2016; Varquez et al., 2017, 2018). Here, we used a nighttime light-adjusted population density (Dong et al., 2017) using Version 1 Nighttime VIIRS Day/Night Band Composites (Elvidge et al., 2013) to adjust the projected population density. The required fu-

ture sociodemographic parameters were referred to SSP3 for the BaU scenario and SSP1 for the compact scenario. The performance of these empirically derived parameters in the modified WRF/SLUCM for the present urban climate was verified (Varquez et al., 2017). Figure 6.3 illustrates the changes in urban parameters and AHE between the present and future for both the compact and BaU scenarios. For further details see 6.2.2.2 and 6.2.2.3.

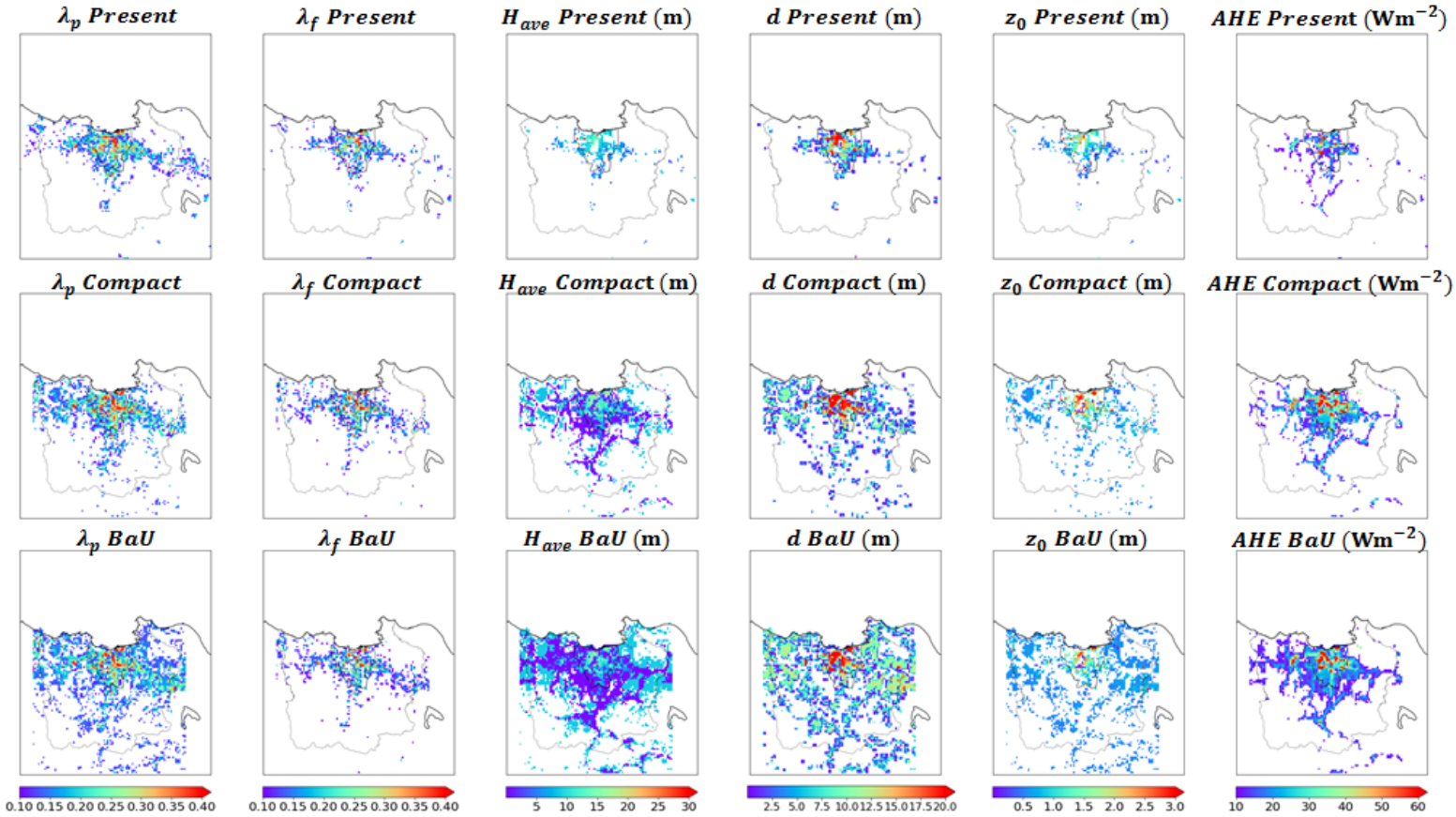

Figure 6.3: Changes in urban morphological, aerodynamic, and AHE parameters between the present and future compact and BaU scenarios in 1km grid resolution. AHE changed temporally on an hourly basis, and the AHE is shown for 13:00 local time.

6.2.2.1 Future population projection

We used the cellular automaton urban growth model SLEUTH (i.e., Slope, Land use, Exclusion, Urban extent, Transportation, and Hill shade) (Clarke et al., 1997) to project the future urban sprawl probability at a 1km grid resolution. The SLEUTH model has been used to project future urban sprawl in several metropolitan areas (Bihamta et al., 2015; Clarke et al., 1997; Jantz et al., 2010; Sakieh and Salmanmahiny, 2016; Silva and Clarke, 2002). The slope and hill shade layers were taken from the GMTED 2010 mean values. Meanwhile, the land-use, exclusion, and urban extent layers were processed from Landsat images from the years 1989, 1994, 2001, and 2014, which were classified using a spectral angle mapping land-use classification algorithm. The exclusion area included water areas, airports, urban parks, and national parks. Finally, the road network layer was taken from an open-source map from 2001 and a digitized map from 1992.

Five coefficients were considered to determine the course of urban sprawl in the study area:

1. The diffusion or dispersion coefficient controls a single grid/pixel number of times being possible as urbanized grid.

2. The breed coefficient determines the probability of a new detached grid becoming new spreading center.

3. The spread coefficient determines the probability that any grid that is part of a spreading center will generate additional urban grid in its surrounding grids.

4. The slope coefficient determines the effect of terrain on as urbanization obstacle (i.e., lower slope will have higher possibility to be urbanized compare with higher slope).

5. The road gravity coefficient determines the distance along the road to which urbanization can occur.

To define the urban growth characteristics of the study area, we conducted calibration calculations to define these coefficients. We used historical land-use data processed from Landsat satellite images from 1989, 1994, 2001, and 2014 as the model learning inputs. Here, the urban growth rules were defined as spontaneous growth, new spreading center growth, edge growth, and road-influenced growth. SLEUTH automatically calculated the growth rules to clarify the study area urban growth characteristics during the calibration process. Additional details of the calibration process can be found in the literature of Clarke et al. (1997) and Silva and Clarke (2002). Based on the calibration process, the growth coefficient results for Jakarta were as follows: diffusion coefficient = 1; breed coefficient = 14; spread coefficient = 89; slope coefficient = 65; and road gravity coefficient = 28. These coefficients were used to define the historical or BaU growth. For controlled, compact urban growth, we modified the spread coefficient to a value of 22, assuming that the spread would be limited to one quarter of that under BaU growth. The results of the urban growth/sprawling probability were then used in a logistic model for the population projection.

Logistic growth models are commonly used in population projections, including those of human populations. The major characteristic of logistic equations is that they implement a population capacity limit. Thus, upon reaching the carrying capacity, the population growth becomes saturated. The discrete logistic

equation used in this study is presented below.

$$\begin{aligned} Pop_{i,j}^{t+1} &= \frac{(A_{i,j}^{t}+1)Pop_{i,j}^{t}}{1+B_{i,j}^{t}\times Pop_{i,j}^{t}} \\ A_{i,j}^{t} &= \exp(r_{i,j}^{t})-1 \\ B_{i,j}^{t} &= \frac{A_{i,j}^{t}}{K^{t}} \end{aligned} \tag{6.1}$$

with

$$r_{i,j}^{t} = \begin{cases} a^{t}\times Pro_{i,j}^{t+1} & \text{for } 0 < Pop_{i,j}^{t} < 100 \\ b^{t}\times Pro_{i,j}^{t+1} & \text{for } Pop_{i,j}^{t} \geq 100 \end{cases}$$

where Pop refers to gridded population, Pro refers to gridded sprawl probability from SLEUTH result, r refers to intrinsic rate of increase, K refers to carrying capacity, and a, b refer to independent estimation variables for rate of increase, changing with time.

Using Equation 6.1, we determined the present rate of population increase based on LandScan 1km gridded population year-by-year data (2001 to 2002, 2006 to 2007, 2009 to 2010, 2010 to 2011, and 2012 to 2013; in order of the base year to the target year) as references for the historical calculation to determine the logistic model parameters. Then, the defined equation was used as the predictor equation for future years. We divided future years into four periods of estimation (2014–2020, 2020–2030, 2030–2040, and 2040–2050) to minimize the prediction deviation, where the target year was the 2050 population.

To define the values of $a^{t},\ b^{t},\ K^{t}$, we optimized the $a^{t},\ b^{t},\ K^{t}$ coefficients by minimizing the sigma value (Equation 6.2) between the predicted population and LandScan population. Then, we determined the most suitable $a^{t},\ b^{t},\ K^{t}$ values for each grid during all four future periods. The city-scale-based population was based on the ratio of the city population to country population (city/country

ratio) taken from the historical city to country ratio from LandScan. For the rate of increase, we used two conditions based on a population limit of 100, which stated that if a given grid exceeded a population of 100, the rate decreased.

We add another restriction based on SSP1 and SSP3 projected population. Yearly SSP city scale value was estimated by using empirical equation derived from linear regression of previous years (2001 - 2013) city/country ratio taken from LandScan. Later, we defined city scale SSP for every year from 2014-2050 value as SSP^t, applied for both SSP1 or SSP3. The constraint is as defined in Equation 6.3. Results of calculation projection using both condition of a^t, b^t, K^t tcoefficient optimization and SSP constraints is shown in Figure 6.4. For each future period, a^t, b^t, K^t coefficient value is as show in Table 6.3.

$$\sigma^{t+1} = \sqrt{\frac{1}{n_i \times n_j} \sum_{i=1}^{i=n_i} \sum_{j=1}^{j=n_j} (LsPop_{i,j}^{t+1} - Pop_{i,j}^{t+1})^2} \tag{6.2}$$

where,

$LsPop_{i,j}$	is LandScan population at grid i,j
$Pop_{i,j}$	is estimated population from logistic equation at grid i,j
σ	is standard deviation of total gridded population from $LsPop_{i,j}^{t+1}$ and $Pop_{i,j}^{t+1}$
n_i , n_j	are total columns number, total rows number

with condition, σ as small as possible.

$$|SSP^t - \text{Total } Pop_{i,j}^t| \leq 10^3 (t = 2020,\ 2030,\ 2040,\ 2050) \tag{6.3}$$

SSP^t is city based population projection based on SSP scenario. Value was processed using linear regression function to projected years (yearly) for city/country ratio of population from SSP. $\text{Total } Pop_{i,j}^t$ is city scale (all grids inside city boundary) estimated population from logistic equation. 10^3 was chosen as the iteration

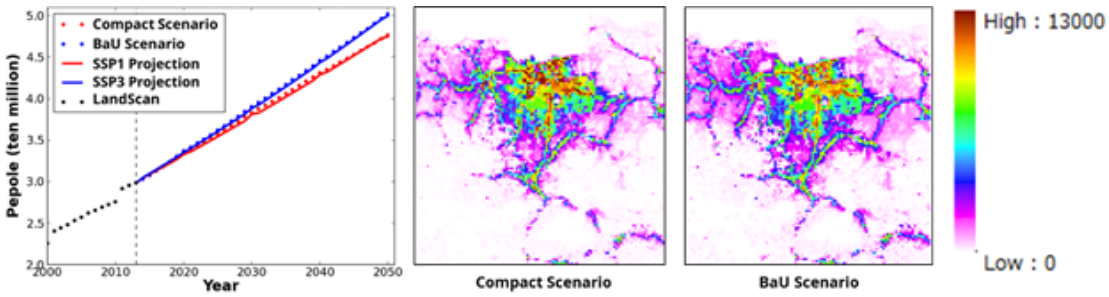

Figure 6.4: Results of the calculated population projection using the conditions of the a^t, b^t, K^t coefficient optimization and SSP constraints for the compact scenario using SSP1 and the BaU scenario using SSP3.

Year (t)	Compact Scenario			BaU Scenario		
	K^t	a^t	b^t	K^t	a^t	b^t
2014∼2020	60000	0.88724	0.035232	60000	1.351278	0.032192
2020∼2030	60000	1.05457	0.025731	60000	1.222823	0.022672
2030∼2040	60000	0.937238	0.020339	60000	0.304	0.019533
2040∼2050	60000	0.862305	0.016753	60000	0.222043	0.01754

Table 6.3: Coefficients for logistic equation

error limit considering that population growth in the SSP scenarios increased by an order of magnitude of 10^7 to 10^8. Thus, 10^3 was considered to represent a small error for the iteration optimization.

6.2.2.2 Future urban parameters projection

Empirical relationship (Kawano, 2018; Varquez et al., 2017, 2018) was built to estimate urban parameters. 30-arc-second (1km) population density (PD) from LandScan 2013 adjusted by nighttime lights (NL) of VIIRS Day/Night Band Composites Version 1 (PDNL) was used. Here, we focused on the estimation of 1km urban parameters of building plan area index (λ_p) and average building height (H_{ave}). The rest of necessary variables (λ_f , d , z_0) later calculated from obtained λ_p and H_{ave} using method describe in Kanda et al. (2013).

To build this relationship function, a complete urban parameter datasets of λ_p and H_{ave} from 5 megacities: New York, Tokyo, Istanbul, Jakarta, and Melbourne were created. A positive linear relationship was found between spatially comparison of PDNL, further normalized by the maximum PDNL ($PDNL_{max}$) and 5 Megacities'realistic H_{ave}. Furthermore, the intercept ($\beta_{H_{ave}}$) and the slope ($\alpha_{H_{ave}}$) of the linear regression used to estimate H_{ave} from PDNL were found to be functions of the city's GDP (in US Dollar) as follows.

$$\begin{aligned} H_{ave} &= alpha_{H_{ave}} \times \frac{PDNL}{PDNL_{max}} + \beta_{H_{ave}} \\ \beta_{H_{ave}} &= -2 \times 10^{-12} \times GDP_{city} + 9.18 \\ \alpha_{H_{ave}} &= -2 \times 10^{11} \times GDP_{city} + 9.80 \\ GDP_{city} &= GDP_{country} \times \frac{Pop_{city}}{Pop_{country}} \end{aligned} \tag{6.4}$$

where $PDNL_{max}$ represents the maximum gridded PDNL value within the area of the city. Population values (Pop_{city}) are taken from projected population value estimated in 6.2.2.1 in 1km grid resolution for 112x135 grids for target study area. Population ($Pop_{country}$) and GDP ($GDP_{country}$) of country in the future were taken from projected country's GDP value (i.e., Indonesia) in 2050 from SSP1 scenario for compact city and SSP3 for BaU (Fujimori et al., 2017, 2012) as defined in Equation 6.5.

$$GDP_{city}(USD) = GDP_{country_{SSP}}(USD) \times \frac{Pop_{city_{SSP}}}{Pop_{country_{SSP}}} \tag{6.5}$$

The empirical equation to estimate future λ_p was also constructed using the same manner with future H_{ave} conceptual manner. Below is the empirical relationship of future λ_p as function of future population as follow.

$$\lambda_p = -0.25 \left(\frac{PDNL}{PDNL_{max}} \right)^2 + 0.46 \left(\frac{PDNL}{PDNL_{max}} \right) + 0.11 \tag{6.6}$$

The urban parameter data for present urban climate calculation were derived from satellite images (Chapter 5). To manage this discrepancy, we calculated both the present and future urban parameters based on sociodemographic empirical equations. Future sociodemographic conditions were taken from the previously calculated population projection, while the other required parameters were taken from the projected SSP1 and SSP3 values. Next, we subtracted the results of the future projected parameters from the present values and added the difference to the present satellite-derived parameters to obtain the future projected parameters. Details on program script for future urban parameters projection, see Appendix A.

6.2.2.3 Future AHE projection

The present anthropogenic heat emission (AHE) values were taken from the 1km gridded global AHE database (Dong et al., 2017). For the future values, we referred to the same publication used as a basis for projecting the AHE. We used SSP1 and SSP3 projected for 2050 instead of currently available country-level energy data (Fujimori et al., 2017, 2012). AHE was calculated as the total energy of heating from energy loss (Q_L), heating from commercial, residential, and transportation sectors (Q_{CRT}), and heating from industrial and agricultural sectors (Q_{IA}) as follows.

$$AHE = Q_L + Q_{CRT} + Q_{IA} \tag{6.7}$$

The gridded Q_L was estimated as follows.

$$Q_L = \frac{EC_p \times R_L}{\sum A_{i,j} \times T} \tag{6.8}$$

where EC_p represents the country-level total annual primary energy consumption

(final and primary) taken from the SSP projection, R_L is the ratio of energy loss to total primary energy consumption $(1-(\mathrm{Energy}_{\mathrm{final}}/\mathrm{Energy}_{\mathrm{primary}}))$, $\sum A_{i,j}$ is the total area of a country in the grid, and T is the time period (one year).

The gridded Q_{CRT} was calculated as follows.

$$Q_{CRT} = \frac{EC_p \times R_{CRT}}{A_{i,j} \times T} \times \left(\frac{PDNL_{i,j}}{\sum PDNL_{i,j}} \right) \tag{6.9}$$

where $A_{i,j}$ corresponds to each area of each grid cell (km^2), $PDNL_{i,j}$ is the population density adjusted to the VIIRS nighttime lights in each grid ($people/km^2$), and $\sum PDNL_{i,j}$ is the sum of the total adjusted population density within each country. Here, we referred to SSP1 and SSP3 future country-level population data. For city-scale data, we used the LandScan 2013 ratios to estimate the population density of each grid.

The gridded Q_{IA} was calculated as follows.

$$Q_{IA} = \frac{EC_p \times R_{IA}}{\sum A'_{i,j} \times T} \tag{6.10}$$

where R_{IA} is the ratio of energy consumed by industry, agricultural, forestry, fishing, and other non-specified sectors to the total primary energy consumption of the country stated in the SSP1 or SSP3 projections, while $\sum A'_{i,j}$ is the total area occupied by industrial and agricultural activities based on SSP1 and SSP3. See Appendix A for programs to calculate future AHE for Jakarta. Finally, the calculated AHE was predicted for the monthly and diurnal variations following previously described methods (Dong et al., 2017).

6.3 Results

6.3.1 Global climate change projection

In the extent of effect solely from global climate change, the results after PGW method showed that the impact is homogenous in our focused domain with $0.60°C$ and $1.37°C$ temperature increased for RCP2.6 and RCP8.5 respectively (Figure 6.5 and 6.7). This homogenous global climate change effect is agreed with similar studies implementing PGW for urban climate analysis (Doan & Kusaka, 2018; Kusaka et al., 2016; Lee et al., 2017; Yang et al., 2016).

Under global effects, humidity increased from the present to the future due to increases in sea temperature. However, urban effects resulted in a drier atmosphere within the urban grids. As a result, humidity in the urban area did not change drastically compared with present conditions, despite the increases in background global humidity. HSU areas exhibited a slightly drier urban atmosphere than AU areas solely from the urban effect.

Considering global effects alone, the RCP2.6 scenario resulted in faster wind speeds throughout the study domain (Figure 6.8). Meanwhile, the RCP8.5 scenario resulted in slower wind speeds, especially around shore areas, probably due to lower sea–land temperature differences.

6.3.2 Future urban climate projection from combined global and local effect

The near-surface temperature in urban land use increased by $0.66 \pm 0.67°C$ and $1.47 \pm 1.38°C$ for RCP2.6&Compact and RCP8.5&BaU, respectively. The large standard deviations indicated a wide heterogeneity in temperature change within each 1km grid. Figures 6.5 and 6.6 present the statistical analysis of the temperature change due to combined global-urban effect and urban effect alone, respec-

tively.

Figure 6.7 shows the spatial distribution of the average temperature change in the future. The average temperature increase in high-sprawl urban (HSU) areas under the RCP2.6&Compact scenario was $0.67 \pm 1.04°C$, while that under the RCP8.5&BaU scenario reached $1.46 \pm 1.50°C$. HSU area was defined by newly or additional projected urban areas due to city volume expansion in 2046-2055. If the UHI were defined pre- and post-urbanization, we could determine the change in temperature from the present to the future in such high-sprawl areas as the temperature change due to the urban effect.

Both the RCP2.6&Compact and RCP8.5&BaU scenarios showed that the average temperature increase in HSU areas was higher in the day than at night (Figure 6.5(d)). By contrast, in the all urban (AU) areas the nighttime temperature increase was higher than that in the daytime. The AU areas were dominated by formerly urbanized areas located within the Jakarta boundary, while HSU areas were characterized by considerably lower building densities and heights, with shallow urban canyons. Moreover, HSU areas resemble residential areas rather than business districts. Thus, the HSU areas may reflect more shortwave radiation to the canopy layer, increasing the temperature during the day but enabling faster cooling at night. Conversely, the AU areas had lower albedos, yielding the opposite effect.

We separated solitary urban effects from the RCP2.6&Compact and RCP8.5 &BaU scenarios by subtracting them with the intermediate case (Figure 6.6). The average urban effects in a compact city for AU and HSU areas were $0.04 \pm 0.65°C$ and $0.05 \pm 1.02°C$ respectively. Meanwhile, the urban effects under the BaU scenario in AU and HSU areas were $0.10 \pm 0.71°C$ and $0.10 \pm 1.05°C$, respectively. The hourly averaged urban effect was less dominant than the background climate change, which ranged from 0.20 to $0.30°C$ (Figure 6.6(b)). Even though the av-

erage contribution was non-significant, the spatial variation was large, ranging from 1.2 to 1.65°C under the compact scenario and 1.2 to 1.80°C under the BaU scenario (Figure 6.6(a)). Comparing the two urbanization scenarios, the urban effect was larger under the BaU scenario. Moreover, the difference was largest from midnight until early morning. Finally, the urban effect resulted in significantly larger temperature variance in HSU areas than in AU areas under both scenarios. The smallest variations were observed immediately after sunrise and at sunset. Compared with AU areas, the daytime urban effect in HSU areas showed higher temperature increases. Meanwhile, the magnitude of the nighttime urban effect was larger in AU areas.

Urban effects could reduce wind speeds by up to 1m/s, as observed in both the compact and BaU scenarios. The urban effects on slower wind speeds were greater under the BaU scenario, especially in the eastern area of Jakarta, corresponding to an area with a high potential for future urbanization. Surface roughness was greater under the BaU scenario than the compact scenario in the city outskirts, leading to higher wind drag and vertical upward wind motion due to convection, resulting in less urban ventilation.

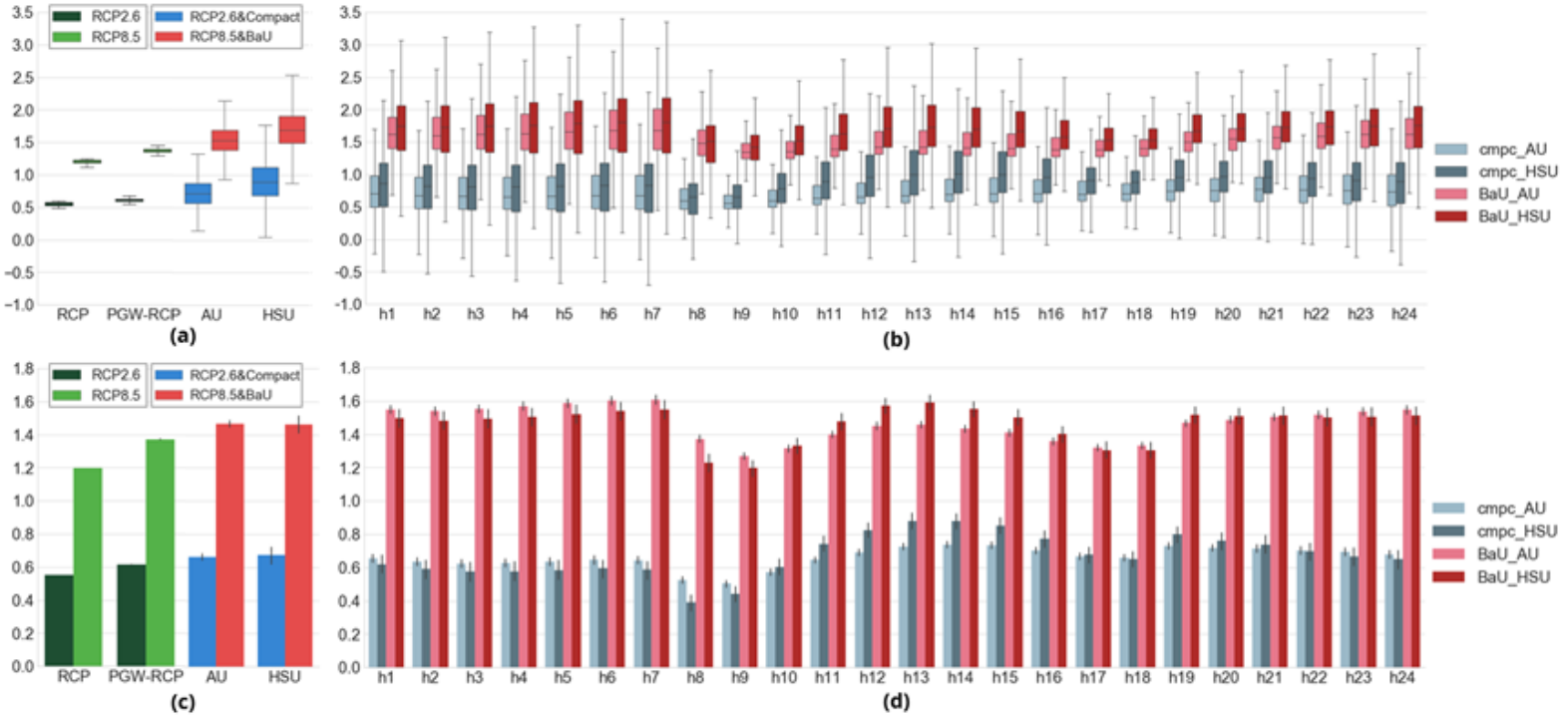

Figure 6.5: Statistical analysis of future temperatures change (vertical axis shows temperature change from present to future in °C; h1, h2, ⋯, h24 define hourly variation): (a) 10-year averaged spatiotemporal temperature change distribution for global climate change effect (RCP2.6 and RCP8.5 bars) and combined with local urbanization effect (RCP2.6&Compact and RCP8.5&BaU bars); (b) hourly variation in (a) for the RCP2.6&Compact (RCP8.5&BaU) scenario in AU and HSU; (c) the same as (a) but accounting for the average, where the error lines show the 95% confidence interval; and (d) hourly variation in (c) for the RCP2.6&Compact (RCP8.5&BaU) scenario in AU and HSU.

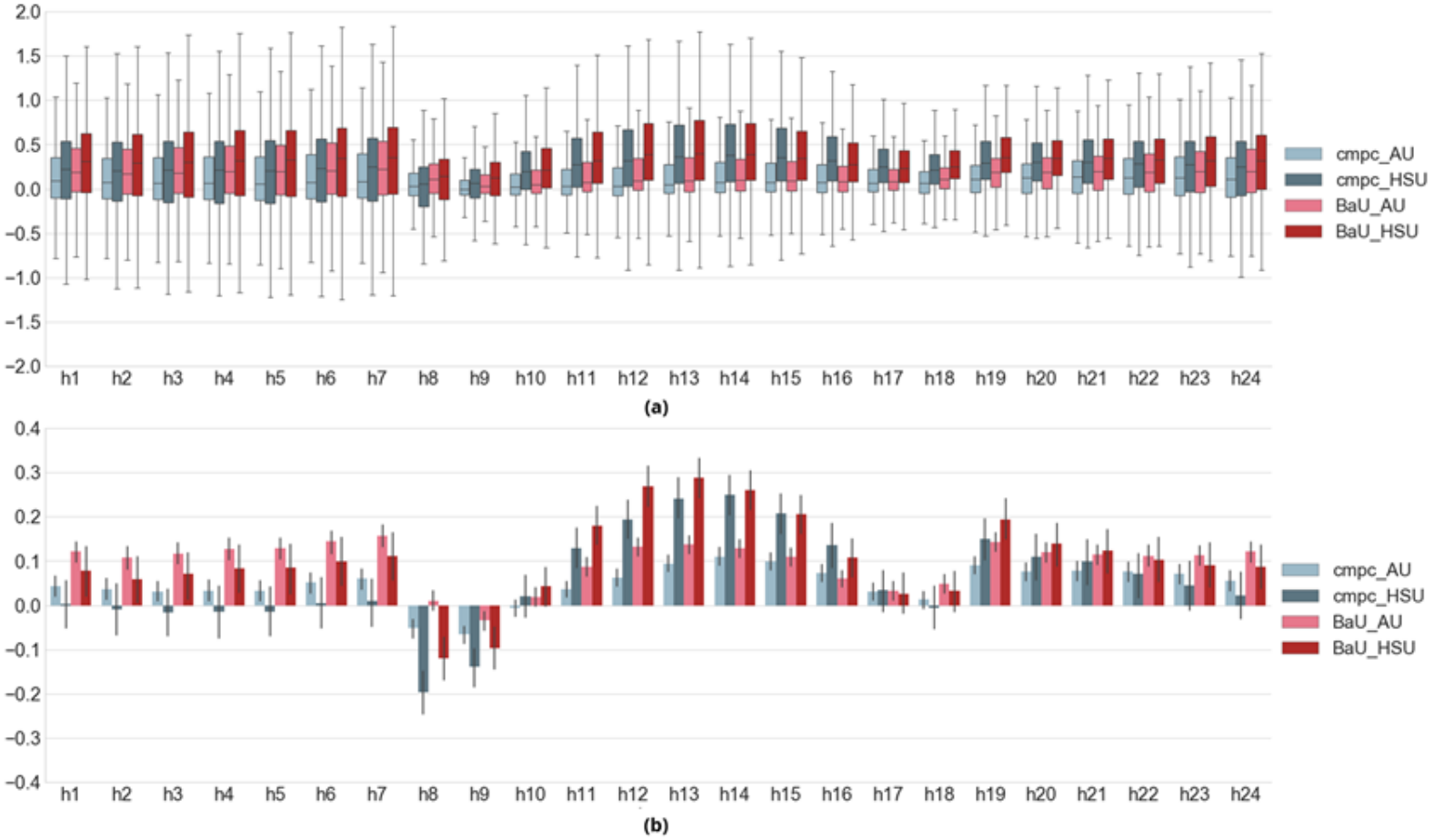

Figure 6.6: Statistical analysis temperature changes solely from urban effect (vertical axis shows temperature change from present to future in °C; h1, h2, ⋯, h24 define hourly variation) based on urban effects (i.e., future cases of compact (BaU) minus the intermediate cases of RCP2.6 (RCP8.5)): (a) 10-year averaged spatiotemporal hourly-temperature change in distribution for the AU and HSU in Compact(BaU) urbanization scenario; (b) the same as (a) but for the average value, where the error line shows the 95% confidence interval.

6.4 Discussion

The findings of this study imply that the effect of combined climate change and local urbanization is highly varied at a 1km resolution, despite the overall small average values. The urbanization effect itself strongly related to how urban parameters and AHE change in the future projected in each scenario. Depending on how future urban configuration and heat emission change, the urbanization effect may increase or decrease temperature in certain grids. Similar study of Doan and Kusaka (2018) conducted in Greater Ho Chi Minh city, Vietnam, which is comparable with Greater Jakarta, showed the future urban effect could reach $0.5°C$ spatially-averaged in HSU area. It is to be noted that study on Ho chi minh city and Hanoi only use land use criteria as land use change reference and geographical boundary, therefore the result is somehow homogenous, independent of urban parameterization. On the other hand, we found that in Greater Jakarta the urban effect itself is quite insignificant as spatially-averaged value, but the spatial-variation range is more critical ($0.05 \pm 1.02°C$ and $0.10 \pm 1.05°C$ for compact and BaU scenario in HSU area). Some grids had temperature increases due to urban effects that were close or larger in magnitude to those caused by global effects. As such, these grids may represent areas that are particularly vulnerable to urban climate change risks. The location of Greater Jakarta in tropical area is considered as the main cause of averagely low urban effect that is dominated by synoptic scale effect (Varquez and Kanda, 2018).

Comparing the combined global and urbanization scenarios, implementing the RCP2.6&Compact scenario could suppress the impact of climate change in urban areas. By consequence, the RCP2.6&Compact scenario was associated with a lower future temperature increase. Moreover, the compact scenario promoted a centralized and smart city design, which could increase urban resilience in rela-

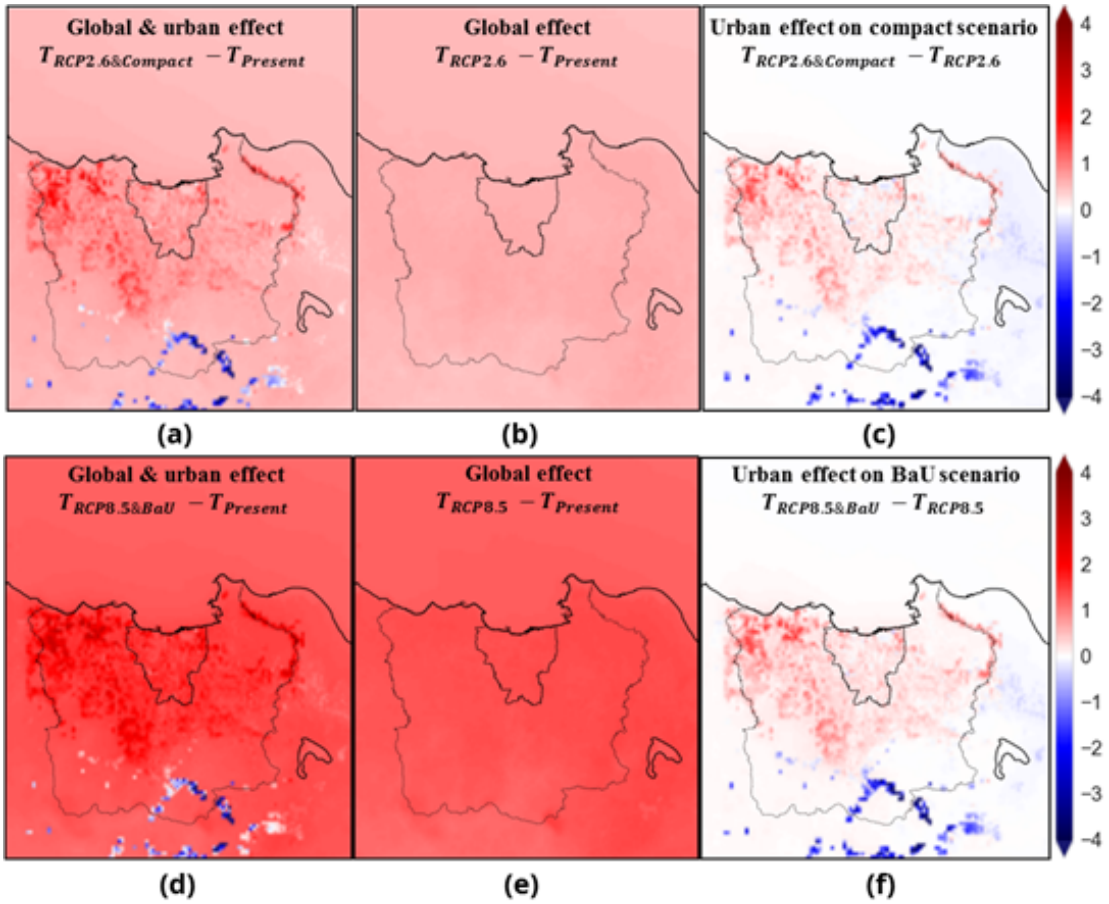

Figure 6.7: Spatial average of the 10-year 2-m temperature change between the present and future (°C): temperature change based on the global climate change and local urbanization scenarios for the RCP2.6&Compact (a) and RCP8.5&BaU (d); temperature change solely due to global climate change for RCP2.6 (b) and RCP8.5 (e); temperature change solely from local urbanization effect under the compact (c) and BaU (f). The inner solid black line represents Jakarta and outer line represents Greater Jakarta.

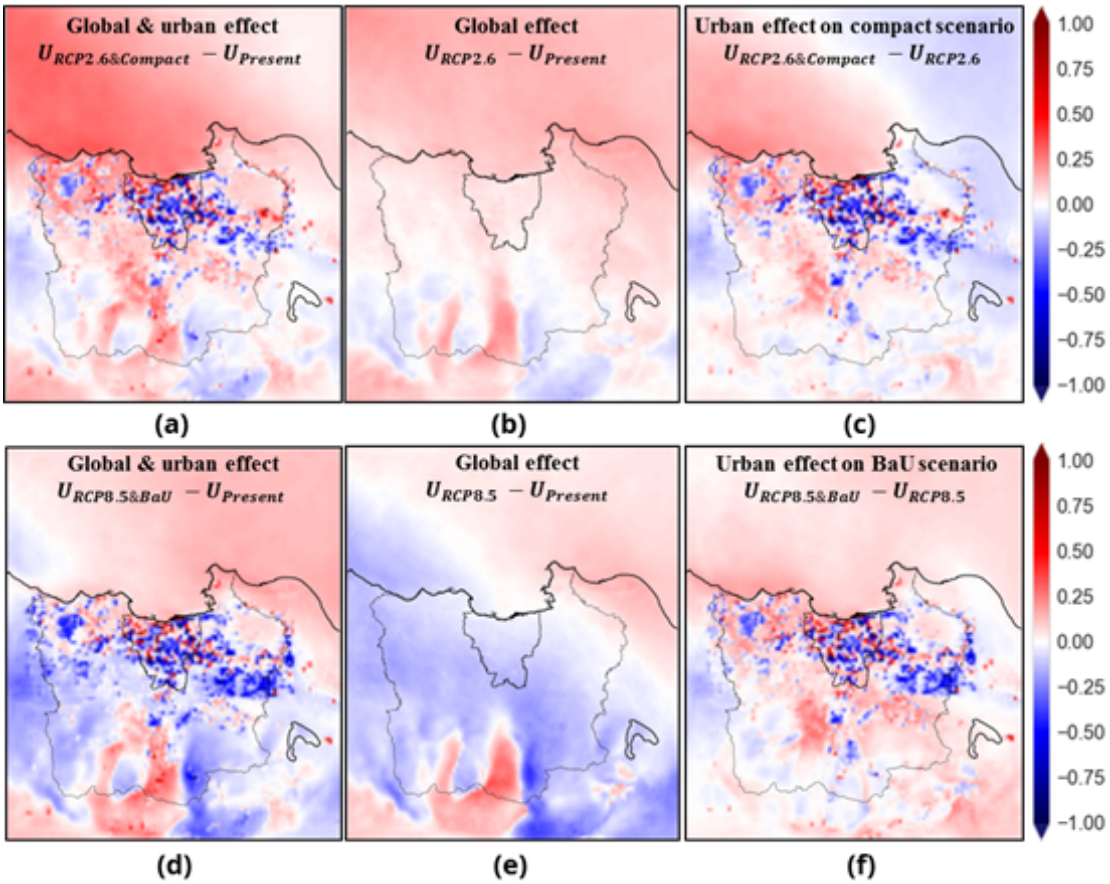

Figure 6.8: Spatial average of the 10-year change in 10-m wind speed between the present and future (m/s): wind speed change based on the global climate change and local urbanization scenarios RCP2.6&Compact (a) and RCP8.5&BaU (d); wind speed change solely due to global climate change for RCP2.6 (b) and RCP8.5 (e); wind speed change solely from local urbanization effect under the compact (c) and BaU (f).

tion to the impacts of climate change. By contrast, lower restrictions on urban planning could realize the RCP8.5&BaU scenario, which could increase urban temperatures up to $3.4^{\circ}C$ from present conditions (Figure 6.7), particularly in dense residential areas in the northwestern area of Greater Jakarta. Such high temperature increases could drastically increase the vulnerability of the population to heat stress and the energy demand for cooling.

The RCP8.5&BaU scenario resulted in lower wind speeds due to higher changes in surface roughness in the future, increasing the associated drag. This was especially notable in the southeastern area of the future urbanized area of Greater Jakarta (Figure 6.8). Effect of the urban area solely under local urbanization effect in compact (Figure 6.8(c)) and BaU (Figure 6.8(f)), showing that d and z_0 have a linear relationship on wind speed. Wind drag could reduce urban atmospheric circulation and advection cooling from sea and mountain breezes. The projected urbanized area on the outskirts of Jakarta had a greater impact on the urban effect than that of the city center. Therefore, controlling sprawl in these areas should be considered given the potential impact on the future population. Mitigation and adaptation strategies that support the RCP2.6&Compact scenario are highly recommended.

We found that both urban morphological and aerodynamic parameters and AHE had substantial effects on shaping urban climate characteristics, regardless of two-dimensional urban land use expansion. The daytime urban effect was larger than that at night in terms of average magnitude; however, the spatial variance of the nighttime urban effect was greater. Moreover, an average urban cooling effect around $0.2^{\circ}C$ was observed immediately after sunrise under both scenarios, with greater cooling under the compact scenario (Figure 6.6). The logical explanation is that there was a lower albedo under the compact scenario due to the presence of deeper urban canyons, thereby lowering the temperature due to the lower amount

of radiation received in the early morning. Overall, the magnitude of the urban effect in the study area was lower than the maximum tropical UHI value or typical subtropical and mid-latitude values (Wienert and Kuttler, 2005).

Negative temperature changes were predicted around hilly areas close to the mountain perimeter in the southern outskirts of Jakarta. This temperature decrease may be due to urban mixed-topography effects from coastal to mountainous areas, creating a cool zone around the mountain base (Lebassi-Habtezion et al., 2011). However, further studies are recommended to clarify this result.

The daily analysis of the urban effect during sea-breeze days showed that the urban area could act as an obstacle to sea-breeze penetration, resulting in increased temperatures further inland. Under the RCP8.5&BaU scenario, this mechanism could induce earlier thermal convection areas, compared with the present, resulting in a higher atmospheric boundary layer. By contrast, this phenomenon was less significant under the RCP2.6&Compact scenario. Urban areas as wind obstacles were observed not only during the day, when sea breezes penetrated inland, but also at night under land-breeze conditions. Land breezes from higher-altitude areas in the southeastern outskirts of Jakarta were impeded due to the urban effect, resulting in a higher nighttime UHI. Although not considered in this study, dispersion of air pollutants can be deduced. Given Jakarta's sea/land breeze circulation and its mixed topography, downwind areas in the southern outskirts will tend to have higher air pollutant concentrations due to its advection from the bay to the downwind city areas. At night, air pollution returns to the bay area, degrading the air quality in the northern coastal area of the city (Oke et al., 2017).

As limitations of this study, there are some concerns regarding the empirical equations used to derive the estimated urban parameters. Further improvements, by including more cities and a deeper analysis based on conditions unique to

particular cities, such as regional, background climate, and cultural effects would be likely to improve the equations. Moreover, model validation with observation stations showed higher error and bias during the day compared to night. This error may have been inherited from the surface radiation budget calculations in the SLUCM combined with the NOAH land surface model (Salamanca et al., 2018), further analysis should be considered.

6.5 Summary

Projections of the future climate of tropical, rapidly urbanizing megacities cannot rely solely on the effects of emission scenarios. The results of this study imply that urban effects can reach the same magnitude as global effects. Even though urban signals dominated the climate signal by an average factor of 12.2 (13.0) under the RCP2.6&Compact (RCP8.5&BaU) scenario, the findings showed that the urban signal distribution values were highly and significantly spatially diverse. In order to perform vulnerability studies, investigating over combinations of global climate and local urbanization are necessary. Several realizations of the same urbanization policies (e.g. BaU) would also be required. This would allow to determine the areas that are vulnerable in most realizations, and could then be considered as a reliable projection of future vulnerable urban areas.

Overall, mitigation and adaptation efforts based on urban planning in Greater Jakarta should strive to meet the conditions of the RCP2.6&Compact, since temperature change trends will otherwise follow the RCP8.5&BaU scenario, with no strict regulation on urban planning. The implications of the adaptation efforts under the RCP2.6&Compact scenario could reduce the effects of warming in newly urbanized areas. Focusing on urban ventilation, a strategy mirroring the RCP2.6&Compact scenario could improve urban wind ventilation by reducing urban roughness in the outskirts of Jakarta. Furthermore, it could prevent daytime

and nighttime air pollution by promoting effective wind circulation.

The results of this study imply that a compact concept of urban development could prevent future warming. Because the input data were constructed from globally available data sources, this study also aimed to fill the gaps in urban climate research between tropical and mid-latitude cities, especially other cities in developing countries. Therefore, this strategy should be considered not only for Greater Jakarta but also for other developing cities located in Am/Af climate zones experiencing rapid urbanization.

7

Future heat-related mortality projection

7.1 Introduction

Future temperature change in urban area affect directly to urban dwellers. Direct impact on higher temperature exposure is the heat-related mortality (Hales et al., 2014; Honda et al., 2014) and energy consumption for space cooling (Isaac and van Vuuren, 2009). In addition, heat wave will emerge in the future climate and the effect is exaggerated in urban area (Lemonsu et al., 2015; Wouters et al., 2017; Zhao et al., 2014). Therefore, the phenomena will place urban dwellers as the most vulnerable population in the future world, especially elderly, low-income populations, and those without access to cooling facilities (Patz et al., 2005). Furthermore, sleep disturbance cases are projected to increase due to higher future temperature (Obradovich et al., 2017; Rifkin et al., 2018). People with cardiovascular or respiratory disease, diabetes, chronic mental disorders, or

other preexisting medical conditions are at greater risk from heat exposure (Kovats and Hajat, 2008). Higher temperature may also trigger higher rate of tropical disease such as it gives better environment for malaria and dengue vectors (Rueda et al., 1990; Whitmire et al., 1987).

Correlation between heat-related mortality and climate change shows that implication of scenario on low adaptation-mitigation strategy implied on 0.1 –0.6% heat-related excess deaths in 2050 where Asian countries are the most vulnerable ones (Hales et al., 2014). Previous studies implied that optimum temperature (OT) and relative risk of death due to mortality can be featured in V-shaped relation (Honda et al., 1998, 2007). OT is defined as a temperature value where the minimum mortality value observed as a function of daily maximum temperature (Takahashi et al., 2007) or mean temperature (Gasparrini et al., 2015). Following this definition, OT can also be defined as the most comfortable day by means of daily mean or maximum temperature. Figure 7.1 illustrates the OT and heat-related mortality relative risk relationship. First global analysis on the OT and heat-related mortality relative risk (OT-RR) shows that OT lied on the 84^{th} percentile of annual daily maximum temperature distribution (Honda et al., 2014). However due to limitation, this study is still limited to developed countries and data sourced from developing and tropical countries are not included. This condition makes the OT as 84^{th} percentile rule in the developing tropical countries become arguable.

Study by Gasparrini et al. (2015) reveals that both heat and cold as function of daily mean temperature value are affecting temperature-related mortality risk. The geographical scope of this study is including tropical, subtropical, mid-latitude, and high-latitude countries. From this study, it is apparent that in (sub)tropical countries (e.g., Thailand, Brazil, Taiwan) the OT is shifted left-side to around 60^{th} percentile of daily mean temperature data distribution. In

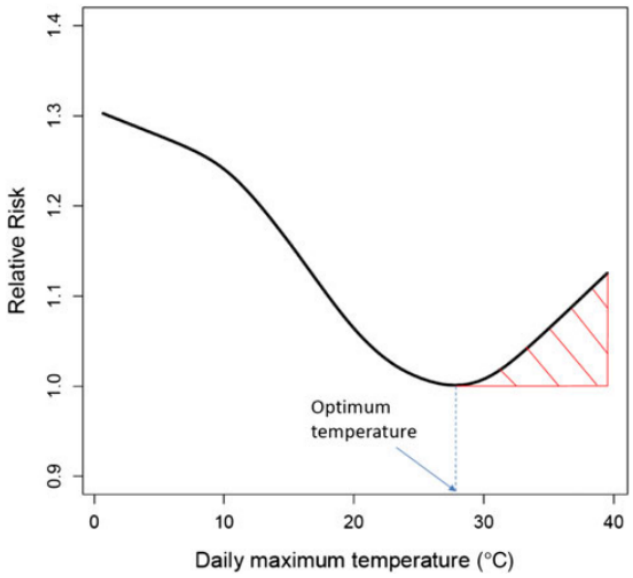

Figure 7.1: Heat-related mortality, considered as the shaded area. Taken from Honda et al. (2014)

(sub)tropical countries however, the temperature mortality relative risk only related with hot temperatures since the winter season are still above 10°C. Meanwhile, the OT in mid-latitude countries (e.g., Japan, South Korea, China, Canada, USA) agrees with Honda et al. (2014)'s study, ranging from 81^{st} to 89^{th} percentile of daily mean temperature distribution. The study also found that in high-latitude country (e.g., Sweden), the OT is shifted right to 93^{rd} percentile.

Mentioned studies were conducted for global analysis and the they also analyzed the future prospect of temperature-related mortality under climate change scenarios and population changes. However, due to global application reason, the spatial resolution of these studies are pretty coarse (i.e., approx. $\sim$ 55km grid resolution). The coarse resolution is considerably insufficient to analyze up into district administration level, where the crucial planning on adaptation strategy is happening. Therefore, this current work aims to project future heat-related mortality for Greater Jakarta using 1km high-spatial-resolution temperature pro-

jection data obtained from previous conducted simulations result. We adapt the V-shape OT-RR analysis method in this study with OT modification to 60^{th} percentile following results of Gasparrini et al. (2015) for Bangkok, which is quite resemblance of Great Jakarta in geographical and urban-socio-economic condition. The target year is 2050 following this study's target year. This study targets heat-related mortality projection based on two scenarios: (1) No adaptation scenario where the temperature change following the results of RCP8.5&BaU, and (2) Best adaptation scenario where the temperature change following the results of RCP2.6&Compact. The effect of humidity is neglected in this study following the insignificant effect reported in Honda et al. (2000), especially in an area in less-varied humidity such as Greater Jakarta (Sintorini, 2018).

7.2 Data and methodology

7.2.1 Daily temperature data and optimum temperature estimation

In this study, we collected daily temperature data (i.e., mean, minimum, and maximum) from 3-hourly public weather station report database www.ogimet.com. We obtained the data for all days from 2006 to 2015 from 2 World Meteorological Stations in urban area Jakarta: KMO and TPR. These stations are selected due to their location in the center of urban area which is representative in determining thermal condition in built-up area. All repositories were downloaded automatically through linux environment system. The original data is in ASCII text form. Data processing were done using Python script. The final form of the database is contained with timestamp (i.e., in year, month, day, hour), station code, daily temperature mean ($\mathrm{Td}_{\mathrm{mean}}$), and daily temperature maximum ($\mathrm{Td}_{\mathrm{max}}$).

Once the dataset is configured, statistical analysis using python programming language was conducted to define temperature data distribution on $\mathrm{Td}_{\mathrm{mean}}$

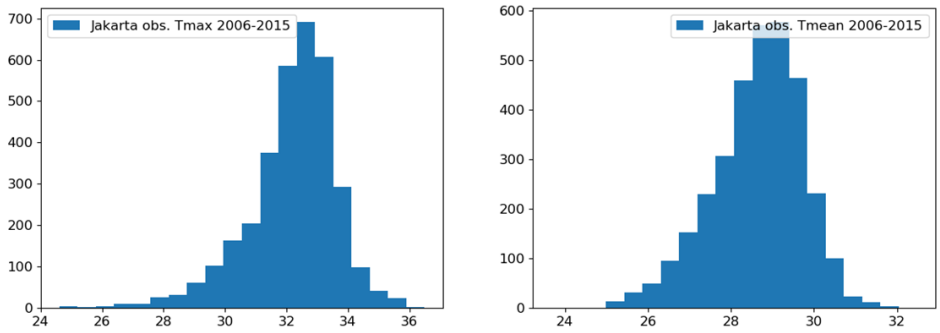

Figure 7.2: Td_{max} (left) and Td_{mean} (right) data distribution over 10 years (i.e., all months) averaged from KMO and TPR

and Td_{max}. The data distribution results are shown in Figure 7.2. Linear correlation analysis was conducted to find the relationship between Td_{mean} and Td_{max} during 2006-2015. The results show that $Td_{mean} = 0.74(Td_{max}) + 5.42$ with pearson correlation value equal to 1.0. This states that the use of Td_{mean} and Td_{max} are interchangeable in the further analysis.

From the timestamped daily temperature database acquired from KMO and TPR in daily resolution from 2006 to 2015, the data is further processed to define the 60^{th} percentile value. The results show that 60^{th} percentile value is 29.2°C and 32.8°C in function of Td_{mean} and Td_{max} respectively, averaged from both stations. These temperatures are used as OT reference value in the corresponding further analysis.

7.2.2 Bias correction method

In the results of Chapter 5, it is found that the model has positive bias on temperature value when compared with stations' temperature data. Since the OT for heat-related mortality analysis is calculated from observation stations' data, thus the model result need to be adjusted to be comparable with referenced OT. For temperature bias adjustment, statistical bias adjustment method (Piani et al.,

2010a) is used. This method was developed to correct general climate model result on temperature and precipitation prediction/ projection to real observed values (Piani et al., 2010b). Therefore, the statistical bias adjustment method is quite suitable to be applied in this study.

The concept of bias statistical correction method is involving a development of transfer function derived from cumulative distribution functions (CDFs) of observations and model simulations. The corrected variable x_{cor} is a function of the modeled counterpart, $x_{cor} = f(x_{mod})$. The transfer function (henceforth, TF) is such that the intensity histogram of the corrected variable x_{cor} matches the intensity histogram of the observed x_{obs}. The first step includes creating probability density function (PDF) from histogram of 10-year daily temperature data in each grid. In case of temperature, the PDF usually formed as bell-shaped function, thus representing normal distributed data. The TF as function of x_{mod} (i.e., $TF(x_{mod})$) can be derived by first calculating the cumulative distribution functions (CDF) and then associating to each value of x_{mod} the value x_{obs} such that,

$$CDF_{mod}(x_{mod}) = CDF_{obs}(x_{obs}) \tag{7.1}$$

As mentioned before, temperature distribution PDF resembles a bell-shaped curve or following Gaussian distribution. When this holds, the TF to correlate between histogram of observed and model can be well represented by linear TF which is in function of mean and standard deviation. Therefore, $TF(x_{mod})$ for present temperature can be expressed as follow.

$$TF(x_{mod,present}) = CDF_{obs}^{-1}(CDF_{mod,present}(x_{mod,present})) \tag{7.2}$$

Figure 7.3 illustrated the bias correction process.

Figure 7.5 shows the simulations' adjusted temperature compared with

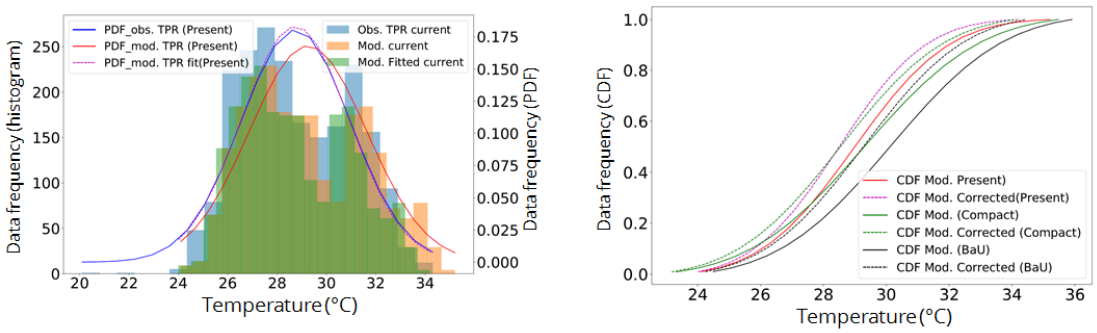

Figure 7.3: Illustration of bias correction in an urban grid.

observation point. Compared with Figure 5.4, bias corrected simulation result is now closer to observation value, especially on higher temperature which is very much sensitive in this chapter. The result of statistical bias adjustment for $\mathrm{Td}_{\mathrm{max}}$ averaged for 10-year August is as illustrated in Figure 7.4. Using linear TF for bias correction, the results show that city center will have the highest 10-year averaged $\mathrm{Td}_{\mathrm{max}}$ compare with outskirt surrounding areas.

For future case which includes shifting of temperature to right tail in the future temperature histogram, a straight forward assumption using shifting of mean and standard deviation is used (Piani et al., 2010b) and is expressed as follows.

$$\begin{aligned} \mu^{\mathrm{correct}}_{\mathrm{mod,future}} &= \mu_{\mathrm{obs}} + \frac{\sigma_{\mathrm{obs}}}{\sigma_{\mathrm{mod,present}}}(\mu_{\mathrm{mod,future}} - \mu_{\mathrm{mod,present}}) \\ \sigma^{\mathrm{correct}}_{\mathrm{mod,future}} &= \frac{\sigma_{\mathrm{obs}}}{\sigma_{\mathrm{mod,present}}}\sigma_{\mathrm{mod,future}} \end{aligned} \tag{7.3}$$

Therefore, TF for future will be expressed as,

$$\mathrm{TF}(x_{\mathrm{mod,present}}) = \mathrm{CDF}^{-1}_{\mathrm{mod,future}}(\mu^{\mathrm{correct}}_{\mathrm{mod,future}}, \sigma^{\mathrm{correct}}_{\mathrm{mod,future}}) \tag{7.4}$$

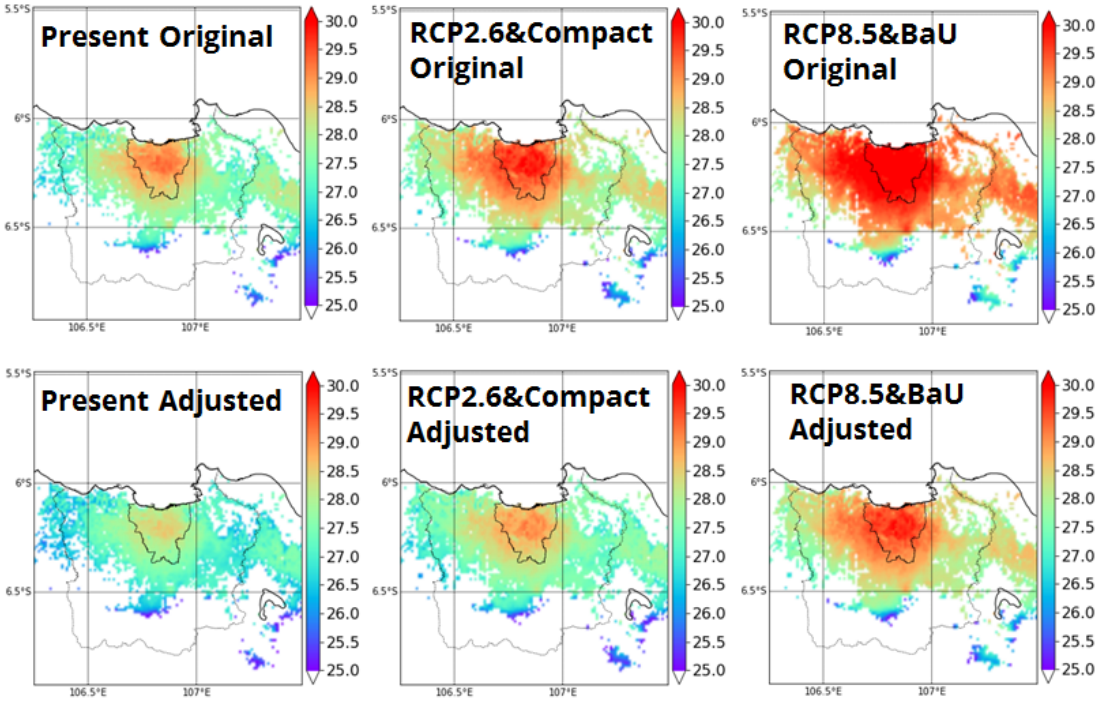

Figure 7.4: Simulation results' Td_{max} before and after bias correction for present and future. Units in °C

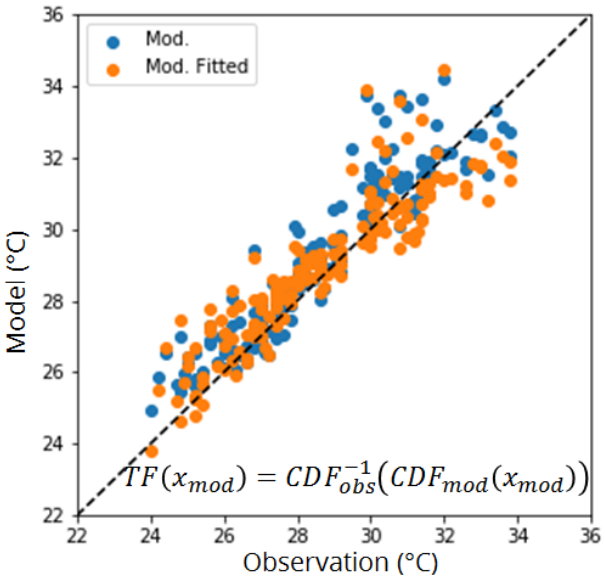

Figure 7.5: Temperature bias correction result (y-axis) compared with observation (x-axis). Blue dots show simulation result before bias correction and orange dots after correction.

7.2.3 Optimum temperature and heat-related relative risk calculation

Projecting heat impact on the future population cannot be conducted without considering how the age distribution will be in 2050. This is very crucial since Jakarta has distinct population characteristic as the middle-class population is emerging in present (2010s). The population of Jakarta in 2050 is expected to have balance proportion from old ages to young ones. National Development Planning Agency Republic of Indonesa (Bappenas) of Jakarta issued the prediction of population pyramid for every 5 years since 2020 to 2035 (Badan Pusat Statistik, 2013) as shown on Figure 7.6. From this local dataset we found empiral function

Figure 7.6: Projected population pyramid for estimating the future proportion of population > 65yrs. old

of age >65 is as follow.

$$R_{65_{year}} = 4 \times 10^{-48} \times \exp(0.00525 \times \text{year}) \tag{7.5}$$

where, year = target year. Daily crude rate per 1000 population is expressed as 0.0095/1000 population and 0.0306/1000 population for 2014 and 2050 respectively. Combining these factors then we can estimate the proportion projection for > 65yrs. old population.

As mentioned previously, there is a certain discrepancy of estimating OT

in mid-latitude and tropical countries. In this study, the OT is estimated as 60^{th} percentile of Td_{max} data from 10-year daily temperature maximum data averaged from KMO and TPR. Based on the calculation, the result showed that $32.8°C$ is the estimated OT value for Td_{max} (i.e., $OT_{Td_{max}}$).To define OT-RR correlation function, reconstruction of result from Gasparrini et al. (2015) for Bangkok, Thailand was done. The function is described as follows.

$$\begin{aligned} RR_{i,j} &= 0.0125(x_{i,j})^2 + 0.025(x_{i,j}) + 1 \\ x_{i,j} &= Td_{max_{i,j}} - OT_{Td_{max}} \end{aligned} \tag{7.6}$$

where $RR_{i,j}$ is the relatve risk of mortality at temperature ($Td_{max} - OT_{Td_{max}}$) and i,j refer to grid coordinate.

Finally, the heat-related mortality is calculated using empirical function of Hales et al. (2014); Honda et al. (2014) and modified with Bangkok, Thailand (Gasparrini et al., 2015) is as follow.

$$\begin{aligned} \text{Heat related deaths} &= D_{av} \times 0.60 \times (RR_{i,j} - 1) \\ D_{av} &= \text{daily crude mortality}_{year} \times R_{65_{year}} \end{aligned} \tag{7.7}$$

where D_{av} is the daily average number of deaths in > 65yrs. old population. Details on programs for OT-RR calculation is presented in Appendix B.

7.3 Results and Discussion

This study remarks the prime approach on heat-related mortality due to global climate change and local urbanization effect in a rapidly developing megacities. The target year of 2050 is an intermediate future target which is necessary for mid-term adaptation strategy. By applying empirical relationship on optimum daily maximum temperature and relative risk mortality due to temperature, we can project the heat-mortality risk in the future based on projected future temperature

done in Chapter 6.

In Greater Jakarta, the results of future $\mathrm{Td}_{\mathrm{max}}$ in statistical histogram and spatial distribution is shown in Figure 7.7 and Figure 7.8, respectively. The median value of present $\mathrm{Td}_{\mathrm{max}}$ is $33.2°\mathrm{C}$, and for the future is $34.6°\mathrm{C}$ and $33.8°\mathrm{C}$ for RCP8.5&BaU and RCP2.6&Compact respectively. Based on the distribution, future maximum $\mathrm{Td}_{\mathrm{max}}$ is located at $36.0°\mathrm{C}$ in no-adaptation RCP8.5&BaU scenario. Following study by Takahashi et al. (2007), the extreme temperature is achieved when the temperature fulfill $\mathrm{OT} + 5$ or equal to $37.8°\mathrm{C}$ for current study on Greater Jakarta. Thus, assuming current applied scenarios, Greater Jakarta will not experience any extreme condition on heat-related mortality. In addition, such extreme weather or heat wave is naturally difficult to occur in tropical area where Greater Jakarta is located due to low-pressure area, even in the future climate.

In this study, we adapt the OT-RR empirical relation to project high-resolution heat-related mortality number for population older than 65 years old using the methods defined previously. Future population projection has been done previously in Chapter 5. Then, the ratio of population > 65 year old is calculated as defined in section 7.2.3 of this chapter. Figure 7.9 shows the spatial distribution of projected heat-related mortality in Greater Jakarta in 2050 using two scenarios: (1) RCP8.5&BaU comprises no-mitigation-adaptation strategy, and (2) RCP2.6&Compact comprises best mitigation-adaptation strategy. Figure 7.10 illustrated the heat-related mortality risk per 100,000 population. It is expected that best mitigation-adaptation strategy can reduce the heat-mortality risk to around 40-50% from no-mitigation-adaptation scenario.

The report of WHO (Hales et al., 2014) showed that in 2050 the heat-related mortality around Greater Jakarta area without any mitigation strategy is more that 75 annual deaths for population more than 65 years old. However,

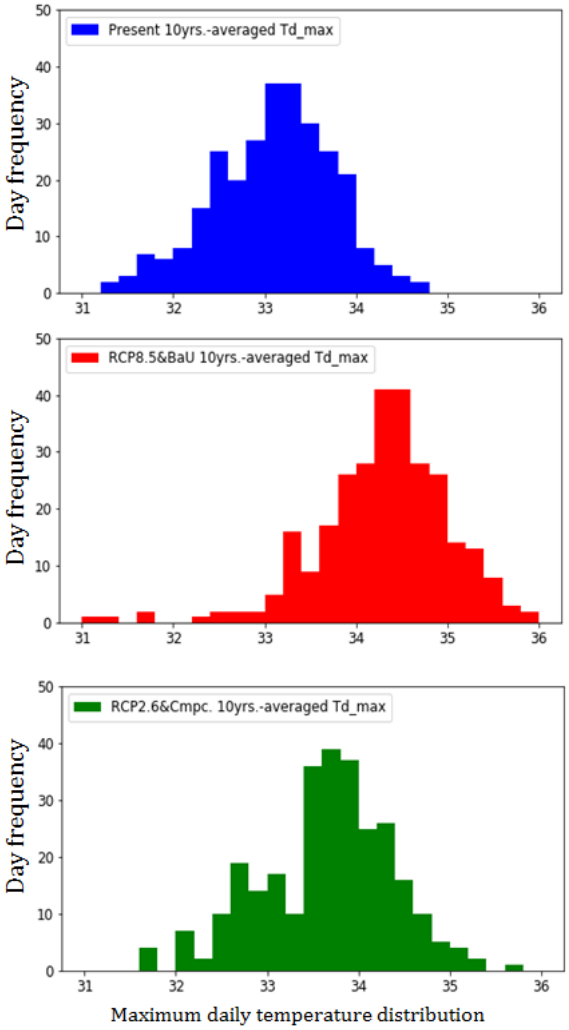

Figure 7.7: Projected Td_{max} histogram distribution averaged from 2046-2005 for Greater Jakarta

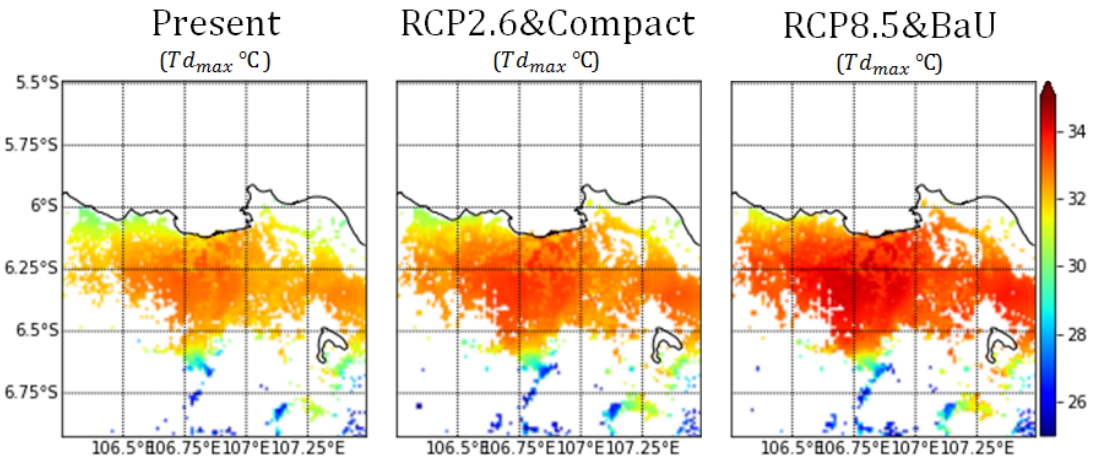

Figure 7.8: Projected Td_{max} spatial distribution averaged from 2046-2005 for Greater Jakarta

this result is very much coarse as it is conducted in $0.5° \times 0.5°(\sim 55\text{km})$. This number is approximately equal to 0.0037 daily deaths/km^2. However, downscaling to 1.2km resolution as conducted in this study, the value can be varied much with WHO results where the risk value can reach more than 0.005 daily deaths/km^2 (Figure 7.9). Hence, assuming scenario conducted in current study, stakeholders can have better spatial recognition on higher vulnarable district regarding future heat risk.

7.4 Summary

People adaptation ability is quite related with background climates. Tropical area people may suffer less to heat increase than those who are settled in higher latitude. This is represented by the shifting of OT to the left-tail of temperature distribution data to 60^{th} percentile from 84^{th} percentile in mid-latitude countries. The reader should bear in mind that the OT for (sub)tropical countries are limited to data collected in Thailand, Brazil, and Taiwan following study of Gasparrini et al. (2015). Future studies in gaining data for more broad range of tropical

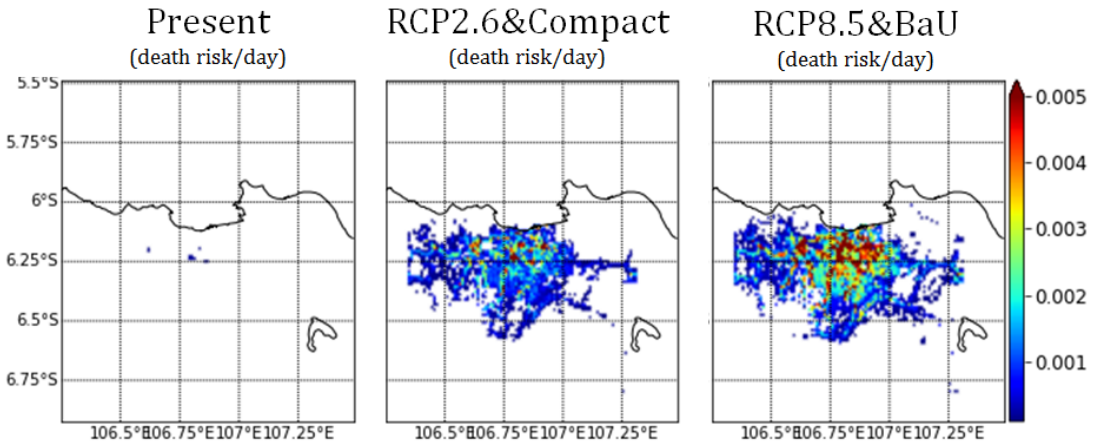

Figure 7.9: Spatial distribution of projected heat-related mortality in Greater Jakarta in 2050 (i.e., multiplied by gridded projected 2050's $>$ 65yrs. old population)

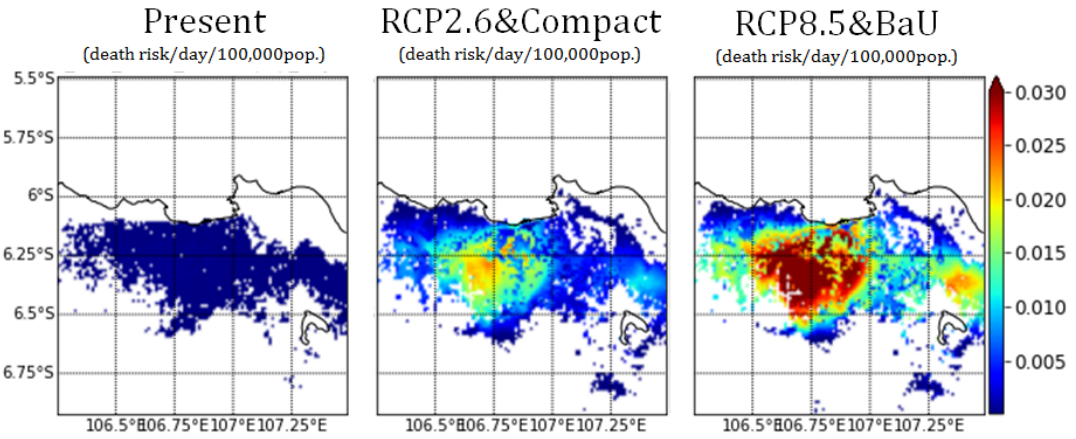

Figure 7.10: Spatial distribution of projected heat-related mortality in Greater Jakarta in 2050 per 100,000 population of $>$ 65yrs. old

countries and cities are very much worthwhile.

Even though global study on predicting future heat risk on mortality is strongly importance, it's coarse resolution could be an obstacle in defining a detailed, district-scale study of local adaptation strategy which is more practicable for local stakeholders. Thus, higher resolution approach is very much important. The downscaling approach should maintain the presence of global climate change impact, urbanization effect, and population projection including age distribution projection (i.e., older population that is expected higher in risk).

The findings of this chapter makes a prime study on OT-RR empirical function implication on 1km high-resolution to project future heat-related mortality in target area of Greater Jakarta. This study provides an insight of how mitigation-adaptation strategies could leverage the heat-related mortality risk in urban area. No-mitigation-adaptation scenario assumed in this study as RCP8.5&BaU scenario, may escalate heat-mortality risk to 0.03 daily deaths$/\text{km}^2/100,000$ populations $>$ 65 yrs. old or up to 0.005 daily deaths$/\text{km}^2$ for projected future $>$ 65 yrs. old populations. On the other hand, a best mitigation-adaptation strategy assumed as RCP2.6&Compact scenario is potentially reducing this values to 40-50%.

8

Concluding remarks

8.1 Introduction

This chapter is aimed to summarize all the work done in previous chapters and conclude the findings of this research. The general objective of this research is to find a solution on how to predict and project present and future urban climate in a tropical megacity in developing country through numerical simulations, and how it impact the future populations. The challenges of conducting such urban climate study in developing countries are related to data scarcity and selection of realistic future scenarios affecting urban climate without local stakeholders' support. Furthermore, this study targets a generic, representative, repeatable, and realistic framework of urban climate study global approach. The findings should make important contribution to scientific and general communities in communicating and building public awareness on urban climate problem.

8.2 Research findings

There are several new findings addressed in this study as mentioned in each chapter previously. To summarize the discussions, the major findings of this study is as follows.

1. In representing realistic urban morphological features, global coverage and zero-cost satellite imageries can achieve sufficient 1km resolution of bulk urban parameters: λ_p , λ_f , H_{ave} , d , z_0.

2. Empirical equations were derived to estimate λ_p and λ_f from Landsat 8 images. Good agreement was achieved when they were compared with the actual λ_p and λ_f values. Using a neural network, subtracted ASTER-GMTED data were combined with the DMSP-OLS nightlight image to define a function for deriving H_{ave} in 1km resolution.

3. Including urban parameters derived from global datasets in the simulation provided better agreement, especially with regard to wind speed, than did a simulation that used the default parameters provided in the WRF/SLUCM model. The improved representation of wind speed and thereby improving temperature, especially improvement in nighttime wind speed over the urban area.

4. Application of satellite-derived urban parameters in WRF/SLUCM simulation gives evidence of simple and zero-cost solution in conducting mesoscale urban climate analysis in developing cities that mostly lack of actual building database, such as Asian megacities.

5. Using PGW dynamical downscaling from GCM and applied it in RCM is sufficiently providing future meteorological boundaries on background climate condition and mitigation scenarios. On the other hand global SSP

model results provide a general country's socio-demographic parameters in the future which can be derived to predict future city's population and energy consumption. Using empirical function on GDP and population with urban morphological parameters, future urban parameters are projected accordingly.

6. The results of this study imply that urban effects can reach the same magnitude as global effects in tropical city. Even though urban signals dominated the climate signal by an average factor of 12.2 (13.0) under the RCP2.6&Compact (RCP8.5&BaU) scenario, the findings showed that the urban signal distribution values were highly and significantly spatially diverse.

7. Lower restrictions on urban planning could realize the RCP8.5&BaU scenario, which could increase urban temperatures up to $1.47 \pm 1.38°C$ from present conditions. Otherwise, best mitigation-adaptation strategy promoting urban resiliency of RCP2.6&Compact planning could minimize the temperature increase to $0.66 \pm 0.67°C$.

8. Mitigation and adaptation efforts based on urban planning in Greater Jakarta should strive to meet the conditions of the RCP2.6&Compact, since temperature change trends will otherwise follow the RCP8.5&BaU scenario, with no strict regulation on urban planning. The implications of the adaptation efforts under the RCP2.6&Compact scenario could reduce the effects of warming in newly urbanized areas.

9. This study provides an insight of how mitigation-adaptation strategies could leverage the heat-related mortality risk in urban area. Without any mitigation and adaptation scenario assumed in this study as RCP8.5&BaU scenario, may escalate heat-mortality risk to 0.03 daily deaths$/km^2/100,000$

populations $>$ 65 yrs. old or up to 0.005daily deaths/km^2 for projected future $>$ 65 yrs. old populations. On the other hand, a best mitigation-adaptation strategy assumed as RCP2.6&Compact scenario is potentially reducing this values to 40-50%.

8.3 Recommendations for further research

There is abundant room of improvement for further progress in present and future urban climate analysis and how its impact to the urban resiliency and society. Following are several recommendations for further works.

1. This study opens up huge opportunity on application of data sciences (i.e., big data, artificial intellegence, data mining) in the scope of urban climate study. We expect that through data sciences and advancements of smart cities, near-future global urban climate studies and practical application pursuing high-resilience cities can be accomplished. Using the advancements of big data and data processing, the empirical relationships to determine urban parameters also can be significantly improved.

2. Currently, we only used 3 cities to estimate present urban parameters and we understand that it is far from sufficient. Currently, our team are focusing on building database of urban parameters on 30 megacities, most of them are located in (sub)tropical area (e.g., Mumbai, Beijing, Delhi, Dhaka). To realize this, we challenge several approaches including:

    - Estimating urban parameters data based on socio-demographic parameters as mentioned in Kawano (2018), and Varquez et al. (2018). However, as socio-demographic parameter is not a direct physical relationship with geomorphological urban surface parameter, other supporting

parameter such as energy or nightlight, cultural, economy, or other possible parameter need to be research more.

- Using faster algorithm than what stated in this paper. Currently spectral angle mapping is used for urban land cover classification in λ_p, using random forest combined with cloud computing strategy can reach both speed and global approach (i.e. Google Earth Engine).
- For building height estimation, commercially available higher resolution stereo satellite such as TanDEM-X (Kent et al., 2019) can be useful to get a better result. For current improvement work, our team is using high-resolution satellite imageries from Pleiades (i.e. acquired from Pasco) for 30 megacities.
- International network such as WUDAPT (www.wudapt.org) project (level 1 and 2) which is collecting urban database including urban morphological data can be a good entrance. Using big data, we can acquire more input regarding building height in cities around the globe and application of machine learning to classified which parameters and inter-comparison of buildings height based on culture (i.e. related to architectural, height limitation, exclusive area), social entity, and regional common similarity.

3. The positive bias -especially during daytime- on current study simulation results are apparently related with systematical error due to urban surface energy balance model in SLUCM and land surface model of NOAH-LSM implemented in the model. This bias is amplified in tropical area due to large error on latent heat flux estimation. Improvement on urban surface model is very much worthwhile although currently it is out of scope of this study.

4. A simple yet efficient empirical relationship on optimum temperature and heat-related mortality risk in city-scale can leverage the importance of urban climate impact assessment. However, more research on OT-RR in wider range of background climates and cities' configuration needs to be undertaken. This is important to achieve more precise estimation of the location of OT and RR as function of temperature, since it is strongly depend on climate and people adaptability to climate.

5. Even though it is very much intereseting to analyze year to year trend of urban meteorological condition in span of 2006-2015 for present and 2046-2055 for future, the average condition is more to emphasize in such climate study.

6. There is a concern regarding supercomputing resource that was used for simulation calculation presented in this study may be a challenge to be applied in developing countries. To cope with this problem, several strategies that could be applied as solution to computational resource challenges in developing countries. Since WRF/SLUCM itself is an open-source software, the solutions mainly focusing on computational hour reduction and use of market-available computing hardware / electronics as follows.

    - Reduce simulation period, including reduction on spin-up period.
    - Use less target year for each present and future simulation (i.e. currently uses 10 years)
    - Decide representative few days in the target month before conducting the simulation. This method can be done using statistical analysis based on meteorological station data. Thus, one can reduce simulation days but still maintaining representativeness of the target month.

- Use of commercially available work station with an excellent system specification can be one of the solution.
- Related to point 4, approach on WRF/SLUCM for GPU computing is highly recommended. Recent GPU from NVIDIA or AMD which is originally intended for game performance can be tweaked to serve the purpose of weather simulation. However, there is challenge on adapting current environment setting since this research are done in Tsubame's CPU system.

8.4 Summary

Overall, the author wishes that this study could provide a comprehensive research on mesoscale urban climate study in present and future, also its implication to urban population. We are hoping that this study could facilitate a global cross-fields networks of scientists (e.g., meteorologist, climatologits, enviromental scientists) and design stakeholders (e.g., urban planners, architects, government officials, policy makers) in understanding more about the urban environment and be a base of future urban planning considerations.

A

Python programs for processing future urban parameters and AHE

A.1 Calculating future λ_p, λ_f and H_{ave}

```
#This program is based upon by the results of Kawano (2018), Varquez et
    al. (2017, 2018)
#which reveals dependency of urban parameters to existing global
    datasets
#such as the LandScan and VIIRS nightlights
#modified by Nisrina Setyo Darmanto using SSP data

import gdal
import arcpy
from arcpy import env
from arcpy.sa import *
import os
import numpy,glob
import time

def acquire(file):
    op   = gdal.Open(file,gdal.GA_ReadOnly)
    band = op.GetRasterBand(1)
    DATA = band.ReadAsArray(0,0,band.XSize,band.YSize)
    op   = None
    del band
    return DATA
```

```
def est_havg(pdfile,gdp,pdcountry,pdcityfile,outfile,pdnlfut): #put
    2050 pdnl input
   pdnl     = acquire(pdfile)
   pdnlmax  = numpy.max(pdnl)
   pdnlfut   = acquire(pdnlfut)
   pdnlfutmax = numpy.max(pdnlfut)
   npopviirs = pdnl/pdnlfutmax
   pdcity   = numpy.sum(acquire(pdcityfile))
   gdpcity  = gdp*pdcity/pdcountry
   alphaH   = 2.0e-11*gdpcity+9.80
   betaH    = -2e-12*gdpcity+9.18
   havg     = alphaH*npopviirs+betaH
   havg[(npopviirs==0.)|(pdnl<2000.)] = 0.
    #Create geotiff
   sel          = gdal.Open(pdfile,gdal.GA_ReadOnly)
   proj         = sel.GetProjection()
   col         = sel.RasterXSize
   row         = sel.RasterYSize
   geogtransform = sel.GetGeoTransform()
   outfile      = outfile
   outdriver    = gdal.GetDriverByName("GTiff")
   outdata      = outdriver.Create(outfile,col,row,1,gdal.GDT_Float32)
   outdata.GetRasterBand(1).WriteArray(havg)
   outdata.SetGeoTransform(geogtransform)
   outdata.SetProjection(proj)
   sel          = None
   outdata      = None
   return havg

def est_paifai(pdfile,outfile1,pdnlfut): #put 2050 pdnl input
   pdnl     = acquire(pdfile)
   pdnlmax  = numpy.max(pdnl)
   pdnlfut   = acquire(pdnlfut)
   pdnlfutmax = numpy.max(pdnlfut) #max (pd max 2050 adjusted data)
   npopviirs = pdnl/pdnlfutmax
   npopviirs[npopviirs>0.90086887835703]=0.90086887835703 #Must not
      drop after peak curve
   pai      = -0.2532*npopviirs*npopviirs+0.4562*npopviirs+0.1125
   pai[(npopviirs==0.)|(pdnl<2000.)] = 0.
   paif     = numpy.copy(pai) #Conditions for the frontal area index and
      plane area index relation
   paif[paif>0.45] = 0.45
```

```
    paif[paif<0.05] = 0.05
    fai      = 1.42*paif*paif+0.4*paif
    fai[(npopviirs==0.)|(pdnl<2000.)] = 0.0
     #Create geotiff
    sel         = gdal.Open(pdfile,gdal.GA_ReadOnly)
    proj        = sel.GetProjection()
    col        = sel.RasterXSize
    row        = sel.RasterYSize
    geogtransform = sel.GetGeoTransform()
    outfile     = outfile1
    outdriver   = gdal.GetDriverByName("GTiff")
    outdata     = outdriver.Create(outfile,col,row,1,gdal.GDT_Float32)
    outdata.GetRasterBand(1).WriteArray(pai)
    outdata.SetGeoTransform(geogtransform)
    outdata.SetProjection(proj)
    outdata     = None
    #outfile     = outfile2
    #outdriver   = gdal.GetDriverByName("GTiff")
    #outdata     = outdriver.Create(outfile,col,row,1,gdal.GDT_Float32)
    #outdata.GetRasterBand(1).WriteArray(fai)
    #outdata.SetGeoTransform(geogtransform)
    #outdata.SetProjection(proj)
    outdata     = None
    sel         = None
    return pai,fai


'''
##### Case for SSP3, No-change/business-as-usual scenario (historical)
#GDP2014MER = 368917900000 #SSP3_BaU_NoCC
#GDP2014PPP = 909291900000 #SSP3_BaU_NoCC
#INDPOP2014 = 239870900 #SSP3_BaU_NoCC
#GDP2050MER = 1122367000000 #SSP3_BaU_NoCC
#GDP2050PPP = 2766358000000 #SSP3_BaU_NoCC
#INDPOP2050 = 285081600 #SSP3_BaU_NoCC
directory = 'F:\\JakartaNewInputData\\'
pop       = directory+'historicalStrategy\\PrePop_Historical_2050.tif'
popviirs  = directory+'historicalStrategy\\historical_adj_2050.tif'
pdnl_2050 = directory+'historicalStrategy\\historical_adj_2050.tif'
    #put 2050 data here
file_out  = directory+'historicalStrategy\\historical_havg_2050.tif'
havg      =
    est_havg(popviirs,GDP2050PPP,INDPOP2050,pop,file_out,pdnl_2050)
```

```
arcpy.env.overwriteOutput = True
file_out1 = directory+'historicalStrategy\\historical_pai_2050.tif'
#file_out2 = directory+'historicalStrategy\\historical_fai_2050.tif'
pai,fai   = est_paifai(popviirs,file_out1,pdnl_2050)
    #(pdfile,outfile1,pdnlfut)
hst       = 1.05*havg-3.7
hst[havg==0.] = 0.
hmx       = 12.51*numpy.power(hst,0.77)

'''
# ##### Case for SSP1, Sustainability, taking the green road (compact)
GDP2014MER = 368941700000 #SSP1_BaU_NoCC
GDP2014PPP = 909350600000 #SSP1_BaU_NoCC
INDPOP2014 = 239870900  #SSP1_BaU_NoCC
#GDP2050MER = 1356944000000 #SSP1_BaU_NoCC
#GDP2050PPP = 3344533200000 #SSP1_BaU_NoCC
#INDPOP2050 = 270466100 #SSP1_BaU_NoCC
directory = 'F:\\JakartaNewInputData\\compactStrategy\\'
pop       = directory+'PrePop_Compact_2014.tif'
popviirs  = directory+'compact_adj_2014.tif'
pdnl_2050 = directory+'compact_adj_2050.tif'
file_out  = directory+'compact_havg_2014.tif'
havg      =
    est_havg(popviirs,GDP2014PPP,INDPOP20,pop,file_out,pdnl_2050)
file_out1 = directory+'compact_pai_2014.tif'
#file_out2 = directory+'compact_fai_2014.tif'
pai     = est_paifai(popviirs,file_out1,pdnl_2050)
    #(pdfile,outfile1,pdnlfut)
hst       = 1.05*havg-3.7
hst[havg==0.] = 0.
hmx       = 12.51*numpy.power(hst,0.77)
```

A.2 Calculating future d and z_0

```
#This program is based upon by the results of Kawano (2018), Varquez et
    al. (2017, 2018)
#which reveals dependency of urban parameters to existing global
    datasets
#such as the LandScan and VIIRS nightlights
#modified by Nisrina Setyo Darmanto using SSP data
```

```
import gdal
import arcpy
from arcpy import env
from arcpy.sa import *
import os
import numpy,glob
import time

def acquire(fff,numCols,numRows):
    nd          = gdal.Open(fff,gdal.GA_ReadOnly)
    band        = nd.GetRasterBand(1)
    xsize        = numCols
    ysize        = numRows
    DATA        = band.ReadAsArray(0,0,xsize,ysize)
    nd          = None
    del band
    return DATA


def est_dz(pdfile,havg,pai,fai,hst,hmx,outfile1,outfile2):
   #Affix constants
   a0 = 1.29
   b0 = 0.36
   c0 = -0.17
   with numpy.errstate(divide='ignore', invalid='ignore'):
      X = numpy.true_divide(hst+havg,hmx)
      X[ ~ numpy.isfinite(X)]=0
   #X = (hst+havg)/hmx
   #X = 0.
   X[X>1.0] = 1.0
   X[X<0.0] = 0.0
   d = (c0*X*X+(a0*numpy.power(pai,b0)-c0)*X)*hmx
   d[havg==0.] = 0.0
   dmac = (1+numpy.power(4.43,-1.0*pai)*(pai-1))*havg
   dmac[havg<3.53] = 0.0
   with numpy.errstate(divide='ignore', invalid='ignore'):
      dmachavg = numpy.true_divide(dmac,havg)
      zmac = havg*(1-(dmachavg))* \
         numpy.exp(-1.*numpy.power(0.5*(1.2/0.4/0.4)*(1-(dmachavg))*fai,-0.5))
      dmachavg[~ numpy.isfinite(dmachavg)] = 0
   zmac[havg<3.53] = 0.0
   a1 = 0.71
   b1 = 20.21
```

```
    c1 = -0.77
    with numpy.errstate(divide='ignore', invalid='ignore'):
       Y  = numpy.true_divide(pai*hst,havg)
       Y[ ~ numpy.isfinite(Y)]=0
    Y[Y<0.0] = 0.0
    z = zmac*(b1*Y*Y+c1*Y+a1)
    if z.any()>havg.any():
       z=0
    else:
       z=z
    #z[z>havg] = 0.0
    #Create geotiff
    sel          = gdal.Open(pdfile,gdal.GA_ReadOnly)
    proj         = sel.GetProjection()
    col         = sel.RasterXSize
    row         = sel.RasterYSize
    geogtransform = sel.GetGeoTransform()
    outfile      = outfile1
    outdriver    = gdal.GetDriverByName("GTiff")
    outdata      = outdriver.Create(outfile,col,row,1,gdal.GDT_Float32)
    outdata.GetRasterBand(1).WriteArray(d)
    outdata.SetGeoTransform(geogtransform)
    outdata.SetProjection(proj)
    outdata      = None
    outfile      = outfile2
    outdriver    = gdal.GetDriverByName("GTiff")
    outdata      = outdriver.Create(outfile,col,row,1,gdal.GDT_Float32)
    outdata.GetRasterBand(1).WriteArray(z)
    outdata.SetGeoTransform(geogtransform)
    outdata.SetProjection(proj)
    outdata      = None
    sel          = None
    return d,z

##### Case for SSP3, No-change/business-as-usual scenario (historical)
#GDP2014MER = 368917900000 #SSP3_BaU_NoCC
#GDP2014PPP = 909291900000 #SSP3_BaU_NoCC
#INDPOP2014 = 239870900 #SSP3_BaU_NoCC
GDP2050MER = 1122367000000 #SSP3_BaU_NoCC
GDP2050PPP = 2766358000000 #SSP3_BaU_NoCC
INDPOP2050 = 285081600 #SSP3_BaU_NoCC
directory = 'F:\\UrbanParam\\urban_para_WRF\\to_convert\\'
dir1    = 'F:\\UrbanParam\\'
```

```
#pop      =
   directory+'future_pop\\differ_historical\\Pop_predict_20-50.tif'
popviirs  = dir1+'historical_adj_2050.tif'
pdnl_2050 = dir1+'historical_adj_2050.tif'
nd         = gdal.Open(pdnl_2050,gdal.GA_ReadOnly)
band       = nd.GetRasterBand(1)
numCols    = nd.RasterXSize
numRows    = nd.RasterYSize

pai     = directory+'pai_lonlat_2050_new.tif'
fai     = directory+'fai_lonlat_2050_new.tif'
pai     = acquire(pai,numCols,numRows)
fai     = acquire(fai,numCols,numRows)

havg    = directory+'havg_lonlat_2050_new.tif'
havg    = acquire(havg,numCols,numRows)
hst       = 1.05*havg-3.7
hst[havg<3.53] = 0.
hmx       = 12.51*numpy.power(hst,0.77)

file_out1 = directory+'historical_d_2050_new2.tif'
file_out2 = directory+'historical_z0_2050_new2.tif'
d,z       = est_dz(popviirs,havg,pai,fai,hst,hmx,file_out1,file_out2)
```

A.3 Calculating future AHE

```
#This program is based upon by the results of Dong et al. (2017),
   Varquez et al. (2017)
#which reveals dependency of AHE to existing global datasets
#such as the LandScan and DMSP-OLS Nightlights
#VIIRS nightlights is used to substitute DMSP-OLS
#modified by Nisrina Setyo Darmanto using SSP data

import subprocess
import winsound
import arcpy
from arcpy import env
from arcpy.sa import *
import os
import numpy,glob
```

```
import time
try:
    from osgeo import gdal, osr
except ImportError:
    import gdal, osr
import matplotlib.mlab as mlab
import matplotlib.pyplot as plt
from scipy import stats
#import pandas

start = time.time()

def regres(x,y):
    x[x==0.] = numpy.nan

    if numpy.nansum(x) > 20:
        slope, intercept, r_value, p_value, std_err = \
      stats.linregress(x[~numpy.isnan(x)],y[~numpy.isnan(x)])
    else:
        slope = numpy.nan
        intercept = numpy.nan
        r_value = numpy.nan
        p_value = numpy.nan
        std_err = numpy.nan
    return slope, intercept, r_value, p_value, std_err

def adjust(x,y,R,uf,lf,a,b,thres,lowest_lim):
    x[numpy.logical_and(numpy.logical_and \
   (numpy.logical_or(R<lf,R>uf),y>thres),y>lowest_lim)] = \
   (y[numpy.logical_and(numpy.logical_and(numpy.logical_or(R<lf,R>uf),y>thres)
      \
   ,y>lowest_lim)]-b)/a
    return x

def full_adjustment(pop,nig,file_in,file_out):
    ## Necessary assumptions
    nig[pop<100.] = 0.
    nig[nig>0.01] = 0.
    llimit      = 0.0012

    store = numpy.copy(pop)
    work_pd = pop.flatten() # 1-d of pd within the admin
    work_nl = nig.flatten() # 1-d of nl within the admin
```

```
#print "Admin ID: ",iad," 1-d Size of Grids:",work_pd.shape
# get first regress line
print numpy.sum(work_pd),work_pd.shape,"sum"
print numpy.sum(work_nl),work_nl.shape,"night_sum"
slope1    =regres(work_pd,work_nl)[0]
intercept1 =regres(work_pd,work_nl)[1]
r_value1  =regres(work_pd,work_nl)[2]
if slope1==0:
    slope1=float('nan')
#print "ID:",iad
#print "slope1: ",slope1,"intercept1: ",intercept1,"r-squared1: ",
    r_value1**2

R = work_nl-work_pd*slope1-intercept1
print R[~numpy.isnan(R)]
if numpy.all(numpy.isnan(R)) == True:
    new_pop = numpy.copy(pop)
elif pop.shape[0]<3 and pop.shape[1]<3: #No change over very small
    administrative units
    new_pop = numpy.copy(pop)
else:
    # get upper fence and lower fence
    Q1   = numpy.percentile(R[~numpy.isnan(R)],25)
    Q3   = numpy.percentile(R[~numpy.isnan(R)],75)
    IQ   = Q3-Q1
    R_l  = Q1-1.5*IQ
    R_u  = Q3+1.5*IQ
    #print "ID:",iad, "lower fence:",R_l,"upper fence:",R_u
    # remove outlier
    work_pd_in = work_pd[numpy.logical_and(R>=R_l,R<=R_u)]
    work_nl_in = work_nl[numpy.logical_and(R>=R_l,R<=R_u)]
    nl_extra = work_nl[R>R_u]
    if nl_extra.shape[0]<10: ##Assumption
        thres = 0.0012
    else:
 #      print nl_extra.shape[0]
        thres = numpy.percentile(nl_extra,58.2887700535)
    #thres=600;
    #if iad==1215:
    #    print "Jakarta",thres

    # get second regress line after removing
    slope2    =regres(work_pd_in,work_nl_in)[0]
```

```
    intercept2 =regres(work_pd_in,work_nl_in)[1]
    r_value2  =regres(work_pd_in,work_nl_in)[2]
    if slope2==0:
        slope2=float('nan')

    del R
    R = nig-pop*slope1-intercept1
    if numpy.isnan(slope2):
        new_pop=numpy.copy(pop)
        #percentage=100
    else:
        new_pop =
            adjust(pop,nig,R,R_u,R_l,slope2,intercept2,thres,llimit)
        #percentage=len(work_pd_in)/len(work_pd[~numpy.isnan(work_pd)])*100

    del Q1,Q3,IQ,R_l,R_u

    #print "ID:",iad,"percentage of retained data=",percentage,"%"
    del work_pd_in, work_nl_in

# statistics about negative pd_new
#ng=len(pdnp1d[pdnp1d<0])
#total=len(pdnp1d[~numpy.isnan(pdnp1d)])
#print "negative pixel: ",ng
#print "total pixel of valid data:", total
#print "negative percentage:",ng/total*100,"%"
new_pop[new_pop<0]=0
new_pop[numpy.isnan(new_pop)]=0
### Assumption, no new_pop grid must exceed twice that of the
    original pop grid max.
#print numpy.nanmax(new_pop),numpy.nanmax(store)
new_pop[new_pop>2.5*numpy.nanmax(store)] =
    store[new_pop>2.5*numpy.nanmax(store)]
# create a new raster
sel         = gdal.Open(file_in,gdal.GA_ReadOnly)
proj        = sel.GetProjection()
col        = sel.RasterXSize
row        = sel.RasterYSize
geogtransform = sel.GetGeoTransform()
outfile     = file_out
outdriver   = gdal.GetDriverByName("GTiff")
outdata     = outdriver.Create(outfile,col,row,1,gdal.GDT_Float32)
outdata.GetRasterBand(1).WriteArray(new_pop)
```

```
    outdata.SetGeoTransform(geogtransform)
    outdata.SetProjection(proj)
    sel         = None
    outdata     = None

def clip_selection(xst,yst,xcol,yrow,file_in,file_out):
    driver = gdal.GetDriverByName('GTiff')
    filename = file_in
    output_file = file_out
    dataset = gdal.Open(filename,gdal.GA_ReadOnly)
    band    = dataset.GetRasterBand(1)
    cols    = dataset.RasterXSize
    rows    = dataset.RasterYSize
    transform= dataset.GetGeoTransform()

    xOrigin    = transform[0]
    yOrigin    = transform[3]
    pixelWidth = transform[1]
    pixelHeight = -transform[5]
    data = band.ReadAsArray(int(xst), int(yst), int(xcol), int(yrow))
    new_x = xOrigin + xst*pixelWidth
    new_y = yOrigin - yst*pixelHeight
    #data[data<=0] = numpy.nan
    new_transform = (new_x, transform[1], transform[2], new_y,
       transform[4], transform[5])
    dst_ds = driver.Create(output_file, xcol, yrow, 1, gdal.GDT_Float32)
       #writting output raster
    dst_ds.GetRasterBand(1).WriteArray(data)
    dst_ds.SetGeoTransform(new_transform)
    wkt = dataset.GetProjection()
    srs = osr.SpatialReference()
    srs.ImportFromWkt(wkt)
    dst_ds.SetProjection( srs.ExportToWkt() )
    del data
    dataset = None
    dst_ds = None

def acquire(fff,j,i,numCols,numRows):
    nd          = gdal.Open(fff,gdal.GA_ReadOnly)
    band        = nd.GetRasterBand(1)
    xsize        = numCols
    ysize        = numRows
    DATA        = band.ReadAsArray(j,i,xsize,ysize)
```

```
    nd          = None
    del band
    return DATA

def acquire_area(dts):
    xsize       = dts.RasterXSize
    ysize       = dts.RasterYSize
    DATA        = band.ReadAsArray(0,0,xsize,ysize)
    return DATA


directory1 = 'F:\\UrbanParam\\jakarta_futre_analyses\\urb\\'
directory2 = "F:\\UrbanParam\\future_pop\\differ_historical\\"
directory = "F:\\UrbanParam\\"
pp       = directory2+'Pop_predict_20-50.tif'
nl       = directory1+'VIIRS\\avg_jkt_viirs.tif'
dataset  = gdal.Open(pp,gdal.GA_ReadOnly)
band     = dataset.GetRasterBand(1)
cols     = dataset.RasterXSize
rows     = dataset.RasterYSize



#file_out = directory+'historical_adj_2050.tif'
#cor_ll_lon =
#cor_ll_lat =
#cor_ur_lon =
#cor_ur_lat =
#pop = acquire(pp,0,0,cols,rows)
#area= acquire_area(dataset)
#popden = pop/((0.008333333333*110.57)*(0.008333333333*111.32))
#niglit = acquire(nl,0,0,cols,rows)
#full_adjustment(popden,niglit,pp,file_out)

#popden_2050_noadj = popden
popadj     = directory+"historical_adj_2014.tif"
popden_adj  = acquire(popadj,0,0,cols,rows)
popden_adj =
    popden_adj/((0.008333333333*110.57)*(0.008333333333*111.32))

'''
#SSP3 data fujimori for whole Indonesia
energy_prim = 13.8199
```

```
energy_fin = 11.3701
ratio_loss = 1.000-(energy_fin/energy_prim)
fin_crt = 3.7426+2.6006
r_crt = fin_crt/energy_prim
fin_ia = 5.0269
r_ia = fin_ia/energy_prim
'''

#SSP3 2010 data fujimori for whole Indonesia
energy_prim = 7.6731
energy_fin = 6.4564
ratio_loss = 1.000-(energy_fin/energy_prim)
fin_crt = 2.8149+1.2753
r_crt = fin_crt/energy_prim
fin_ia = 2.3662
r_ia = fin_ia/energy_prim


#pop_2050 = 285.0816*1000000
pop_2010 = 239.8709*1000000
area_indo = 1917306.000000 #unit km2
unit = 1.0e18/(1000*1000*365*24*3600)

#calculating Q loss
Q_L = (energy_prim*ratio_loss/area_indo)*unit

#calculating Q CRT
#Q_CRT = q_crt()
#lspop_no_adj = numpy.array(popden)
lspop_adj = numpy.array(popden_adj)
#sum_lspop_no_adj = numpy.sum(lspop_no_adj)
sum_lspop_adj = numpy.sum(lspop_adj)
Q_CRT =
    (energy_prim*r_crt/((0.008333333333*110.57)*(0.008333333333*111.32)))
    \
   *unit*(sum_lspop_adj/pop_2010)*(lspop_adj/sum_lspop_adj)



#calculating Q IA
'''
land_cover_ssp3 = 133.6593*1000000/100
cropland_ssp3 = 29.9094*1000000/100
```

```
harvested_ssp = 3.4847*1000000/100
'''
land_cover_ssp3 = 133.6593*1000000/100
cropland_ssp3 = 26.6482*1000000/100
harvested_ssp = 2.856*1000000/100

land_cover_IA_ssp3 = cropland_ssp3+harvested_ssp #in km2


Q_IA_ssp = (energy_prim*r_ia/land_cover_IA_ssp3)*unit
#Q_IA_landscan = Q_IA_ssp*'''#luas area landscan
    PD'''/land_cover_IA_ssp3
Q_IA_grid = numpy.zeros([rows,cols])
for i in range(0,rows-1):
   for j in range(0,cols-1):
      if lspop_adj[i,j]>0:
         Q_IA_grid[i,j] = (Q_IA_ssp*((0.008333333333*110.57)* \
         (0.008333333333*111.32))/land_cover_IA_ssp3)
      else:
         Q_IA_grid[i,j] = 0

AHE_grid = Q_CRT+Q_IA_ssp
AHE_grid = numpy.array(AHE_grid)+Q_L

file_out2    = directory+'AHE_historical_adj_2014.tif'
#sel2         = gdal.Open(popden_adj,gdal.GA_ReadOnly)
proj2        = dataset.GetProjection()
#col         = sel.RasterXSize
#row         = sel.RasterYSize
geogtransform2 = dataset.GetGeoTransform()
outdriver2   = gdal.GetDriverByName("GTiff")
outdata2     = outdriver2.Create(file_out2,cols,rows,1,gdal.GDT_Float32)
outdata2.GetRasterBand(1).WriteArray(AHE_grid)
outdata2.SetGeoTransform(geogtransform2)
outdata2.SetProjection(proj2)
#sel         = None
outdata2     = None

end = time.time()
print "Time duration (sec.): ",(end-start)
raw_input("Press enter to continue..")
```

```
from __future__ import division
import arcpy,numpy,time
from arcpy import env
from arcpy.sa import *

# Check out extension license
arcpy.CheckOutExtension("Spatial")

directory1 = "F:\\AHE\\Temperature"
arcpy.env.workspace=(r'%s' % (directory))

Tyr = Raster("temp_yravg.tif")
Tyr_jkt = arcpy
list_tempmonth=arcpy.ListRasters("*temp_mask.tif")
dmn_boundary = "F:\\AHE\\Population\\domain_boundary.shp"
ahe_anl = Raster("F:\\AHE\\Population\\AHE_historical_adj_2050_2.tif")

start = time.time()

for temp1 in list_tempmonth:
    temp = Raster(temp1)
    outras1 = Con(((Tyr<=9.0) & (temp >16.0) ), 0.0027, \
   Con(((Tyr<=9.0) & (temp<=16.0)),0.03, \
      Con(((Tyr>9.0) & (Tyr<=20.0) & (temp>16.0)),
          (0.0239*Tyr*Tyr-0.404*Tyr+1.9741)/100, \
      Con(((Tyr>9.0) & (Tyr<=20.0) &
          (temp<=16.0)),(-0.0194*Tyr*Tyr+0.03368*Tyr+1.5172)/100, \
      Con(((Tyr>20) &
          (temp>16)),0.03,Con(((Tyr>20.0)&(temp<=16.0)),0.0027))))))
    outras2=Abs(temp - 16.)*outras1+1
    outras2.save(temp1+"_ratio.tif")
    del temp,outras1,outras2

meanratio = (Raster("aprtemp_mask.tif_ratio.tif")+\
           +Raster("augtemp_mask.tif_ratio.tif")+\
           +Raster("dectemp_mask.tif_ratio.tif")+\
           +Raster("febtemp_mask.tif_ratio.tif")+\
           +Raster("jantemp_mask.tif_ratio.tif")+\
           +Raster("jultemp_mask.tif_ratio.tif")+\
           +Raster("juntemp_mask.tif_ratio.tif")+\
```

```
            +Raster("martemp_mask.tif_ratio.tif")+\
            +Raster("maytemp_mask.tif_ratio.tif")+\
            +Raster("novtemp_mask.tif_ratio.tif")+\
            +Raster("octtemp_mask.tif_ratio.tif")+\
            +Raster("septemp_mask.tif_ratio.tif"))/12

for temp1 in list_tempmonth:
    name = temp1.replace("temp_mask.tif","")
    temp = Raster(temp1)
    sense = Con(((Tyr<=9.0) & (temp >16.0) ), 0.0027,
      Con(((Tyr<=9.0) & (temp<=16.0)),0.03, \
      Con(((Tyr>9.0) & (Tyr<=20.0) & (temp>16.0)),
          (0.0239*Tyr*Tyr-0.404*Tyr+1.9741)/100, \
      Con(((Tyr>9.0) & (Tyr<=20.0) &
          (temp<=16.0)),(-0.0194*Tyr*Tyr+0.03368*Tyr+1.5172)/100, \
      Con(((Tyr>20) &
          (temp>16)),0.03,Con(((Tyr>20.0)&(temp<=16.0)),0.0027))))))
    ratio = Abs(temp - 16.)*sense+1
    weigh = ratio/meanratio
    ahe_mon = ahe_anl*weigh
    ahe_mon.save("G:/AHEv2/"+name+"_ahe.tif")
    del name,temp,sense,ratio,weigh,ahe_mon

end = time.time()
print "Time duration (sec.): ",(end-start)

raw_input("Press enter to continue..")
```

A.5 Calculating future AHE: hourly value

```
from __future__ import division
import arcpy,numpy,time
from arcpy import env
from arcpy.sa import *

arcpy.CheckOutExtension("Spatial")

directory = "F:/AHE/Temperature/jakarta_temp"
arcpy.env.workspace=(r'%s' % (directory))
popden1 = Raster("F:/UrbanParam/historical_adj_2050.tif")#/1000000
popden  =
```

```
    (popden1/((0.008333333333*110.57)*(0.008333333333*111.32)))/1000000
#popden_adj/((0.008333333333*110.57)*(0.008333333333*111.32))
start = time.time()

list_tempmonth=arcpy.ListRasters("*temp_mask_jkt.tif")
for temp1 in list_tempmonth:
    name = temp1.replace("temp_mask_jkt.tif","")
    temp = Raster(temp1)
    ahe  = Raster("F:/UrbanParam/AHE_jakarta/"+name+"_2050_ahe.tif")

    outras0 = ahe * Con((temp<=12.4),0.608215,Con(((temp > 12.4) &
        (temp <=16.95)),0.557478, \
      Con(((temp > 16.95) & (temp <=
          20.95)),0.508126,Con((temp>20.95),0.438995)))) + popden * 84
    outras1 = ahe * Con((temp<=12.4),0.434346,Con(((temp > 12.4) &
        (temp <=16.95)),0.39479, \
      Con(((temp > 16.95) & (temp <=
          20.95)),0.370016,Con((temp>20.95),0.338244)))) + popden * 70
    outras2 = ahe * Con((temp<=12.4),0.289504,Con(((temp > 12.4) &
        (temp <=16.95)),0.336615, \
      Con(((temp > 16.95) & (temp <=
          20.95)),0.343788,Con((temp>20.95),0.315746)))) + popden * 70
    outras3 = ahe * Con((temp<=12.4),0.259544,Con(((temp > 12.4) &
        (temp <=16.95)),0.293129, \
      Con(((temp > 16.95) & (temp <=
          20.95)),0.294209,Con((temp>20.95),0.26177)))) + popden * 70
    outras4 = ahe * Con((temp<=12.4),0.294717,Con(((temp > 12.4) &
        (temp <=16.95)),0.34431, \
      Con(((temp > 16.95) & (temp <=
          20.95)),0.352713,Con((temp>20.95),0.312785)))) + popden * 70
    outras5 = ahe * Con((temp<=12.4),0.337675,Con(((temp > 12.4) &
        (temp <=16.95)),0.405552, \
      Con(((temp > 16.95) & (temp <=
          20.95)),0.418111,Con((temp>20.95),0.357215)))) + popden * 70
    outras6 = ahe * Con((temp<=12.4),0.45107,Con(((temp > 12.4) & (temp
        <=16.95)), \
      0.566222,Con(((temp > 16.95) & (temp <=
          20.95)),0.591728,Con((temp>20.95),0.499174)))) + popden * 84
    outras7 = ahe * Con((temp<=12.4),0.804371,Con(((temp > 12.4) &
        (temp <=16.95)),0.861609, \
      Con(((temp > 16.95) & (temp <=
          20.95)),0.849874,Con((temp>20.95),0.709469)))) + popden * 105
    outras8 = ahe * Con((temp<=12.4),1.411348,Con(((temp > 12.4) &
```

```
    (temp <=16.95)),1.13571, \
  Con(((temp > 16.95) & (temp <=
      20.95)),0.954737,Con((temp>20.95),0.840674)))) + popden * 122.5
outras9 = ahe * Con((temp<=12.4),1.316703,Con(((temp > 12.4) &
    (temp <=16.95)),1.188195, \
  Con(((temp > 16.95) & (temp <=
      20.95)),1.1498,Con((temp>20.95),1.178221)))) + popden * 140
outras10 = ahe * Con((temp<=12.4),1.355483,Con(((temp > 12.4) &
    (temp <=16.95)),1.386827, \
  Con(((temp > 16.95) & (temp <=
      20.95)),1.430585,Con((temp>20.95),1.53088)))) + popden * 140
outras11 = ahe * Con((temp<=12.4),1.323806,Con(((temp > 12.4) &
    (temp <=16.95)),1.392018, \
  Con(((temp > 16.95) & (temp <=
      20.95)),1.463298,Con((temp>20.95),1.587226)))) + popden * 140
outras12 = ahe * Con((temp<=12.4),1.314536,Con(((temp > 12.4) &
    (temp <=16.95)),1.408568, \
  Con(((temp > 16.95) & (temp <=
      20.95)),1.481697,Con((temp>20.95),1.593552)))) + popden * 140
outras13 = ahe * Con((temp<=12.4),1.29899,Con(((temp > 12.4) &
    (temp <=16.95)),1.38327, \
  Con(((temp > 16.95) & (temp <=
      20.95)),1.461458,Con((temp>20.95),1.584948)))) + popden * 140
outras14 = ahe * Con((temp<=12.4),1.328093,Con(((temp > 12.4) &
    (temp <=16.95)),1.403093, \
  Con(((temp > 16.95) & (temp <=
      20.95)),1.47728,Con((temp>20.95),1.604017)))) + popden * 140
outras15 = ahe * Con((temp<=12.4),1.307997,Con(((temp > 12.4) &
    (temp <=16.95)),1.428007, \
  Con(((temp > 16.95) & (temp <=
      20.95)),1.519798,Con((temp>20.95),1.646218)))) + popden * 140
outras16 = ahe * Con((temp<=12.4),1.30695,Con(((temp > 12.4) &
    (temp <=16.95)),1.430827, \
  Con(((temp > 16.95) & (temp <=
      20.95)),1.523604,Con((temp>20.95),1.654345)))) + popden * 140
outras17 = ahe * Con((temp<=12.4),1.393122,Con(((temp > 12.4) &
    (temp <=16.95)),1.450605, \
  Con(((temp > 16.95) & (temp <=
      20.95)),1.528128,Con((temp>20.95),1.646944)))) + popden * 140
outras18 = ahe * Con((temp<=12.4),1.463495,Con(((temp > 12.4) &
    (temp <=16.95)),1.485231, \
  Con(((temp > 16.95) & (temp <=
      20.95)),1.532506,Con((temp>20.95),1.581719)))) + popden * 140
```

```
outras19 = ahe * Con((temp<=12.4),1.433388,Con(((temp > 12.4) &
    (temp <=16.95)),1.398923, \
  Con(((temp > 16.95) & (temp <=
      20.95)),1.345529,Con((temp>20.95),1.290567)))) + popden * 140
outras20 = ahe * Con((temp<=12.4),1.19949,Con(((temp > 12.4) &
    (temp <=16.95)),1.149193, \
  Con(((temp > 16.95) & (temp <=
      20.95)),1.08802,Con((temp>20.95),0.996295)))) + popden * 140
outras21 = ahe * Con((temp<=12.4),1.210262,Con(((temp > 12.4) &
    (temp <=16.95)),1.086298, \
  Con(((temp > 16.95) & (temp <=
      20.95)),0.982672,Con((temp>20.95),0.875675)))) + popden * 140
outras22 = ahe * Con((temp<=12.4),0.992553,Con(((temp > 12.4) &
    (temp <=16.95)),0.816803, \
  Con(((temp > 16.95) & (temp <=
      20.95)),0.725456,Con((temp>20.95),0.636464)))) + popden * 122.5
outras23 = ahe * Con((temp<=12.4),0.8647332,Con(((temp > 12.4) &
    (temp <=16.95)),0.696604, \
  Con(((temp > 16.95) & (temp <=
      20.95)),0.60609,Con((temp>20.95),0.521858)))) + popden * 105

print "WARNING: Currently Building AHE ",name," by Yue"
outras0.save("F:/UrbanParam/AHE_jakarta_new/"+name+"_2050_ahe_00.tif")
outras1.save("F:/UrbanParam/AHE_jakarta_new/"+name+"_2050_ahe_01.tif")
outras2.save("F:/UrbanParam/AHE_jakarta_new/"+name+"_2050_ahe_02.tif")
outras3.save("F:/UrbanParam/AHE_jakarta_new/"+name+"_2050_ahe_03.tif")
outras4.save("F:/UrbanParam/AHE_jakarta_new/"+name+"_2050_ahe_04.tif")
outras5.save("F:/UrbanParam/AHE_jakarta_new/"+name+"_2050_ahe_05.tif")
outras6.save("F:/UrbanParam/AHE_jakarta_new/"+name+"_2050_ahe_06.tif")
outras7.save("F:/UrbanParam/AHE_jakarta_new/"+name+"_2050_ahe_07.tif")
outras8.save("F:/UrbanParam/AHE_jakarta_new/"+name+"_2050_ahe_08.tif")
outras9.save("F:/UrbanParam/AHE_jakarta_new/"+name+"_2050_ahe_09.tif")
outras10.save("F:/UrbanParam/AHE_jakarta_new/"+name+"_2050_ahe_10.tif")
outras11.save("F:/UrbanParam/AHE_jakarta_new/"+name+"_2050_ahe_11.tif")
outras12.save("F:/UrbanParam/AHE_jakarta_new/"+name+"_2050_ahe_12.tif")
outras13.save("F:/UrbanParam/AHE_jakarta_new/"+name+"_2050_ahe_13.tif")
outras14.save("F:/UrbanParam/AHE_jakarta_new/"+name+"_2050_ahe_14.tif")
outras15.save("F:/UrbanParam/AHE_jakarta_new/"+name+"_2050_ahe_15.tif")
outras16.save("F:/UrbanParam/AHE_jakarta_new/"+name+"_2050_ahe_16.tif")
outras17.save("F:/UrbanParam/AHE_jakarta_new/"+name+"_2050_ahe_17.tif")
outras18.save("F:/UrbanParam/AHE_jakarta_new/"+name+"_2050_ahe_18.tif")
outras19.save("F:/UrbanParam/AHE_jakarta_new/"+name+"_2050_ahe_19.tif")
outras20.save("F:/UrbanParam/AHE_jakarta_new/"+name+"_2050_ahe_20.tif")
```

```
    outras21.save("F:/UrbanParam/AHE_jakarta_new/"+name+"_2050_ahe_21.tif")
    outras22.save("F:/UrbanParam/AHE_jakarta_new/"+name+"_2050_ahe_22.tif")
    outras23.save("F:/UrbanParam/AHE_jakarta_new/"+name+"_2050_ahe_23.tif")

end = time.time()
print "Time duration (sec.): ",(end-start)

raw_input("Press enter to continue..")
```

B

Python programs for heat related mortality estimation

B.1 Bias adjustment (example for RCP8.5&BaU temperature bias adjustment)

```
#This program is to correct temperature from simulation to be similar
    with observation
#Current program is for RCP8.5\&BaU temperature bias adjustment case
#Program created by Nisrina Setyo Darmanto

import numpy as np
import pandas as pd
import scipy
import scipy.stats
from scipy.stats import norm
import matplotlib
import matplotlib.pyplot as plt
import matplotlib.mlab as mlab
from scipy.stats import linregress as ln
from netCDF4 import Dataset
import glob

def Fit(y):
   dist_results = []
   params = {}
   dist_names = ['norm']#,'expon','pareto', 'weibull_max']
```

```
    for dist_name in dist_names:
        dist = getattr(scipy.stats, dist_name)
        param = dist.fit(y)

        params[dist_name] = param
        #Applying the Kolmogorov-Smirnov test
        D, p = scipy.stats.kstest(y, dist_name, args=param);
        dist_results.append((dist_name,p))

    #select the best fitted distribution
    sel_dist,p = (max(dist_results,key=lambda item:item[1]))
    #store the name of the best fit and its p value
    DistributionName = sel_dist
    PValue = p

    #self.isFitted = True
    return DistributionName, PValue, params

def assign_norm(data_to_be_fit):
    data_fit     = Fit(data_to_be_fit)
    param_norm      = data_fit[2][data_fit[0]]
    pdf_data     = norm.pdf(data_to_be_fit, loc = param_norm[0], scale =
        param_norm[1])
    cdf_data     = pdf_data.cumsum()
    cdf_data /= cdf_data[-1]

    return param_norm, pdf_data, cdf_data

def fitting_to_obs(data_to_fit, locs, scales, delta):
    locs         = locs + delta
    scales          = scales
    pdf_fit         = norm.pdf(data_to_fit, loc=locs, scale = scales)
    cdf_fit         = pdf_fit.cumsum()
    cdf_fit /= cdf_fit[-1]

    list_ppf = []

    for item in xrange(cdf_fit.size):
        ppf_data = norm.ppf(cdf_fit[item], loc=locs, scale = scales)
        if ppf_data==float('Inf'):
            ppf_data = norm.ppf(cdf_fit[item-1], loc=locs, scale = scales)
            list_ppf.append(ppf_data)
```

```
      else:
        list_ppf.append(ppf_data)

   df_ppf = pd.DataFrame(list_ppf)

   return pdf_fit, cdf_fit, df_ppf
   del list_ppf

def find_nearest(array,value):
    idx = (np.abs(array-value)).argmin()
    return array[idx]

def temp_200(current_start, target_lon, target_lat,current_list):

   lons  = current_start.variables['XLONG'][:]
   lons1d  = lons[0,:]
   lats  = current_start.variables['XLAT'][:]
   lats1d  = lats[:,0]
   ilon = np.where(lons1d==find_nearest(lons1d,target_lon))[0][0]
      #x-coordinate
   jlat = np.where(lats1d==find_nearest(lats1d,target_lat))[0][0]
      #y-coordinate

   print len(current_list)

   single_file  =
      current_start.variables['T_200ZR_URB2D'][:,jlat,ilon]-273.15
   df = pd.DataFrame(single_file)

   for i in xrange(len(current_list)-1):
      list_file  = Dataset(current_list[i+1], mode = 'r')
      temp    = list_file.variables['T_200ZR_URB2D'][:,jlat,ilon]-273.15
      df2       = pd.DataFrame(temp)
      print i
      df_append  = df.append(df2)
      df = df_append
      del df2
      #temp_mat.append([temp_mat])

   #temp_10yrs = np.stack(temp_mat)
   #del temp_mat
   del df
   return df_append
```

```
folder    = 'F:/WRFResult/code/' #raw_input("input file folder: ")
filename1 = folder + 'df_TPR_temp200.csv' #raw_input('input file name:
    ')
filename2 = folder + 'df_CGK_temp200.csv'
filename3 = folder + 'df_KMY_temp200.csv'

df_tpr    = pd.read_csv(filename1)
df_cgk    = pd.read_csv(filename2)
df_kmy    = pd.read_csv(filename3)

data_obs_tpr  = df_tpr.iloc[:,1:11].values.ravel()
data_obs_cgk = df_cgk.iloc[:,1:11].values.ravel()
data_obs_kmy = df_kmy.iloc[:,1:11].values.ravel()

data_mod_tpr  = df_tpr.iloc[:,12:23].values.ravel()
data_mod_cgk = df_cgk.iloc[:,12:23].values.ravel()
data_mod_kmy = df_kmy.iloc[:,12:23].values.ravel()

#kasih condition if disini untuk value inside range 0-50.0, if no give
    null value


obs_ave = np.nanmean( np.array([data_obs_tpr, data_obs_cgk,
    data_obs_kmy]), axis=0 )
mod_ave = np.nanmean( np.array([data_mod_tpr, data_mod_cgk,
    data_mod_kmy]), axis=0 )

df_data_all =
    pd.DataFrame(columns=['index_orig','KMO_obs','KMO_mod','TPR_obs',
    'TPR_mod',
           'CGK_obs', 'CGK_mod', 'Ave_obs', 'Ave_mod'])

df_data_all['KMO_obs']   = data_obs_kmy
df_data_all['KMO_mod']  = data_mod_kmy
df_data_all['TPR_obs']   = data_obs_tpr
df_data_all['TPR_mod']   = data_mod_tpr
df_data_all['CGK_obs']   = data_obs_cgk
df_data_all['CGK_mod']   = data_mod_cgk
df_data_all['Ave_obs']   = obs_ave
df_data_all['Ave_mod']   = mod_ave
df_data_all['index_orig']  = np.array(df_data_all.index)
```

```
current_t200_list  =
    sorted(glob.glob('F:/WRFResult/tempor_curr/CURR_20*_variables_t200.nc'))
current_t200    =
    Dataset('F:/WRFResult/tempor_curr/CURR_2006_variables_t200.nc',
    mode = 'r')#['T_200ZR_URB2D'][:] - 273.15
cmpc_t200_list  =
    sorted(glob.glob('F:/WRFResult/tempor/CMPC_20*_variables_t200.nc'))
cmpc_t200       =
    Dataset('F:/WRFResult/tempor/CMPC_2006_variables_T200.nc', mode
    ='r')
hist_t200_list  =
    sorted(glob.glob('F:/WRFResult/tempor_hist/HIST_20*_variables_t200.nc'))
hist_t200       =
    Dataset('F:/WRFResult/tempor_hist/HIST_2006_variables_t200.nc',
    mode ='r')

#curr_fit    = Fit(curr_point)
#param_curr  = curr_fit[2][curr_fit[0]]
#print 'mean and sigma current: ', str(param_curr)

lon_TPR    = 106.8778
lat_TPR    = -6.11
lon_KMY      = 106.8333
lat_KMY      = -6.18333
lon_CGK      = 106.65
lat_CGK      = -6.1167


KMO_hist     = temp_200(hist_t200, lon_KMY, lat_KMY, hist_t200_list)
df_KMO_hist  = KMO_hist
TPR_hist     = temp_200(hist_t200, lon_TPR, lat_TPR, hist_t200_list)
df_TPR_hist  = TPR_hist
CGK_hist     = temp_200(hist_t200, lon_CGK, lat_CGK, hist_t200_list)
df_CGK_hist  = CGK_hist

#normal distribution assigning to observed data
obs_KMO_mask    = df_data_all['KMO_obs'][df_data_all['KMO_obs']<40.0]
obs_TPR_mask    = df_data_all['TPR_obs'][df_data_all['TPR_obs']<40.0]
obs_CGK_mask    = df_data_all['CGK_obs'][df_data_all['CGK_obs']<40.0]

param_obs_KMO, obs_KMO_pdf, cdf_KMO_obs = assign_norm(obs_KMO_mask)
param_obs_TPR, obs_TPR_pdf, cdf_TPR_obs = assign_norm(obs_TPR_mask)
param_obs_CGK, obs_CGK_pdf, cdf_CGK_obs = assign_norm(obs_CGK_mask)
```

```
param_mean_OBSAve = np.mean(
             np.array(
             [param_obs_KMO[0],
             param_obs_TPR[0],
             param_obs_CGK[0]
             ]
             )
             )

param_std_OBSAve = np.mean(
             np.array(
             [param_obs_KMO[1],
             param_obs_TPR[1],
             param_obs_CGK[1]
             ]
             )
             )

param_mod_KMO, mod_KMO_pdf, mod_KMO_cdf =
    assign_norm(df_data_all['KMO_mod'])
param_mod_TPR, mod_TPR_pdf, mod_TPR_cdf =
    assign_norm(df_data_all['TPR_mod'])
param_mod_CGK, mod_CGK_pdf, mod_CGK_cdf =
    assign_norm(df_data_all['CGK_mod'])

param_mean_MODAve = np.mean(
             np.array(
             [param_mod_KMO[0],
             param_mod_TPR[0],
             param_mod_CGK[0]
             ]
             )
             )

param_std_MODAve = np.mean(
             np.array(
             [param_mod_KMO[1],
             param_mod_TPR[1],
             param_mod_CGK[1]
             ]
             )
             )
```

```
param_hist_KMO, hist_KMO_pdf, hist_KMO_cdf = assign_norm(df_KMO_hist)
param_hist_TPR, hist_TPR_pdf, hist_TPR_cdf = assign_norm(df_TPR_hist)
param_hist_CGK, hist_CGK_pdf, hist_CGK_cdf = assign_norm(df_CGK_hist)

param_mean_HISTAve = np.mean(
             np.array(
             [param_hist_KMO[0],
             param_hist_TPR[0],
             param_hist_CGK[0]
             ]
             )
             )

param_std_HISTAve = np.mean(
             np.array(
             [param_hist_KMO[1],
             param_hist_TPR[1],
             param_hist_CGK[1]
             ]
             )
             )

index_modKMO    = sorted(enumerate(df_data_all['KMO_mod']),key=lambda
    i:i[1])
df_indexKMO     = pd.DataFrame(index_modKMO)
index_modTPR    = sorted(enumerate(df_data_all['TPR_mod']),key=lambda
    i:i[1])
df_indexTPR     = pd.DataFrame(index_modTPR)
index_modCGK    = sorted(enumerate(df_data_all['CGK_mod']),key=lambda
    i:i[1])
df_indexCGK     = pd.DataFrame(index_modCGK)

index_histKMO   = sorted(enumerate(df_KMO_hist[0]),key=lambda i:i[1])
df_index_hist_KMO = pd.DataFrame(index_histKMO)
index_histTPR   = sorted(enumerate(df_TPR_hist[0]),key=lambda i:i[1])
df_index_hist_TPR = pd.DataFrame(index_histTPR)
index_histCGK   = sorted(enumerate(df_CGK_hist[0]),key=lambda i:i[1])
df_index_hist_CGK = pd.DataFrame(index_histCGK)


#======================Normal Correction
    Parameters=========================#
```

```
stdCOR_hist_KMO  = (param_obs_KMO[1] / param_mod_KMO[1]) *
    param_hist_KMO[1]
meanCOR_hist_KMO  = param_obs_KMO[0] + ( (param_obs_KMO[1] /
    param_mod_KMO[1]) * (param_hist_KMO[0] - param_mod_KMO[0]))

stdCOR_hist_TPR  = (param_obs_TPR[1] / param_mod_TPR[1]) *
    param_hist_TPR[1]
meanCOR_hist_TPR  = param_obs_TPR[0] + ( (param_obs_TPR[1] /
    param_mod_TPR[1]) * (param_hist_TPR[0] - param_mod_TPR[0]))

stdCOR_hist_CGK  = (param_obs_CGK[1] / param_mod_CGK[1]) *
    param_hist_CGK[1]
meanCOR_hist_CGK  = param_obs_CGK[0] + ( (param_obs_CGK[1] /
    param_mod_CGK[1]) * (param_hist_CGK[0] - param_mod_CGK[0]))

#====================FITTING TO CORRECTED MEAN AND
    STD=======================#

mod_KMO_pdf_fit, cdf_KMO_mod_fit, ppf_KMO_mod_fit = fitting_to_obs(
                        df_KMO_hist[0],
                        locs = meanCOR_hist_KMO,
                        scales = stdCOR_hist_KMO,
                        delta = 0)

mod_TPR_pdf_fit, cdf_TPR_mod_fit, ppf_TPR_mod_fit = fitting_to_obs(
                        df_TPR_hist[0],
                        locs = meanCOR_hist_TPR,
                        scales = stdCOR_hist_TPR,
                        delta = 0)

mod_CGK_pdf_fit, cdf_CGK_mod_fit, ppf_CGK_mod_fit = fitting_to_obs(
                        df_CGK_hist[0],
                        locs = meanCOR_hist_CGK,
                        scales = stdCOR_hist_CGK,
                        delta = 0)



#======================RETURN FUNCTION==================#
df_combine = pd.DataFrame(columns=['index_orig', 'data_mod','cdf_mod',
    'ppf_mod'])
df_combine['index_orig'] = pd.concat([df_index_hist_KMO[0]])
```

```
df_combine['data_mod'] = pd.concat([df_index_hist_KMO[1]])
a = pd.DataFrame(mod_KMO_pdf_fit)
b = pd.DataFrame(ppf_KMO_mod_fit)
df_combine['cdf_mod'] = pd.concat([a])
df_combine['ppf_mod'] = pd.concat([b])

slopeKMO, interceptKMO, r_valueKMO, p_valueKMO, std_errKMO =
    ln(df_combine['data_mod'], df_combine['ppf_mod']) #orig, ppf

orig = df_KMO_hist[0]
tf_fun_KMO = slopeKMO*orig + interceptKMO

param_TF_KMO_cmpc, mod_KMO_pdf_TF_cmpc, mod_KMO_cdf_TF_cmpc =
    assign_norm(tf_fun_KMO)


del df_combine
df_combine = pd.DataFrame(columns=['index_orig', 'data_mod','cdf_mod',
    'ppf_mod'])
df_combine['index_orig'] = pd.concat([df_index_hist_TPR[0]])
df_combine['data_mod'] = pd.concat([df_index_hist_TPR[1]])
a = pd.DataFrame(mod_TPR_pdf_fit)
b = pd.DataFrame(ppf_TPR_mod_fit)
df_combine['cdf_mod'] = pd.concat([a])
df_combine['ppf_mod'] = pd.concat([b])

slopeTPR, interceptTPR, r_valueTPR, p_valueTPR, std_errTPR =
    ln(df_combine['data_mod'], df_combine['ppf_mod']) #orig, ppf

orig = df_TPR_hist[0]
tf_fun_TPR = slopeTPR*orig + interceptTPR

param_TF_TPR, mod_TPR_pdf_TF, mod_TPR_cdf_TF = assign_norm(tf_fun_TPR)

del df_combine
df_combine = pd.DataFrame(columns=['index_orig', 'data_mod','cdf_mod',
    'ppf_mod'])
df_combine['index_orig'] = pd.concat([df_index_hist_CGK[0]])
df_combine['data_mod'] = pd.concat([df_index_hist_CGK[1]])
a = pd.DataFrame(mod_CGK_pdf_fit)
b = pd.DataFrame(ppf_CGK_mod_fit)
df_combine['cdf_mod'] = pd.concat([a])
df_combine['ppf_mod'] = pd.concat([b])
```

```
slopeCGK, interceptCGK, r_valueCGK, p_valueCGK, std_errCGK =
    ln(df_combine['data_mod'], df_combine['ppf_mod']) #orig, ppf

orig = df_CGK_hist[0]
tf_fun_CGK = slopeCGK*orig + interceptCGK

param_TF_CGK, mod_CGK_pdf_TF, mod_CGK_cdf_TF = assign_norm(tf_fun_CGK)

average_slope_hist = np.mean(np.array([slopeKMO, slopeTPR, slopeCGK]))
print 'slope BaU: ', str(average_slope_hist)
average_intercept_hist = np.mean(np.array([interceptKMO, interceptTPR,
    interceptCGK]))
print 'intercept BaU: ', str(average_intercept_hist)
```

B.2 Estimating optimum temperature from daily maximum and minimum temperature from synop data

```
#This program is to estimate optimum temperature from daily maximum and
    minimum temperature from synop data
#Program created by Nisrina Setyo Darmanto

import numpy as np
import glob
import pandas as pd
from netCDF4 import Dataset
import numpy as np
import matplotlib
import matplotlib.pyplot as plt
from mpl_toolkits.basemap import Basemap
import os.path
from matplotlib.font_manager import FontProperties
from matplotlib import rcParams
import matplotlib.pylab as pylab
params = {'legend.fontsize': 'large',
          'axes.labelsize': 'large',
         'axes.titlesize':'large',
         'xtick.labelsize':'large',
         'ytick.labelsize':'large'}
pylab.rcParams.update(params)
```

```
import glob

try:
    import archook #The module which locates arcgis
    archook.get_arcpy()
    import arcpy
except ImportError:
    print 'error on importing arcpy'
from arcpy import env
from arcpy.sa import *

import os
import numpy,glob
import time
try:
    from osgeo import gdal, osr
except ImportError:
    import gdal, osr
import seaborn as sns

#import pandas

def acquire(fff,j,i,numCols,numRows):
    nd          = gdal.Open(fff,gdal.GA_ReadOnly)
    band        = nd.GetRasterBand(1)
    xsize        = numCols
    ysize        = numRows
    DATA        = band.ReadAsArray(j,i,xsize,ysize)
    nd          = None
    del band
    return DATA

def acquire_area(dts):
    xsize       = dts.RasterXSize
    ysize       = dts.RasterYSize
    DATA        = band.ReadAsArray(0,0,xsize,ysize)
    return DATA

def percentile84(file_list):
   dfList = pd.DataFrame([])

   for num_file in xrange(len(file_list)):
```

```
      filename = file_list[num_file]
      testlist = open(filename).readlines()

      print len(testlist)

      matches = [s for s in testlist if '333 10' in s]

      for i in xrange(len(matches)):
         lines      = matches[i]
         stnames    = lines[0:5]
         year     = float(lines[6:10])
         month    = float(lines[11:13])
         day        = float(lines[14:16])
         hour     = float(lines[17:19])

         index_333  = lines.find('333 10')

         tmax     = lines[index_333+6 : index_333+10]
         tmax     = float(tmax) / 10.0

         data1 = pd.DataFrame([stnames,year,month,day,hour,tmax])
         data1 = data1.transpose()
         dfList = dfList.append(data1, ignore_index=True)

         print stnames,year,month,day,hour,tmax

   dfList = dfList.rename(columns= {0:'station', 1: 'year', 2: 'month',
       3:'day', 4:'hour', 5:'tmax'})

   tmax_array  = dfList['tmax']
   topt_obs = np.percentile(tmax_array, 60.0)
   return topt_obs, tmax_array, dfList

def percentile84_mean(file_list):
   dfList = pd.DataFrame([])

   for num_file in xrange(len(file_list)):
      filename = file_list[num_file]
      testlist = open(filename).readlines()

      print len(testlist)

      matches = [s for s in testlist if 'NIL=' not in s]
```

```
    for i in xrange(len(matches)):
      lines      = matches[i]
      stnames    = lines[0:5]
      year     = float(lines[6:10])
      month    = float(lines[11:13])
      day        = float(lines[14:16])
      hour     = float(lines[17:19])

      print lines[54:57]

      myString = lines[54:57]
      print lines[54:57]
      if not myString:
        tmean = 9999
      else:
        tmean    = float(lines[54:57])/10.0

      index_333  = lines.find('333 10')

      if index_333 == float(-1):
        tmax = 9999
      else:
        tmax     = lines[index_333+6 : index_333+10]
        tmax     = float(tmax) / 10.0

      data1 = pd.DataFrame([stnames,year,month,day,hour,tmax,tmean])
      data1 = data1.transpose()
      dfList = dfList.append(data1, ignore_index=True)

      print stnames,year,month,day,hour,tmax,tmean

  dfList = dfList.rename(columns= {0:'station', 1: 'year', 2: 'month',
     3:'day', 4:'hour', 5:'tmax',6:'tmean'})

  tmax_array  = dfList['tmax']
  topt_obs = np.percentile(tmax_array, 60.0)

  tmean_array  = dfList['tmean']
  tmean_opt_obs = np.percentile(tmean_array, 60.0)
  return topt_obs, tmean_opt_obs, tmax_array, dfList, tmean_array

def plot_map(lon, lat, parameter, vmin, vmax, figname):
```

```
    current  = Dataset('../tempor_curr/CURR_dayMEAN_mean.nc', mode = 'r')
    lon1    = lon.min()
    lon2    = lon.max()
    lat1    = lat.min()
    lat2    = lat.max()
    x_grid     = np.size(current.dimensions['x'])
    y_grid     = np.size(current.dimensions['y'])

    del current

    m = Basemap(projection='mill',llcrnrlat=lat1,urcrnrlat=lat2,\
    llcrnrlon=lon1,urcrnrlon=lon2,lat_ts=None,resolution ='h')
    fig,ax       = plt.subplots()
    m.drawcoastlines()
    parallels    = np.arange(-10.,-4.,0.25)
    m.drawparallels(parallels, labels=[1,0,0,0], fontsize=10)
    meridians    = np.arange(104., 108., 0.25)
    m.drawmeridians(meridians, labels=[0,0,0,1])#, fontsize=10)
    xi,yi      = m(lon,lat)
    #plt.savefig(figname+'.png')

    cs         = plt.pcolormesh(xi,yi,parameter, cmap='jet',
        shading='gouraud', vmin= vmin, vmax=vmax)
    cs.cmap.set_under('w')
    cbar   = m.colorbar(cs, location='right',extend='max')
    plt.title(figname)
    plt.savefig('../mortality_image/'+figname+'.png')
    plt.close()


def output_tmax(file_list):

    all_year_tmax = []

    for file_num in xrange(len(file_list)):
       current = Dataset(file_list[file_num], mode =
           'r')['T_200ZR_URB2D'][:] - 273.15
       all_year_tmax.append(current)

    tmax_all = np.stack(all_year_tmax)
    del all_year_tmax

    return tmax_all
```

```
directory1 = '../ogimet_96741/'
file_list = sorted(glob.glob(directory1 + '20*.txt'))
pr84_tpr = percentile84(file_list)
data_tpr = pr84_tpr[1]
df_tpr    = pr84_tpr[2]

directory2 = '../ogimet_96745/'
file_list2 = sorted(glob.glob(directory2 + '20*.txt'))
pr84_kmy = percentile84(file_list2)
data_kmy = pr84_kmy[1]
df_kmy    = pr84_kmy[2]

topt_obs = (pr84_kmy[0] + pr84_tpr[0])/2

fig, ax = plt.subplots()
a = df_tpr['tmax']
b = pd.to_numeric(a)
b = b[b < 40.0]
n, bins, patch = ax.hist(b, 20, label='Jakarta obs. Tmax 2006-2015')
ax.legend(loc ='best')
plt.savefig('../mortality_image/data_tmax_hist.png')
plt.close()

del b, df_kmy, df_tpr

#=================================================#
#FOR CALCULATING OT BASED ON MEAN DAILY TEMPERATURE#
# comment out when calculating OT based on Td_max
#=================================================#
'''
directory1 = '../ogimet_96741/'
file_list = sorted(glob.glob(directory1 + '20*.txt'))
pr84_tpr = percentile84_mean(file_list)
data_tpr = pr84_tpr[1]
df_tpr    = pr84_tpr[3]

directory2 = '../ogimet_96745/'
file_list2 = sorted(glob.glob(directory2 + '20*.txt'))
pr84_kmy = percentile84_mean(file_list2)
data_kmy = pr84_kmy[1]
df_kmy    = pr84_kmy[3]
```

```
topt_obs     = (pr84_kmy[0] + pr84_tpr[0])/2
tmean_opt_obs  = (pr84_kmy[1] + pr84_tpr[1])/2

fig, ax = plt.subplots()
a = df_tpr['tmax']
b = pd.to_numeric(a)
b = b[b < 40.0]
b = b[b > 10.0]
n1, bins1, patch1 = ax.hist(b, 20, label='Jakarta obs. Tmax 2006-2015')
ax.legend(loc ='best')
plt.savefig('../mortality_image/data_tmax_hist_181102.png')
plt.close()

del b


a = df_tpr['tmean']
b = pd.to_numeric(a)
b = b[b < 40.0]
b = b[b > 10.0]
list1 = b
del b
n = 8
list2 = [np.mean(list1[i:i+n]) for i in range(0,len(list1),n)]
b = list2
fig, ax = plt.subplots()
n2, bins2, patch2 = ax.hist(b, 20, label='Jakarta obs. Tmean 2006-2015')
ax.legend(loc ='best')
plt.savefig('../mortality_image/data_tmean_hist_181102.png')
plt.close()

del b, #df_kmy, df_tpr

tmean_opt_obs = np.percentile(pr84_tpr[3], 60.0)
'''
```

B.3 Calculating future heat-related mortality risk in RCP2.6& Compact and RCP8.5&BaU

```
#This program is to estimate future heat-related mortality risk in
    RCP2.6\&Compact and RCP8.5\&BaU
#Any required input is result from previous program
#Program created by Nisrina Setyo Darmanto

import numpy as np
import glob
import pandas as pd
from netCDF4 import Dataset
import numpy as np
import matplotlib
import matplotlib.pyplot as plt
from mpl_toolkits.basemap import Basemap
import os.path
from matplotlib.font_manager import FontProperties
from matplotlib import rcParams
import matplotlib.pylab as pylab
params = {'legend.fontsize': 'large',
          'axes.labelsize': 'large',
         'axes.titlesize':'large',
         'xtick.labelsize':'large',
         'ytick.labelsize':'large'}
pylab.rcParams.update(params)

import glob

try:
    import archook #The module which locates arcgis
    archook.get_arcpy()
    import arcpy
except ImportError:
    print 'error on importing arcpy'
from arcpy import env
from arcpy.sa import *

import os
import numpy,glob
import time
try:
    from osgeo import gdal, osr
except ImportError:
    import gdal, osr
import seaborn as sns
```

```
#import pandas

def acquire(fff,j,i,numCols,numRows):
    nd          = gdal.Open(fff,gdal.GA_ReadOnly)
    band        = nd.GetRasterBand(1)
    xsize        = numCols
    ysize        = numRows
    DATA        = band.ReadAsArray(j,i,xsize,ysize)
    nd          = None
    del band
    return DATA

def acquire_area(dts):
    xsize       = dts.RasterXSize
    ysize       = dts.RasterYSize
    DATA        = band.ReadAsArray(0,0,xsize,ysize)
    return DATA


def plot_map(lon, lat, parameter, vmin, vmax, figname):
   current  = Dataset('../tempor_curr/CURR_dayMEAN_mean.nc', mode = 'r')
   lon1    = lon.min()
   lon2    = lon.max()
   lat1    = lat.min()
   lat2    = lat.max()
   x_grid     = np.size(current.dimensions['x'])
   y_grid     = np.size(current.dimensions['y'])

   del current

   m = Basemap(projection='mill',llcrnrlat=lat1,urcrnrlat=lat2,\
   llcrnrlon=lon1,urcrnrlon=lon2,lat_ts=None,resolution ='h')
   fig,ax       = plt.subplots()
   m.drawcoastlines()
   parallels    = np.arange(-10.,-4.,0.25)
   m.drawparallels(parallels, labels=[1,0,0,0], fontsize=10)
   meridians    = np.arange(104., 108., 0.25)
   m.drawmeridians(meridians, labels=[0,0,0,1])#, fontsize=10)
   xi,yi      = m(lon,lat)
   #plt.savefig(figname+'.png')

   cs         = plt.pcolormesh(xi,yi,parameter, cmap='jet',
```

```
        shading='gouraud', vmin= vmin, vmax=vmax)
    cs.cmap.set_under('w')
    cbar  = m.colorbar(cs, location='right',extend='max')
    plt.title(figname)
    plt.savefig('../mortality_image/'+figname+'.png')
    plt.close()


def output_tmax(file_list):

    all_year_tmax = []

    for file_num in xrange(len(file_list)):
        current = Dataset(file_list[file_num], mode =
            'r')['T_200ZR_URB2D'][:] - 273.15
        all_year_tmax.append(current)

    tmax_all = np.stack(all_year_tmax)
    del all_year_tmax

    return tmax_all



#=============================================#
#INPUT OF CLIMATE SIMULATION DATA#
#=============================================#
current  = Dataset('../tempor_curr/CURR_dayMEAN_mean.nc', mode = 'r')
lon     = current.variables['XLONG'][:]
lat       = current.variables['XLAT'][:]
lon1    = lon.min()
lon2    = lon.max()
lat1    = lat.min()
lat2    = lat.max()
x_grid    = np.size(current.dimensions['x'])
y_grid    = np.size(current.dimensions['y'])

del current

#=============================================#
#===INPUT POPULATION RASTER DATA==============#
#=============================================#
```

```
pop_cmpc_curr = '../Compact_SSP1/target_2014_cmpc.tif'
pop_cmpc_2050 = '../Compact_SSP1/target_2050_cmpc.tif'
pop_hist_curr = '../Historical_SSP3/target_2014_hist.tif'
pop_hist_2050 = '../Historical_SSP3/target_2050_hist.tif'
#test_data = acquire_area(file_temp,0,0,)

dataset    = gdal.Open(pop_cmpc_curr,gdal.GA_ReadOnly)
band       = dataset.GetRasterBand(1)
cols       = dataset.RasterXSize
rows       = dataset.RasterYSize

#CURRENT POPULATION
pdCMPC_curr  = acquire(pop_cmpc_curr, 0, 0, cols, rows)
arr_pdCMPC_curr = pdCMPC_curr[::-1]

#COMPACT POPULATION
pdCMPC_2050  = acquire(pop_cmpc_2050, 0, 0, cols, rows)
arr_pdCMPC_2050 = pdCMPC_2050[::-1]

#BAU POPULATION
pdHIST_2050  = acquire(pop_hist_2050, 0, 0, cols, rows)
arr_pdHIST_2050 = pdHIST_2050[::-1]

del pop_cmpc_curr, pop_cmpc_2050, pop_hist_curr, pop_hist_2050

#======================INPUT COEFFICIENT
    LIST================================#
cdr_day2014  = 0.0095/1000 #every 1000 population
cdr_day2050  = 0.0306/1000 #every 1000 population

pop_ratio65_2014 = 0.0269
pop_ratio65_2050 = 0.2203

cdr_65_2014 = cdr_day2014*pop_ratio65_2014
cdr_65_2050 = cdr_day2050*pop_ratio65_2050

function_coef_thai = 0.60
function_coef_jp = 0.88

#==============put bias corrected max temp
    here================================###

urbCurrent  =
```

```
    Dataset('../geo_em.d03_current.nc',mode='r')['MOD_FRC_URB2D'][:]
urbCurrent  = urbCurrent[0]

current_Fitted_list  =
    sorted(glob.glob('./figure_stat1/data_currentFitted_20*.npy'))
cmpc_Fitted_list   =
    sorted(glob.glob('./figure_stat1/data_cmpcFitted20*.npy'))
hist_Fitted_list   =
    sorted(glob.glob('./figure_stat1/data_histFitted20*.npy'))
rcp26_Fitted_list    =
    sorted(glob.glob('./figure_stat1/data_rcp26Fitted20*.npy'))
rcp85_Fitted_list    =
    sorted(glob.glob('./figure_stat1/data_rcp85Fitted20*.npy'))

df_curr  = pd.DataFrame()
df_rcp26 = pd.DataFrame()
df_rcp85 = pd.DataFrame()
df_cmpc    = pd.DataFrame()
df_hist    = pd.DataFrame()

for year in xrange(len(current_Fitted_list)):
   year_mark = 2006 + year

   current_Fitted    = np.load(current_Fitted_list[year])
   cmpc_Fitted     = np.load(cmpc_Fitted_list[year])
   hist_Fitted     = np.load(hist_Fitted_list[year])
   rcp26_Fitted    = np.load(rcp26_Fitted_list[year])
   rcp85_Fitted    = np.load(rcp85_Fitted_list[year])

   value_curr = [np.max(current_Fitted[j:j+24,:,:], axis=0) for j in
      range(0, current_Fitted.shape[0], 24)]
   value_curr = np.array(value_curr)
   value_cmpc = [np.max(cmpc_Fitted[j:j+24,:,:], axis=0) for j in
      range(0, cmpc_Fitted.shape[0], 24)]
   value_cmpc = np.array(value_cmpc)
   value_hist = [np.max(hist_Fitted[j:j+24,:,:], axis=0) for j in
      range(0, hist_Fitted.shape[0], 24)]
   value_hist = np.array(value_hist)


   #plot histogram of current and future tmax [:,60,60]

   fig, (ax1, ax2, ax3, ax4, ax5)  = plt.subplots(nrows=5, ncols=1,
```

```
    figsize=(8,25))
n1, bins1, patches1  = ax1.hist(value_curr[:,60,65], 25,
    range=(31,36), color='blue', label='Present -averaged
    Td_max'+str(year_mark))
n2, bins2, patches2  = ax2.hist(value_rcp26[:,60,65], 25,
    range=(31,36), color='aquamarine', label='RCP2.6 -averaged
    Td_max'+str(year_mark))
n3, bins3, patches3  = ax3.hist(value_rcp85[:,60,65], 25,
    range=(31,36), color='salmon', label='RCP8.5 -averaged
    Td_max'+str(year_mark))
n4, bins4, patches4  = ax4.hist(value_cmpc[:,60,65], 25,
    range=(31,36), color='green', label='RCP2.6&Cmpc. -averaged
    Td_max'+str(year_mark))
n5, bins5, patches5  = ax5.hist(value_hist[:,60,65], 25,
    range=(31,36), color='red', label='RCP8.5&BaU -averaged
    Td_max'+str(year_mark))
ax1.legend(loc ='upper left')
ax2.legend(loc ='upper left')
ax3.legend(loc ='upper left')
ax4.legend(loc ='upper left')
ax5.legend(loc ='upper left')
plt.savefig('../mortality_image/data_tmax_model_'+ str(year_mark)
    +'.png')
plt.close()



curr_p    = pd.DataFrame(value_curr[:,60,65])
rcp26_p   = pd.DataFrame(value_rcp26[:,60,65])
rcp85_p   = pd.DataFrame(value_rcp85[:,60,65])
cmpc_p    = pd.DataFrame(value_cmpc[:,60,65])
hist_p    = pd.DataFrame(value_hist[:,60,65])

df_append_curr = df_curr.append(curr_p)
df_curr      = df_append_curr
del curr_p

df_append_rcp26 = df_rcp26.append(rcp26_p)
df_rcp26  = df_append_rcp26
del rcp26_p

df_append_rcp85 = df_rcp85.append(rcp85_p)
df_rcp85  = df_append_rcp85
```

```
    del rcp85_p

    df_append_cmpc = df_cmpc.append(cmpc_p)
    df_cmpc      = df_append_cmpc
    del cmpc_p

    df_append_hist = df_hist.append(hist_p)
    df_hist      = df_append_hist
    del hist_p


#===========CALCULATING DAV==============#


    #DAV CURRENT
    dav_curr = np.zeros_like(value_curr)
    death_rate_curr = np.zeros_like(value_curr)

    for i in xrange(value_curr.shape[0]):
       for j in xrange(value_curr.shape[1]):
          for k in xrange(value_curr.shape[2]):

             t_max   = value_curr[i,j,k]
             t_count = t_max - topt_obs
             if t_count > 0.0:
                print i,j,k
                RR = (0.0125*(t_count**2) + 0.025*t_count + 1) - 1
                pop65 = pop_ratio65_2014 * arr_pdCMPC_curr[j,k]
                death   = cdr_day2014 * pop65
                dav     = death * function_coef_thai * RR
                dav_curr[i,j,k] = dav
                a = cdr_65_2014 *1000* function_coef_thai
                death_rate_curr[i,j,k] = a * RR #unit : every 1000
                    population
             else:
                continue

    dav_curr_sum = np.sum(dav_curr, axis=0)
    dav_curr_mean = np.mean(dav_curr, axis=0)
    dav_curr_sum_DR = np.sum(death_rate_curr, axis=0)
    dav_curr_mean_DR = np.mean(death_rate_curr, axis=0)
```

```
np.save('../mortality_image/dav_curr_sum_'+str(year_mark),
    dav_curr_sum)
np.save('../mortality_image/dav_curr_mean_'+str(year_mark),
    dav_curr_mean)
np.save('../mortality_image/dav_curr_sum_DR_'+str(year_mark),
    dav_curr_sum_DR)
np.save('../mortality_image/dav_curr_mean_DR_'+str(year_mark),
    dav_curr_mean_DR)


#DAV COMPACT
dav_cmpc = np.zeros_like(value_cmpc)
death_rate_cmpc = np.zeros_like(value_cmpc)
for i in xrange(value_cmpc.shape[0]):
   for j in xrange(value_cmpc.shape[1]):
      for k in xrange(value_cmpc.shape[2]):

         t_max   = value_cmpc[i,j,k]
         t_count = t_max - topt_obs
         if t_count > 0.0:
            print i,j,k
            RR = (0.0125*(t_count**2) + 0.025*t_count + 1) - 1
            pop65 = pop_ratio65_2050 * arr_pdCMPC_2050[j,k]
            death   = cdr_day2050 * pop65
            dav     = death * function_coef_thai * RR
            dav_cmpc[i,j,k] = dav
            a = cdr_65_2050*1000 * function_coef_thai
            death_rate_cmpc[i,j,k] = a * RR #unit : every 1000
                population
         else:
            continue

dav_cmpc_sum = np.sum(dav_cmpc, axis=0)
dav_cmpc_mean = np.mean(dav_cmpc, axis=0)
dav_cmpc_sum_DR = np.sum(death_rate_cmpc, axis=0)
dav_cmpc_mean_DR = np.mean(death_rate_cmpc, axis=0)


np.save('../mortality_image/dav_cmpc_sum_'+str(year_mark),
    dav_cmpc_sum)
np.save('../mortality_image/dav_cmpc_mean_'+str(year_mark),
    dav_cmpc_mean)
np.save('../mortality_image/dav_cmpc_sum_DR_'+str(year_mark),
```

```
    dav_cmpc_sum_DR)
np.save('../mortality_image/dav_cmpc_mean_DR_'+str(year_mark),
    dav_cmpc_mean_DR)


#DAV BAU
dav_hist = np.zeros_like(value_hist)
death_rate_hist = np.zeros_like(value_hist)

for i in xrange(value_hist.shape[0]):
   for j in xrange(value_hist.shape[1]):
      for k in xrange(value_hist.shape[2]):

         t_max   = value_hist[i,j,k]
         t_count = t_max - topt_obs
         if t_count > 0.0:
            print i,j,k
            RR = (0.0125*(t_count**2) + 0.025*t_count + 1) - 1
            pop65 = pop_ratio65_2050 * arr_pdHIST_2050[j,k]
            death   = cdr_day2050 * pop65
            dav     = death * function_coef_thai * RR
            dav_hist[i,j,k] = dav
            a = cdr_65_2050*1000 * function_coef_thai
            death_rate_hist[i,j,k] = a * RR #unit : every 1000
                population
         else:
            continue

dav_hist_sum = np.sum(dav_hist, axis=0)
dav_hist_mean = np.mean(dav_hist, axis=0)
dav_hist_sum_DR = np.sum(death_rate_hist, axis=0)
dav_hist_mean_DR = np.mean(death_rate_hist, axis=0)


np.save('../mortality_image/dav_hist_sum_'+str(year_mark),
    dav_hist_sum)
np.save('../mortality_image/dav_hist_mean_'+str(year_mark),
    dav_hist_mean)
np.save('../mortality_image/dav_hist_sum_DR_'+str(year_mark),
    dav_hist_sum_DR)
np.save('../mortality_image/dav_hist_mean_DR_'+str(year_mark),
    dav_hist_mean_DR)
```

```
#Plotting for risk per 100,000 population

plot_map(lon, lat, dav_curr_mean_DR*100, 0.00001, 0.03,
    'curr_mor_mean_100000pop'+str(year_mark))
plot_map(lon, lat, dav_cmpc_mean_DR*100, 0.00001, 0.03,
    'cmpc_mor_mean_100000pop'+str(year_mark))
plot_map(lon, lat, dav_hist_mean_DR*100, 0.00001, 0.03,
    'BaU_mor_mean_100000pop'+str(year_mark))

#Plotting Td_max
plot_map(lon, lat, np.mean(value_cmpc, axis=0), 25., 35.,
    'cmpc_tmax'+str(year_mark))
plot_map(lon, lat, np.mean(value_curr, axis=0), 25., 35.,
    'curr_tmax'+str(year_mark))
plot_map(lon, lat, np.mean(value_hist, axis=0), 25., 35.,
    'bau_tmax'+str(year_mark))
```

C

NCL programs for adding pseudo global warming values to present NCEP-FNL

C.1 Adding pseudo global warming values to present NCEP-FNL

```
;;;;;;;;;;;;;;;;;;;;;;;;;;;;;;;;;;;;;;;;;;;;;
;; This program is intended to add CMIP-5 PGW metgrid data
;; into the current metgrid files
;; Please rename/copy PGW files by removing the date and changing it to
   PGW for ALL DOMAINS.
;; ex. met_em.d01.2055-12-16_12:00:00.nc --> met_em.d01.PGW.nc
;; created by Alvin C.G. Varquez and Nisrina S. Darmanto
;;;;;;;;;;;;;;;;;;;;;;;;;;;;;;;;;;;;;;;;;;;;;
begin
src_directory = "./met_future_ensemble_85_meteo/" ;; INPUT
domains = 3                    ;; INPUT
;;;;; INPUT soil temperature variables
soilvars = (/"SKINTEMP","SST","SOILT","ST000010","ST010035", ~C~
"ST010040","ST035100","ST040100","ST100200", ~C~
"ST010200","ST000007","ST007028","ST028100","ST100255", ~C~
"SOILT000","SOILT005","SOILT020","SOILT040","SOILT160","SOILT300","SOILT050"/)
   ;; INPUT
numsoilvars = dimsizes(soilvars)
print(numsoilvars)
do dom=1,domains ;;; Loop for domains
met_files = systemfunc("ls -1 --color=none
   "+src_directory+"met_*d0"+dom+"*00:00.nc");
```

```
met_count=dimsizes(met_files)
print("There are "+met_count+" files in domain 0"+dom);
;; Read necessary parameters from the PGW files;
f=addfile(src_directory+"met_em.d0"+dom+".PGW.nc","r");
PRES_PGW=f->PRES
TT_PGW=f->TT
UU_PGW=f->UU
VV_PGW=f->VV
RH_PGW=f->RH
GHT_PGW=f->GHT
SKINTEMP_PGW=f->SKINTEMP
do ifil=0,dimsizes(met_files)-1 ;;; Loop for met files
print("Working on: "+met_files(ifil));
targ=addfile(met_files(ifil),"wb");
PRES=targ->PRES
TT=targ->TT
UU=targ->UU
VV=targ->VV
RH=targ->RH
GHT=targ->GHT
XLAT_M = targ->XLAT_M
XLON_M = targ->XLONG_M
XLAT_U = targ->XLAT_U
XLON_U = targ->XLONG_U
XLAT_V = targ ->XLAT_V
XLON_V = targ ->XLONG_V
;;;;;;;;;; 4-D Variables ;;;;;;;;;;;;;;;;;
inter_val=int2p_n(PRES_PGW(:,1:,:,:),TT_PGW(:,1:,:,:),PRES,-2,1)
targ->TT = TT+inter_val
delete(inter_val)
inter_val=int2p_n(PRES_PGW(:,1:,:,:),RH_PGW(:,1:,:,:),PRES,-2,1)
targ->RH = RH+inter_val
delete(inter_val)
inter_val=int2p_n(PRES_PGW(:,1:,:,:),GHT_PGW(:,1:,:,:),PRES,-2,1)
targ->GHT = GHT+inter_val
delete(inter_val)
;;for U
PRES_U=linint2(XLON_M(0,0,:),XLAT_M(0,:,0),PRES,False,XLON_U(0,0,:),XLAT_U(0,:,0),0)
dimsnew = dimsizes(PRES_U)
dimsold = dimsizes(PRES)
PRES_U(:,:,:,0)=PRES(:,:,:,0)
PRES_U(:,:,:,dimsnew(3)-1) = PRES(:,:,:,dimsold(3)-1)
PRES_U_PGW=linint2(XLON_M(0,0,:),XLAT_M(0,:,0), ~C~
```

```
PRES_PGW,False,XLON_U(0,0,:),XLAT_U(0,:,0),0)
PRES_U_PGW(:,:,:,0)=PRES_PGW(:,:,:,0)
PRES_U_PGW(:,:,:,dimsnew(3)-1) = PRES_PGW(:,:,:,dimsold(3)-1)
inter_val=int2p_n(PRES_U_PGW(:,1:,:,:),UU_PGW(:,1:,:,:),PRES_U,-2,1)
targ->UU = UU+inter_val
delete(inter_val)
;;for V
PRES_V=linint2(XLON_M(0,0,:),XLAT_M(0,:,0),PRES,False,XLON_V(0,0,:),XLAT_V(0,:,0),0)
dimsnew = dimsizes(PRES_V)
dimsold = dimsizes(PRES)
PRES_V(:,:,0,:)=PRES(:,:,0,:)
PRES_V(:,:,dimsnew(2)-1,:) = PRES(:,:,dimsold(2)-1,:)
PRES_V_PGW=linint2(XLON_M(0,0,:),XLAT_M(0,:,0), ~C~
PRES_PGW,False,XLON_V(0,0,:),XLAT_V(0,:,0),0)
PRES_V_PGW(:,:,0,:)=PRES_PGW(:,:,0,:)
PRES_V_PGW(:,:,dimsnew(2)-1,:) = PRES_PGW(:,:,dimsold(2)-1,:)
inter_val=int2p_n(PRES_V_PGW(:,1:,:,:),VV_PGW(:,1:,:,:),PRES_V,-2,1)
targ->VV = VV+inter_val
delete(inter_val)


;;;;;;;;;; Soil temperature, skin temperature, SST ;;;;;;;;;;;;;;
;;;;; INPUT soil temperature variables
;soilvars = (/"SKINTEMP","SST","SOILT","ST000010",~C~
"ST010035","ST010040","ST035100","ST040100","ST100200", ~C~
"ST010200","ST000007","ST007028","ST028100","ST100255", ~C~
"SOILT000","SOILT005","SOILT020","SOILT040","SOILT160","SOILT300","SOILT050"/)
;numsoilvars = dimsizes(soilvars)
;print(numsoilvars)
do ivar=0,numsoilvars-1
if(isfilevar(targ,soilvars(ivar))) then
  svar=targ->$soilvars(ivar)$
 ; printVarSummary(svar)
 ; printVarSummary(SKINTEMP_PGW)
  targ->$soilvars(ivar)$ = svar+SKINTEMP_PGW
  delete(svar)
end if
end do

;;;for_ST
do iivar=0,3
    svar=targ->ST(:,iivar,:,:)
    targ->ST(:,iivar,:,:)=svar+SKINTEMP_PGW
```

```
    delete(svar)
end do

delete(XLAT_U)
delete(XLAT_V)
delete(XLAT_M)
delete(XLON_U)
delete(XLON_V)
delete(XLON_M)
delete(PRES_U)
delete(PRES_U_PGW)
delete(PRES_V)
delete(PRES_V_PGW)
delete(targ)
delete(PRES)
delete(TT)
delete(UU)
delete(VV)
delete(RH)
delete(GHT)
end do
delete(met_files)
delete(f)
delete(TT_PGW)
delete(UU_PGW)
delete(VV_PGW)
delete(RH_PGW)
delete(GHT_PGW)
delete(SKINTEMP_PGW)
delete(PRES_PGW)
end do
end
```

References

Adachi, S. A., Kimura, F., Kusaka, H., Inoue, T., and Ueda, H. (2012). Comparison of the Impact of Global Climate Changes and Urbanization on Summertime Future Climate in the Tokyo Metropolitan Area. *Journal of Applied Meteorology and Climatology*, 51(8):1441–1454.

Alexander, P., Bechtel, B., Chow, W., Fealy, R., and Mills, G. (2016). Linking urban climate classification with an urban energy and water budget model: Multi-site and multi-seasonal evaluation. *Urban Climate*, 17:196–215.

Alexander, P. J., Mills, G., and Fealy, R. (2015). Using LCZ data to run an urban energy balance model. *Urban Climate*, 13:14–37.

Anderson, G. B., Oleson, K. W., Jones, B., and Peng, R. D. (2018). Projected trends in high-mortality heatwaves under different scenarios of climate, population, and adaptation in 82 US communities. *Climatic Change*, 146(3-4):455–470.

Argüeso, D., Evans, J. P., Pitman, A. J., and Di Luca, A. (2015). Effects of City Expansion on Heat Stress under Climate Change Conditions. *PLOS ONE*, 10(2):e0117066.

Arnfield, A. J. (2003). Two decades of urban climate research: a review of turbulence, exchanges of energy and water, and the urban heat island. *International Journal of Climatology*, 23(1):1–26.

Badan Pusat Statistik (2013). *Proyeksi penduduk Indonesia 2010-2035*. OCLC: 1030426061.

Bechtel, B., Alexander, P., Böhner, J., Ching, J., Conrad, O., Feddema, J., Mills, G., See, L., and Stewart, I. (2015). Mapping Local Climate Zones for a Worldwide Database of the Form and Function of Cities. *ISPRS International Journal of Geo-Information*, 4(1):199–219.

Bechtel, B., See, L., Mills, G., and Foley, M. (2016). Classification of Local Climate Zones Using SAR and Multispectral Data in an Arid Environment. *IEEE Journal of Selected Topics in Applied Earth Observations and Remote Sensing*, 9(7):3097–3105.

Best, M. J. (2006). Progress towards better weather forecasts for city dwellers: from short range to climate change. *Theoretical and Applied Climatology*, 84(1-3):47–55.

Bihamta, N., Soffianian, A., Fakheran, S., and Gholamalifard, M. (2015). Using the SLEUTH Urban Growth Model to Simulate Future Urban Expansion of the Isfahan Metropolitan Area, Iran. *Journal of the Indian Society of Remote Sensing*, 43(2):407–414.

Bornstein, R. D. (1968). Observations of the Urban Heat Island Effect in New York City. *Journal of Applied Meteorology*, 7(4):575–582.

Brousse, O., , A., Foley, M., Mills, G., and Bechtel, B. (2016). WUDAPT, an efficient land use producing data tool for mesoscale models? Integration of urban LCZ in WRF over Madrid. *Urban Climate*, 17:116–134.

C40 cities (2018). Mayoral powers in Jakarta.

Cai, M., Ren, C., Xu, Y., Dai, W., and Wang, X. M. (2016). Local Climate Zone Study for Sustainable Megacities Development by Using Improved WUDAPT Methodology –A Case Study in Guangzhou. *Procedia Environmental Sciences*, 36:82–89.

Carabajal, C. C., Harding, D. J., Boy, J.-P., Danielson, J. J., Gesch, D. B., and Suchdeo, V. P. (2011). Evaluation of the Global Multi-Resolution Terrain Elevation Data 2010 (GMTED2010) using ICESat geodetic control. page 82861Y, Nanjing, China.

Chen, B., Shi, G., Wang, B., Zhao, J., and Tan, S. (2012). Estimation of the anthropogenic heat release distribution in China from 1992 to 2009. *Acta Meteorologica Sinica*, 26(4):507–515.

Chen, F., Kusaka, H., Bornstein, R., Ching, J., Grimmond, C. S. B., Grossman-Clarke, S., Loridan, T., Manning, K. W., Martilli, A., Miao, S., Sailor, D., Salamanca, F. P., Taha, H., Tewari, M., Wang, X., Wyszogrodzki, A. A., and Zhang, C. (2011). The integrated WRF/urban modelling system: development, evaluation, and applications to urban environmental problems. *International Journal of Climatology*, 31(2):273–288.

Clarke, K., Hoppen, S., and Gaydos, L. (1997). A self-modifying cellular automaton model of historical urbanization in the San Francisco Bay area. *Environment and Planning B: Planning and Design*, 24(2):247–261.

Cox, R., Bauer, B. L., and Smith, T. (1998). A Mesoscale Model Intercomparison. *Bulletin of the American Meteorological Society*, 79(2):265–284.

Danylo, O., See, L., Bechtel, B., Schepaschenko, D., and Fritz, S. (2016). Contributing to WUDAPT: A Local Climate Zone Classification of Two Cities in Ukraine. *IEEE Journal of Selected Topics in Applied Earth Observations and Remote Sensing*, 9(5):1841–1853.

de Munck, C., Lemonsu, A., Masson, V., Le Bras, J., and Bonhomme, M. (2018). Evaluating the impacts of greening scenarios on thermal comfort and energy and water consumptions for adapting Paris city to climate change. *Urban Climate*, 23:260–286.

Demographia (2018). Demographia World Urban Areas (Built-Up Urban Areas or Urban Agglomerations). Annual Report 14.

Demuzere, M., Harshan, S., Järvi, L., Roth, M., Grimmond, C. S. B., Masson, V., Oleson, K. W., Velasco, E., and Wouters, H. (2017). Impact of urban canopy models and external parameters on the modelled urban energy balance in a tropical city: Urban Canopy Models and External Parameters Sensitivity. *Quarterly Journal of the Royal Meteorological Society*, 143(704):1581–1596.

Doan, V. Q. and Kusaka, H. (2018). Projections of urban climate in the 2050s in a fast-growing city in Southeast Asia: The greater Ho Chi Minh City metropolitan area, Vietnam. *International Journal of Climatology*, 38(11):4155–4171.

Doan, V. Q., Kusaka, H., and Ho, Q.-B. (2016). Impact of future urbanization on temperature and thermal comfort index in a developing tropical city: Ho Chi Minh City. *Urban Climate*, 17:20–31.

Dobson, J., A. Bright, E., R. Coleman, P., C. Durfee, R., and A. Worley, B. (2000). LandScan: A Global Population Database for Estimating Populations at Risk. 66.

Dong, Y., Varquez, A., and Kanda, M. (2017). Global anthropogenic heat flux database with high spatial resolution. *Atmospheric Environment*, 150:276–294.

Eliasson, I. and Holmer, B. (1990). Urban Heat Island Circulation in G teborg, Sweden. *Theoretical and Applied Climatology*, 42(3):187–196.

Elvidge, C. D., Baugh, K. E., Zhizhin, M., and Hsu, F.-C. (2013). Why VIIRS data are superior to DMSP for mapping nighttime lights. *Proceedings of the Asia-Pacific Advanced Network*, 35(0):62.

Emmanuel, R. (2016). *Urban Climate Challenges in the Tropics: Rethinking Planning and Design Opportunities*. IMPERIAL COLLEGE PRESS.

Fan, F. and Deng, Y. (2014). Enhancing endmember selection in multiple endmember spectral mixture analysis (MESMA) for urban impervious surface area mapping using spectral angle and spectral distance parameters. *International Journal of Applied Earth Observation and Geoinformation*, 33:290–301.

Fischer, E. M., Oleson, K. W., and Lawrence, D. M. (2012). Contrasting urban and rural heat stress responses to climate change: HEAT STRESS RESPONSE TO CLIMATE CHANGE. *Geophysical Research Letters*, 39(3):n/a–n/a.

FrontlineSolvers (2018). Rule of thumbs on feedforward artificial neural network.

Fujimori, S., Hasegawa, T., and Masui, T. (2017). AIM/CGE V2.0: Basic Feature of the Model. In Fujimori, S., Kainuma, M., and Masui, T., editors, *Post-2020 Climate Action*, pages 305–328. Springer Singapore, Singapore.

Fujimori, S., Masui, T., and Matsuoka, Y. (2012). AIM/CGE [basic] manual. *Center for Social and Environmental Systems Research, NIES: Tsukuba, Japan*.

Fujimori, S., Masui, T., and Matsuoka, Y. (2014). Development of a global computable general equilibrium model coupled with detailed energy end-use technology. *Applied Energy*, 128:296–306.

Gasparrini, A., Guo, Y., Hashizume, M., Lavigne, E., Zanobetti, A., Schwartz, J., Tobias, A., Tong, S., Rocklöv, J., Forsberg, B., Leone, M., De Sario, M., Bell, M. L., Guo, Y.-L. L., Wu, C.-f., Kan, H., Yi, S.-M., de Sousa Zanotti Stagliorio Coelho, M., Saldiva, P. H. N., Honda, Y., Kim, H., and Armstrong, B. (2015). Mortality risk attributable to high and low ambient temperature: a multicountry observational study. *The Lancet*, 386(9991):369–375.

Georgescu, M. (2015). Challenges Associated with Adaptation to Future Urban Expansion. *Journal of Climate*, 28(7):2544–2563.

Georgescu, M., Morefield, P. E., Bierwagen, B. G., and Weaver, C. P. (2014). Urban adaptation can roll back warming of emerging megapolitan regions. *Proceedings of the National Academy of Sciences*, 111(8):2909–2914.

Grimmond, C. S. B., Blackett, M., Best, M. J., Baik, J.-J., Belcher, S. E., Beringer, J., Bohnenstengel, S. I., Calmet, I., Chen, F., Coutts, A., Dandou, A., Fortuniak, K., Gouvea, M. L., Hamdi, R., Hendry, M., Kanda, M., Kawai, T., Kawamoto, Y., Kondo, H., Krayenhoff, E. S., Lee, S.-H., Loridan, T., Martilli,

A., Masson, V., Miao, S., Oleson, K., Ooka, R., Pigeon, G., Porson, A., Ryu, Y.-H., Salamanca, F., Steeneveld, G., Tombrou, M., Voogt, J. A., Young, D. T., and Zhang, N. (2011). Initial results from Phase 2 of the international urban energy balance model comparison. *International Journal of Climatology*, 31(2):244–272.

Grimmond, C. S. B. and Oke, T. R. (1999). Aerodynamic Properties of Urban Areas Derived from Analysis of Surface Form. *Journal of Applied Meteorology*, 38(9):1262–1292.

Grimmond, C. S. B. and Oke, T. R. (2002). Turbulent Heat Fluxes in Urban Areas: Observations and a Local-Scale Urban Meteorological Parameterization Scheme (LUMPS). *Journal of Applied Meteorology*, 41(7):792–810.

Guttikunda, S. K., Carmichael, G. R., Calori, G., Eck, C., and Woo, J.-H. (2003). The contribution of megacities to regional sulfur pollution in Asia. *Atmospheric Environment*, 37(1):11–22.

Guttikunda, S. K., Goel, R., and Pant, P. (2014). Nature of air pollution, emission sources, and management in the Indian cities. *Atmospheric Environment*, 95:501–510.

Hagishima, A., Tanimoto, J., Nagayama, K., and Meno, S. (2009). Aerodynamic Parameters of Regular Arrays of Rectangular Blocks with Various Geometries. *Boundary-Layer Meteorology*, 132(2):315–337.

Hales, S., Kovats, S., Lloyd, S., Campbell-Lendrum, D., World Health Organization, World Health Organization, and Health Security and Environment Cluster (2014). *Quantitative risk assessment of the effects of climate change on selected causes of death, 2030s and 2050s*. OCLC: 972886077.

Hamdi, R. and Masson, V. (2008). Inclusion of a Drag Approach in the Town Energy Balance (TEB) Scheme: Offline 1d Evaluation in a Street Canyon. *Journal of Applied Meteorology and Climatology*, 47(10):2627–2644.

Hamdi, R., Van de Vyver, H., De Troch, R., and Termonia, P. (2014). Assessment of three dynamical urban climate downscaling methods: Brussels's future urban heat island under an A1b emission scenario: BRUSSELS'S FUTURE URBAN HEAT ISLAND. *International Journal of Climatology*, 34(4):978–999.

Harman, I. N., Best, M. J., and Belcher, S. E. (2004). Radiative Exchange in an Urban Street Canyon. *Boundary-Layer Meteorology*, 110(2):301–316.

Hidalgo, J., Masson, V., and Gimeno, L. (2010). Scaling the Daytime Urban Heat Island and Urban-Breeze Circulation. *Journal of Applied Meteorology and Climatology*, 49(5):889–901.

Honda, Y., Kabuto, M., Ono, M., and Uchiyama, I. (2007). Determination of optimum daily maximum temperature using climate data. *Environmental Health and Preventive Medicine*, 12(5):209–216.

Honda, Y., Kondo, M., McGregor, G., Kim, H., Guo, Y.-L., Hijioka, Y., Yoshikawa, M., Oka, K., Takano, S., Hales, S., and Kovats, R. S. (2014). Heat-related mortality risk model for climate change impact projection. *Environmental Health and Preventive Medicine*, 19(1):56–63.

Honda, Y., Ono, M., Sasaki, A., and Uchiyama, I. (1998). Shift of the short-term temperature mortality relationship by a climate factor - some evidence necessary to take account of in estimating the health effect of global warming. *Journal of Risk Research*, 1(3):209–220.

Honda, Y., Ono, M., and Uchiyama, I. (2000). Humidity does not Confound Temperature-Mortality Relationship in Japan. *JAPANESE JOURNAL OF BIOMETEOROLOGY*, 37(4):117–122.

Hsu, F.-C., Baugh, E. K., Ghosh, T., Zhizhin, M., and Elvidge, D. C. (2015). DMSP-OLS Radiance Calibrated Nighttime Lights Time Series with Intercalibration. *Remote Sensing*, 7(2).

Huang, Q., Yang, Y., Li, Y., and Gao, B. (2016). A Simulation Study on the Urban Population of China Based on Nighttime Light Data Acquired from DMSP/OLS. *Sustainability*, 8(6).

Iizuka, S. (2018). Future environmental assessment and urban planning by downscaling simulations. *Journal of Wind Engineering and Industrial Aerodynamics*, 181:69–78.

Iizuka, S., Xuan, Y., and Kondo, Y. (2015). Impacts of disaster mitigation/prevention urban structure models on future urban thermal environment. *Sustainable Cities and Society*, 19:414–420.

IPCC (2014). Detection and Attribution of Climate Change: from Global to Regional. In Intergovernmental Panel on Climate Change, editor, *Climate Change 2013 - The Physical Science Basis*, pages 867–952. Cambridge University Press, Cambridge.

Isaac, M. and van Vuuren, D. P. (2009). Modeling global residential sector energy demand for heating and air conditioning in the context of climate change. *Energy Policy*, 37(2):507–521.

Jantz, C. A., Goetz, S. J., Donato, D., and Claggett, P. (2010). Designing and implementing a regional urban modeling system using the SLEUTH cellular urban model. *Computers, Environment and Urban Systems*, 34(1):1–16.

JMA (2011). Climate Change Monitoring Report 2010. Technical report, Japan Meteorological Agency.

Kalnay, E. and Cai, M. (2003). Impact of urbanization and land-use change on climate. *Nature*, 423(6939):528–531.

Kaloustian, N. and Bechtel, B. (2016). Local Climatic Zoning and Urban Heat Island in Beirut. *Procedia Engineering*, 169:216–223.

Kanda, M., Inagaki, A., Miyamoto, T., Gryschka, M., and Raasch, S. (2013). A New Aerodynamic Parametrization for Real Urban Surfaces. *Boundary-Layer Meteorology*, 148(2):357–377.

Kanda, M., Kanega, M., Kawai, T., Moriwaki, R., and Sugawara, H. (2007). Roughness Lengths for Momentum and Heat Derived from Outdoor Urban Scale Models. *Journal of Applied Meteorology and Climatology*, 46(7):1067–1079.

Kanda, M., Kawai, T., Kanega, M., Moriwaki, R., Narita, K., and Hagishima, A. (2005a). A Simple Energy Balance Model for Regular Building Arrays. *Boundary-Layer Meteorology*, 116(3):423–443.

Kanda, M., Kawai, T., and Nakagawa, K. (2005b). A Simple Theoretical Radiation Scheme for Regular Building Arrays. *Boundary-Layer Meteorology*, 114(1):71–90.

Kardinal Jusuf, S., Wong, N., Hagen, E., Anggoro, R., and Hong, Y. (2007). The influence of land use on the urban heat island in Singapore. *Habitat International*, 31(2):232–242.

Kawai, T., Ridwan, M. K., and Kanda, M. (2009). Evaluation of the Simple Urban Energy Balance Model Using Selected Data from 1-yr Flux Observations at Two Cities. *Journal of Applied Meteorology and Climatology*, 48(4):693–715.

Kawano, N. (2018). *Distributed Urban Parametric Database for Global Urban Climatology (グローバル都市気象学のための地表面データの構築と適用)*. 学位論文 (博士) 論文要旨, Tokyo Institute of Technology, Tokyo, Japan.

Kawano, N., Dong, Y., Yucel, M., Varquez, A., and Kanda, M. (2016). Global Urban Climatology: General Simulation Framework for Heat Island Analysis. *Journal of Japan Society of Civil Engineers*, 72(4):I_97–I_102.

Kent, C. W., Grimmond, S., Gatey, D., and Hirano, K. (2019). Urban morphology parameters from global digital elevation models: Implications for aerodynamic roughness and for wind-speed estimation. *Remote Sensing of Environment*, 221:316–339.

Kimura, F. and Kitoh, A. (2007). Downscaling by Pseudo Global Warning Method. *The Final Report of ICCAP*, pages 43–46.

Kondo, H., Genchi, Y., Kikegawa, Y., Ohashi, Y., Yoshikado, H., and Komiyama, H. (2005). Development of a Multi-Layer Urban Canopy Model for the Analysis of Energy Consumption in a Big City: Structure of the Urban Canopy Model and its Basic Performance. *Boundary-Layer Meteorology*, 116(3):395–421.

Kovats, R. S. and Hajat, S. (2008). Heat Stress and Public Health: A Critical Review. *Annual Review of Public Health*, 29(1):41–55.

Kusaka, H., Hara, M., and Takane, Y. (2012). Urban Climate Projection by the WRF Model at 3-km Horizontal Grid Increment: Dynamical Downscaling and Predicting Heat Stress in the 2070^|^rsquo;s August for Tokyo, Osaka, and Nagoya Metropolises. *Journal of the Meteorological Society of Japan. Ser. II*, 90B(0):47–63.

Kusaka, H. and Kimura, F. (2004). Coupling a Single-Layer Urban Canopy Model with a Simple Atmospheric Model: Impact on Urban Heat Island Simulation for an Idealized Case. *Journal of the Meteorological Society of Japan*, 82(1):67–80.

Kusaka, H., Kimura, F., Hirakuchi, H., and Mizutori, M. (2000). The Effects of Land-Use Alteration on the Sea Breeze and Daytime Heat Island in the Tokyo Metropolitan Area. *Journal of the Meteorological Society of Japan. Ser. II*, 78(4):405–420.

Kusaka, H., Kondo, H., Kikegawa, Y., and Kimura, F. (2001). A Simple Single-Layer Urban Canopy Model For Atmospheric Models: Comparison With Multi-Layer And Slab Models. *Boundary-Layer Meteorology*, 101(3):329–358.

Kusaka, H., Suzuki-Parker, A., Aoyagi, T., Adachi, S. A., and Yamagata, Y. (2016). Assessment of RCM and urban scenarios uncertainties in the climate projections for August in the 2050s in Tokyo. *Climatic Change*, 137(3-4):427–438.

Le Bras, J. and Masson, V. (2015). A fast and spatialized urban weather generator for long-term urban studies at the city-scale. *Frontiers in Earth Science*, 3:27.

Lebassi-Habtezion, B., González, J., and Bornstein, R. (2011). Modeled large-scale warming impacts on summer California coastal-cooling trends. *Journal of Geophysical Research*, 116(D20).

Lee, H. S., Trihamdani, A. R., Kubota, T., Iizuka, S., and Phuong, T. T. T. (2017). Impacts of land use changes from the Hanoi Master Plan 2030 on urban heat islands: Part 2. Influence of global warming. *Sustainable Cities and Society*, 31:95–108.

Lemonsu, A., Kounkou-Arnaud, R., Desplat, J., Salagnac, J.-L., and Masson, V. (2013). Evolution of the Parisian urban climate under a global changing climate. *Climatic Change*, 116(3-4):679–692.

Lemonsu, A., Viguié, V., Daniel, M., and Masson, V. (2015). Vulnerability to heat waves: Impact of urban expansion scenarios on urban heat island and heat stress in Paris (France). *Urban Climate*, 14:586–605.

Li, D., Bou-Zeid, E., Baeck, M. L., Jessup, S., and Smith, J. A. (2013). Modeling Land Surface Processes and Heavy Rainfall in Urban Environments: Sensitivity to Urban Surface Representations. *Journal of Hydrometeorology*, 14(4):1098–1118.

Li, D., Malyshev, S., and Shevliakova, E. (2016). Exploring historical and future urban climate in the Earth System Modeling framework: 1. Model development and evaluation: URBAN CLIMATE IN EARTH SYSTEM MODELS. *Journal of Advances in Modeling Earth Systems*, 8(2):917–935.

Luca Congedo (2016). Semi-Automatic Classification Plugin Documentation. Release 5.3.6.1.

MacGregor, G. R. and Nieuwolt, S. (1998). *Tropical climatology: an introduction to the climates of the low latitudes*. Wiley, Chichester, 2. ed edition. OCLC: 245974667.

Martilli, A. (2014). An idealized study of city structure, urban climate, energy consumption, and air quality. *Urban Climate*, 10:430–446.

Martilli, A., Clappier, A., and Rotach, M. W. (2002). An Urban Surface Exchange Parameterisation for Mesoscale Models. *Boundary-Layer Meteorology*, 104(2):261–304.

Masson, V. (2000). A Physically-Based Scheme For The Urban Energy Budget In Atmospheric Models. *Boundary-Layer Meteorology*, 94(3):357–397.

Masson, V., Marchadier, C., Adolphe, L., Aguejdad, R., Avner, P., Bonhomme, M., Bretagne, G., Briottet, X., Bueno, B., de Munck, C., Doukari, O., Hallegatte, S., Hidalgo, J., Houet, T., Le Bras, J., Lemonsu, A., Long, N., Moine, M.-P., Morel, T., Nolorgues, L., Pigeon, G., Salagnac, J.-L., Viguié, V., and Zibouche, K. (2014). Adapting cities to climate change: A systemic modelling approach. *Urban Climate*, 10:407–429.

McCarthy, M. P., Best, M. J., and Betts, R. A. (2010). Climate change in cities due to global warming and urban effects: CLIMATE CHANGE IN CITIES. *Geophysical Research Letters*, 37(9):n/a–n/a.

Miao, S., Chen, F., LeMone, M. A., Tewari, M., Li, Q., and Wang, Y. (2009). An Observational and Modeling Study of Characteristics of Urban Heat Island and Boundary Layer Structures in Beijing. *Journal of Applied Meteorology and Climatology*, 48(3):484–501.

Moriwaki, R. and Kanda, M. (2006). Local and Global Similarity in Turbulent Transfer of Heat, Water Vapour, And CO 2 in the Dynamic Convective Sublayer Over a Suburban Area. *Boundary-Layer Meteorology*, 120(1):163–179.

Nelson, M. A., Brown, M. J., Halverson, S. A., Bieringer, P. E., Annunzio, A., Bieberbach, G., and Meech, S. (2016). A Case Study of the Weather Research and Forecasting Model Applied to the Joint Urban 2003 Tracer Field Experiment. Part 1: Wind and Turbulence. *Boundary-Layer Meteorology*, 158(2):285–309.

Niyogi, D., Lei, M., Kishtawal, C., Schmid, P., and Shepherd, M. (2017). Urbanization Impacts on the Summer Heavy Rainfall Climatology over the Eastern United States. *Earth Interactions*, 21(5):1–17.

Obradovich, N., Migliorini, R., Mednick, S. C., and Fowler, J. H. (2017). Nighttime temperature and human sleep loss in a changing climate. *Science Advances*, 3(5):e1601555.

Oke, T. (1973). City size and the urban heat island. *Atmospheric Environment (1967)*, 7(8):769–779.

Oke, T. R. (1978). *Boundary layer climates*. Methuen, London.

Oke, T. R., Mills, G., Christen, A., and Voogt, J. A. (2017). *Urban climates*. Cambridge University Press, Cambridge New York Melbourne Daryaganj.

Oleson, K. (2012). Contrasts between Urban and Rural Climate in CCSM4 CMIP5 Climate Change Scenarios. *Journal of Climate*, 25(5):1390–1412.

Oleson, K. W., Bonan, G. B., Feddema, J., and Jackson, T. (2011). An examination of urban heat island characteristics in a global climate model. *International Journal of Climatology*, 31(12):1848–1865.

Oleson, K. W., Bonan, G. B., Feddema, J., and Vertenstein, M. (2008a). An Urban Parameterization for a Global Climate Model. Part II: Sensitivity to Input Parameters and the Simulated Urban Heat Island in Offline Simulations. *Journal of Applied Meteorology and Climatology*, 47(4):1061–1076.

Oleson, K. W., Bonan, G. B., Feddema, J., Vertenstein, M., and Grimmond, C. S. B. (2008b). An Urban Parameterization for a Global Climate Model. Part I: Formulation and Evaluation for Two Cities. *Journal of Applied Meteorology and Climatology*, 47(4):1038–1060.

O'Neill, B. C., Kriegler, E., Riahi, K., Ebi, K. L., Hallegatte, S., Carter, T. R., Mathur, R., and van Vuuren, D. P. (2014). A new scenario framework for climate change research: the concept of shared socioeconomic pathways. *Climatic Change*, 122(3):387–400.

Parker, D. E. (2010). Urban heat island effects on estimates of observed climate change. *WIREs Climate Change*, 1(1):123–133.

Patz, J. A., Campbell-Lendrum, D., Holloway, T., and Foley, J. A. (2005). Impact of regional climate change on human health. *Nature*, 438:310.

Piani, C., Haerter, J. O., and Coppola, E. (2010a). Statistical bias correction for daily precipitation in regional climate models over Europe. *Theoretical and Applied Climatology*, 99(1-2):187–192.

Piani, C., Weedon, G., Best, M., Gomes, S., Viterbo, P., Hagemann, S., and Haerter, J. (2010b). Statistical bias correction of global simulated daily precipitation and temperature for the application of hydrological models. *Journal of Hydrology*, 395(3-4):199–215.

Rasmussen, R., Liu, C., Ikeda, K., Gochis, D., Yates, D., Chen, F., Tewari, M., Barlage, M., Dudhia, J., Yu, W., Miller, K., Arsenault, K., Grubišić, V., Thompson, G., and Gutmann, E. (2011). High-Resolution Coupled Climate Runoff Simulations of Seasonal Snowfall over Colorado: A Process Study of Current and Warmer Climate. *Journal of Climate*, 24(12):3015–3048.

Ren, C. (2017). Mapping global cities bu using a common language.

Revi, A., Satterthwaite, D., Aragón-Durand, F., Corfee-Morlot, J., Kiunsi, R., Pelling, M., Roberts, D., and Solecki, W. (2014). Urban areas. In: Climate

Change 2014: Impacts, Adaptation, and Vulnerability. Part A:Global and Sectoral Aspects. Contribution of Working Group II to the Fifth Assessment Report of the Intergovernmental Panel on Climate Change. Technical report, Cambridge University Press, Cambridge, United Kingdom and New York, NY, USA.

Rifkin, D. I., Long, M. W., and Perry, M. J. (2018). Climate change and sleep: A systematic review of the literature and conceptual framework. *Sleep Medicine Reviews*, 42:3–9.

Rosenzweig, C., Solecki, W., Romero-Lankao, P., Mehrotra, S., Dhakal, S., Bowman, T., and Ali Ibrahim, S. (2015). ARC3.2 Summary for City Leaders. Technical report, Columbia University. New York.

Roth, M. (2007a). Review of atmospheric turbulence over cities. *Quarterly Journal of the Royal Meteorological Society*, 126(564):941–990.

Roth, M. (2007b). Review of urban climate research in (sub)tropical regions. *International Journal of Climatology*, 27(14):1859–1873.

Roth, M., Jansson, C., and Velasco, E. (2017). Multi-year energy balance and carbon dioxide fluxes over a residential neighbourhood in a tropical city: MULTI-YEAR ENERGY BALANCE AND CARBON DIOXIDE FLUXES. *International Journal of Climatology*, 37(5):2679–2698.

Roy, D., Wulder, M., Loveland, T., C.E., W., Allen, R., Anderson, M., Helder, D., Irons, J., Johnson, D., Kennedy, R., Scambos, T., Schaaf, C., Schott, J., Sheng, Y., Vermote, E., Belward, A., Bindschadler, R., Cohen, W., Gao, F., Hipple, J., Hostert, P., Huntington, J., Justice, C., Kilic, A., Kovalskyy, V., Lee, Z., Lymburner, L., Masek, J., McCorkel, J., Shuai, Y., Trezza, R., Vogelmann, J., Wynne, R., and Zhu, Z. (2014). Landsat-8: Science and product vision for terrestrial global change research. *Remote Sensing of Environment*, 145:154–172.

Rubel, F. and Kottek, M. (2010). Observed and projected climate shifts 1901-2100 depicted by world maps of the Köppen-Geiger climate classification. *Meteorologische Zeitschrift*, 19(2):135–141.

Rueda, L. M., Patel, K. J., Axtell, R. C., and Stinner, R. E. (1990). Temperature-Dependent Development and Survival Rates of Culex quinquefasciatus and Aedes aegypti (Diptera: Culicidae). *Journal of Medical Entomology*, 27(5):892–898.

Sakieh, Y. and Salmanmahiny, A. (2016). Treating a cancerous landscape: Implications from medical sciences for urban and landscape planning in a developing region. *Habitat International*, 55:180–191.

Salamanca, F., Krpo, A., Martilli, A., and Clappier, A. (2010). A new building energy model coupled with an urban canopy parameterization for urban climate simulations—part I. formulation, verification, and sensitivity analysis of the model. *Theoretical and Applied Climatology*, 99(3-4):331–344.

Salamanca, F., Zhang, Y., Barlage, M., Chen, F., Mahalov, A., and Miao, S. (2018). Evaluation of the WRF-Urban Modeling System Coupled to Noah and Noah-MP Land Surface Models Over a Semiarid Urban Environment. *Journal of Geophysical Research: Atmospheres*, 123(5):2387–2408.

Sato, T., Kimura, F., and Kitoh, A. (2007). Projection of global warming onto regional precipitation over Mongolia using a regional climate model. *Journal of Hydrology*, 333(1):144–154.

Silva, E. and Clarke, K. (2002). Calibration of the SLEUTH urban growth model for Lisbon and Porto, Portugal. *Computers, Environment and Urban Systems*, 26(6):525–552.

Simpson, J. E., Mansfield, D. A., and Milford, J. R. (1977). Inland penetration of sea-breeze fronts. *Quarterly Journal of the Royal Meteorological Society*, 103(435):47–76.

Sintorini, M. M. (2018). The correlation between temperature and humidity with the population density of *Aedes aegypti* as dengue fever's vector. *IOP Conference Series: Earth and Environmental Science*, 106:012033.

Stewart, I. D. and Oke, T. R. (2012). Local Climate Zones for Urban Temperature Studies. *Bulletin of the American Meteorological Society*, 93(12):1879–1900.

Stone, B., Hess, J. J., and Frumkin, H. (2010). Urban Form and Extreme Heat Events: Are Sprawling Cities More Vulnerable to Climate Change Than Compact Cities? *Environmental Health Perspectives*, 118(10):1425–1428.

Stull, R. B. (2009). *An introduction to boundary layer meteorology*. Number 13 in Atmospheric and oceanographic sciences library. Springer, Dordrecht, reprinted edition.

Sutton, P. (1997). Modeling population density with night-time satellite imagery and GIS. *Remote Sensing of Urban Systems*, 21(3):227–244.

Sutton, P. C., Cova, T. J., and Elvidge, C. D. (2006). Mapping "Exurbia" in the Conterminous United States Using Nighttime Satellite Imagery. *Geocarto International*, 21(2):39–45.

Tachikawa, T., Kaku, M., Iwasaki, A., Gesch, D. B., Oimoen, M. J., Zhang, Z., Danielson, J. J., Krieger, T., Curtis, B., Haase, J., Abrams, M., and Carabajal, C. (2011). ASTER Global Digital Elevation Model Version 2 - summary of validation results. Report.

Taha, H. (1997). Urban climates and heat islands: albedo, evapotranspiration, and anthropogenic heat. *Energy and Buildings*, 25(2):99–103.

Takahashi, K., Honda, Y., and Emori, S. (2007). Assessing Mortality Risk from Heat Stress due to Global Warming. *Journal of Risk Research*, 10(3):339–354.

Tewari, M., Salamanca, F., Martilli, A., Treinish, L., and Mahalov, A. (2017). Impacts of projected urban expansion and global warming on cooling energy demand over a semiarid region: Impacts of projected urban expansion and global warming. *Atmospheric Science Letters*, 18(11):419–426.

Trusilova, K., Früh, B., Brienen, S., Walter, A., Masson, V., Pigeon, G., and Becker, P. (2013). Implementation of an Urban Parameterization Scheme into the Regional Climate Model COSMO-CLM. *Journal of Applied Meteorology and Climatology*, 52(10):2296–2311.

Tursilowati, L., Sumatyo, J., Kuze, H., and Adiningsih, E. (2012). The integrated WRF/urban modeling system and its application to monitoring urban heat island in Jakarta-Indonesia. *Journal of Urban and Environmental Engineering*, 6(1):1–9.

United Nations (2015). World Urbanization Prospects: The 2014 Revision. Technical Report ST/ESA/SER.A/366, United Nations, Department of Economic and Social Affairs, Population Division.

United Nations (2018). World Urbanization Prospects: The 2018 Revision. Working Paper ESA/P/WP.252, United Nations, Department of Economic and Social Affairs, Population Division, New York.

van Vuuren, D. P., Edmonds, J., Kainuma, M., Riahi, K., Thomson, A., Hibbard, K., Hurtt, G. C., Kram, T., Krey, V., Lamarque, J.-F., Masui, T., Meinshausen, M., Nakicenovic, N., Smith, S. J., and Rose, S. K. (2011). The representative concentration pathways: an overview. *Climatic Change*, 109(1-2):5–31.

van Vuuren, D. P., Kriegler, E., O'Neill, B. C., Ebi, K. L., Riahi, K., Carter, T. R., Edmonds, J., Hallegatte, S., Kram, T., Mathur, R., and Winkler, H. (2014). A new scenario framework for Climate Change Research: scenario matrix architecture. *Climatic Change*, 122(3):373–386.

Vardoulakis, S., Fisher, B. E., Pericleous, K., and Gonzalez-Flesca, N. (2003). Modelling air quality in street canyons: a review. *Atmospheric Environment*, 37(2):155–182.

Varquez, A. C., Takakuwa, S., Kanda, M., and Xin, Z. (2018). Future population distribution of an urban agglomeration given climate change scenarios. *Journal of Japan Society of Civil Engineers*, 74(4):I_223–I_228.

Varquez, A. C. G., Darmanto, N. S., Kawano, N., Takakuwa, S., Kanda, M., and Xin, Z. (2017). Representative Urban Growing Scenarios for Future Climate Models. *Journal of Japan Society of Civil Engineers*, 73(4):I_103–I_108.

Varquez, A. C. G. and Kanda, M. (2018). Global urban climatology: a meta-analysis of air temperature trends (1960–2009). *npj Climate and Atmospheric Science*, 1(1).

Varquez, A. C. G., Nakayoshi, M., and Kanda, M. (2015). The Effects of Highly Detailed Urban Roughness Parameters on a Sea-Breeze Numerical Simulation. *Boundary-Layer Meteorology*, 154(3):449–469.

Voogt, J. and Oke, T. (2003). Thermal remote sensing of urban climates. *Remote Sensing of Environment*, 86(3):370–384.

Whitmire, R. E., Burke, D. S., Nisalak, A., Harrison, B. A., and Watts, D. M. (1987). Effect of Temperature on the Vector Efficiency of Aedes aegypti for Dengue 2 Virus. *The American Journal of Tropical Medicine and Hygiene*, 36(1):143–152.

Wienert, U. and Kuttler, W. (2005). The dependence of the urban heat island intensity on latitude A statistical approach. *Meteorologische Zeitschrift*, 14(5):677–686.

Wouters, H., Demuzere, M., Blahak, U., Fortuniak, K., Maiheu, B., Camps, J., Tielemans, D., and van Lipzig, N. P. M. (2016). The efficient urban canopy dependency parametrization (SURY) v1.0 for atmospheric modelling: description and application with the COSMO-CLM model for a Belgian summer. *Geoscientific Model Development*, 9(9):3027–3054.

Wouters, H., De Ridder, K., Poelmans, L., Willems, P., Brouwers, J., Hosseinzadehtalaei, P., Tabari, H., Vanden Broucke, S., van Lipzig, N. P. M., and Demuzere, M. (2017). Heat stress increase under climate change twice as large in cities as in rural areas: A study for a densely populated midlatitude maritime region: URBAN HEAT STRESS UNDER CLIMATE CHANGE. *Geophysical Research Letters*, 44(17):8997–9007.

Yamamoto, M., Kasai, M., Okaze, T., Hanaoka, K., and Mochida, A. (2018). Analysis of climatic factors leading to future summer heatstroke risk changes in Tokyo and Sendai based on dynamical downscaling of pseudo global warming data using WRF. *Journal of Wind Engineering and Industrial Aerodynamics*, 183:187–197.

Yang, L., Niyogi, D., Tewari, M., Aliaga, D., Chen, F., Tian, F., and Ni, G. (2016). Contrasting impacts of urban forms on the future thermal environment: example of Beijing metropolitan area. *Environmental Research Letters*, 11(3):034018.

Yau, Y. and Pean, H. (2014). The performance study of a split type air conditioning system in the tropics, as affected by weather. *Energy and Buildings*, 72:1–7.

Yoshikado, H. (1990). Vertical Structure of the Sea Breeze Penetrating through a Large Urban Complex. *Journal of Applied Meteorology*, 29(9):878–891.

Yucel, M., Varquez, A. C., Darmanto, N., and Kanda, M. (2016). Improvements of Urban Representation in Weather Models Using Global Datasets. *Journal of Japan Society of Civil Engineers*, 72(4):I_91–I_96.

Yuhas, R., Goetz, A., and Boardman, J. (1992). Discrimination among semi-arid landscape endmembers using the spectral angle mapper (SAM) algorithm. volume 1, pages 147–149, Pasadena, California. JPL Publication.

Zaki, S. A., Hagishima, A., Tanimoto, J., and Ikegaya, N. (2011). Aerodynamic Parameters of Urban Building Arrays with Random Geometries. *Boundary-Layer Meteorology*, 138(1):99–120.

Zhao, L., Lee, X., Smith, R. B., and Oleson, K. (2014). Strong contributions of local background climate to urban heat islands. *Nature*, 511(7508):216–219.

Zhao, L., Oppenheimer, M., Zhu, Q., Baldwin, J. W., Ebi, K. L., Bou-Zeid, E., Guan, K., and Liu, X. (2018). Interactions between urban heat islands and heat waves. *Environmental Research Letters*, 13(3):034003.

Zhongli, L. and Hanqiu, X. (2016). A study of Urban heat island intensity based on "local climate zones": A case study in Fuzhou, China. In *2016 4th International Workshop on Earth Observation and Remote Sensing Applications (EORSA)*, pages 250–254, Guangzhou, China. IEEE.